# Journal of Baku Engineering University

## PHYSICS

P-ISSN: 2521-6368
E-ISSN: 3107-054X

Volume 9
Number 2
2025

Journal is published twice a year
*Number - 1. June, Number - 2. December*

*An International Journal*

http://journal.beu.edu.az

**Contact address**
*Journal of Baku Engineering University*
*AZ0102, Khirdalan city, Hasan Aliyev str. 120, Absheron, Baku, Azerbaijan*
***Tel:*** *00 994 12 - 349 99 95* ***Fax:*** *00 994 12 349-99-90/91*

**e-mail:** *jr-phisics@beu.edu.az*
**web:** *http://journal.beu.edu.az*
**facebook:** *Journal Of Baku Engineering University*



ISSN 2521-6368
E-3107-054X

ISSN 2521-6368

E-3107-054X

# Journal of Baku Engineering University

## PHYSICS

Baku - AZERBAIJAN

# Journal of Baku Engineering University

## PHYSICS

### 2025. Volume 9, Number 2

## CONTENTS

JOURNAL OF BAKU ENGINEERING UNIVERSITY - PHYSICS
*2025. Volume 9, Number 2* *Pages 55-63*

*UDC: 544.723:66.017.3*
*DOI: https://doi.org/10.30546/09081.2025.002.1010*

# IN SITU SYNTHESIS Of HIERARCHICAL MOF/LDH NANOCOMPOSITES FOR ADVANCED FUNCTIONAL MATERIALS

**Amil ALIGAYEV[1,2*], Ulkar JABBARLI[3], Ulkar SAMADOVA[4], Razim BAYRAMLI[5], Gachay NAJAFOV[5], and Jialin LI[6]**

[1] *NOMATEN Centre of Excellence, National Centre for Nuclear Research, ul. A. Soltana 7, 05-400 Otwock, Poland.*
[2]*Baku Engineering University, Scientific Research Center, Hasan Aliyev str., 120 AZ-0101, Absheron, Azerbaijan.*
[3]*Institute of Theoretical Physics, Faculty of Physics, University of Warsaw, Pasteura St. 5, 02-093 Warsaw, Poland.*
[4]*Institute of Physics Ministry of Science and Education, H.Cavid 131, AZ-1073, Baku, Azerbaijan.*
[5]*Baku Engineering University, Hasan Aliyev str., 120 AZ-0101, Absheron, Azerbaijan.*
[5]*Baku Engineering University, Hasan Aliyev str., 120 AZ-0101, Absheron, Azerbaijan.*
[6]*College of Integrated Circuits, Southeast University, Nanjing, 214026, P.R.China*

*ARTICLE INFO*

*Article history:*
*Received: 2025-04-21*
*Received in revised form:2025-05-02*
*Accepted:2025-05-30*
*Available online:2025-12-21*

*Keywords:*

*Layered Double Hydroxides;*
*Metal-Organic Frameworks;*
*Nanocomposites;*
*Synthesis;*
*Morphological characterization*



*ABSTRACT*

*Nanostructured hybrid materials based on Metal-Organic Frameworks (MOFs) and Layered Double Hydroxides (LDHs) have attracted significant attention due to their exceptional tunability, high surface area, and multifunctional properties. The integration of MOFs and LDHs offers a promising approach for developing advanced materials with enhanced physicochemical stability, adsorption capacity, and catalytic efficiency. In this study, MOF/LDH composites were synthesized through a controlled coprecipitation and solvothermal route, enabling precise control over particle size, crystallinity, and surface morphology. The as-prepared materials were systematically characterized using Scanning Electron Microscopy (SEM) and Transmission Electron Microscopy (TEM) to investigate their structural morphology, interlayer arrangement, and nanoscale interface between MOF and LDH components. The morphological analysis revealed well-defined layered structures with uniform particle distribution and intimate interfacial contact, confirming the successful hybridization of the two materials. The synergistic combination of MOF porosity and LDH ion-exchange capacity is expected to enhance the material's performance in adsorption, catalysis, and environmental remediation applications. This work provides valuable insights into the design, synthesis, and morphological optimization of MOF/LDH nanostructures for multifunctional environmental and biomedical uses.*

[*]*Corresponding author: Email address: amil.aligayev@ncbj.gov.pl*

## 1. INTRODUCTION

### Background

Rapid industrialization and population growth have intensified environmental and health challenges, with global pollutant discharge rates exceeding natural degradation capacities by several orders of magnitude [1]. Industrial discharges, agricultural runoff containing persistent organic pollutants, and pharmaceutical contaminants increasingly threaten natural ecosystems,

while conventional remediation technologies often lack the efficiency, selectivity, and sustainability required to address these complex issues [2].

Nanotechnology has emerged as a transformative approach for developing functional materials with precise control over composition, structure, and properties at the nanoscale [3-6]. The ability to engineer materials at dimensions comparable to molecular and ionic species enables unprecedented control over surface chemistry, electronic structure, and interfacial phenomena critical for sensing, separation, and catalytic applications [7].

Among nanostructured materials, MOFs and LDHs have attracted significant attention due to their structural versatility and broad application potential [8-9]. MOFs are crystalline porous materials composed of metal ions or clusters (secondary building units) coordinated with multidentate organic linkers forming highly ordered three-dimensional frameworks (Figure 1a) with topological diversity [10-11]. The zeolitic imidazolate framework family (ZIFs), particularly ZIF-67 featuring $Co^{2+}$ nodes coordinated with 2-methylimidazolate linkers in a sodalite topology, exhibits remarkable thermal stability up to 350 °C and chemical resistance in organic solvents. Their extraordinarily high surface areas often exceeding 6000 $m^2/g$ for MOF-5 and 1500-1800 $m^2/g$ for ZIF-67 combined with uniform micropore apertures (3.4 Å for ZIF-67) provide molecular sieving capabilities and size-selective adsorption [12,13]. Despite these advantages, MOFs frequently display poor hydrolytic stability, with framework degradation occurring through metal-ligand bond hydrolysis under humid conditions, particularly affecting carboxylate-based MOFs. Additionally, recovering nanosized MOF particles (< 500 nm) from aqueous suspensions remains challenging due to colloidal stability.

LDHs are anionic clays featuring positively charged brucite-like layers with octahedral coordination geometry, intercalated with charge-balancing anions and water molecules (Figure 1b-c). Their general formula, $[M^{2+}_{1-x}M^{2+}_{x}(OH)_2]^{x+}(A^{n-})_{x/n}\cdot mH_2O$, demonstrates compositional flexibility where divalent cations ($M^{2+}$ = $Mg^{2+}$, $Zn^{2+}$, $Ni^{2+}$, $Co^{2+}$) and trivalent cations ($M^{3+}$ = $Al^{3+}$, $Fe^{3+}$, $Cr^{3+}$) can be varied across $M^{2+}/M^{3+}$ ratios typically ranging from 2:1 to 4:1 [14]. The interlayer spacing (0.7-0.8 nm for carbonate-intercalated forms) can be expanded through anion exchange, enabling tunable host-guest chemistry. This structural adaptability allows LDHs to serve as efficient adsorbents with typical capacities of 50-200 mg/g for organic dyes, while their basic surface hydroxyl groups facilitate catalytic applications [15]. However, LDHs suffer from structural instability in acidic environments (pH < 4) and aggregation in aqueous media, reducing accessible surface area from theoretical values of 200-300 $m^2/g$ to often below 80 $m^2/g$ in practical applications.

The integration of LDHs and MOFs into hybrid nanocomposites represents a strategic approach to overcome individual limitations while exploiting complementary advantages [16]. The positively charged LDH surface can provide electrostatic stabilization and nucleation sites for MOF growth, while the rigid MOF framework can serve as a physical barrier preventing LDH layer restacking. Theoretical models predict that such heterostructures should exhibit hierarchical porosity with distinct pore size distributions: micropores (< 2 nm) from MOF cavities contributing to high surface area and molecular selectivity, mesopores (2-50 nm) from interlayer spacing and interparticle voids facilitating mass transport. However, achieving controlled interfacial integration requires precise manipulation of nucleation kinetics, growth rates, and surface chemistry. Minor variations in metal ion concentration, pH gradients, or solvent polarity can drastically alter crystallization pathways, leading to either core-shell structures, physical mixtures, or genuine heterostructures with epitaxial-like interfaces.

Aligned with global sustainability initiatives including the United Nations Sustainable Development Goals (SDGs), MOF/LDH-based materials hold potential for advancing targets related to clean water and sanitation (SDG 6), good health and well-being (SDG 3), and responsible consumption and production (SDG 12) [17]. This research addresses critical synthesis challenges through a controlled coprecipitation-solvothermal approach optimized for reproducible heterostructure formation.

**Problem Statement**

LDHs and MOFs exhibit remarkable potential for environmental remediation and multifunctional material design, but their practical application is constrained by several critical challenges. LDHs often suffer from structural instability and aggregation in aqueous environments, which reduces surface area and limits adsorption efficiency. MOFs, while highly porous and tunable, frequently display poor chemical stability under humid, acidic, or basic conditions, leading to framework collapse and performance loss. Hybrid LDH/MOF systems offer a promising route to combine the advantages of both materials, yet their controlled synthesis and reproducibility remain challenging. Minor variations in synthesis conditions can drastically alter crystallinity, morphology, porosity, and interfacial interactions, making it difficult to establish reliable structure-property relationships. Additionally, scalable and cost-effective synthesis methods are limited, as many current protocols require high temperatures, multi-step processing, or expensive reagents. Understanding how nanoscale architecture influences macroscopic performance, particularly in terms of adsorption, structural integrity, and hybrid integration, remains incomplete. Addressing these challenges requires innovative synthesis strategies, precise morphological control, and comprehensive characterization to realize hybrid materials with predictable and reproducible properties.

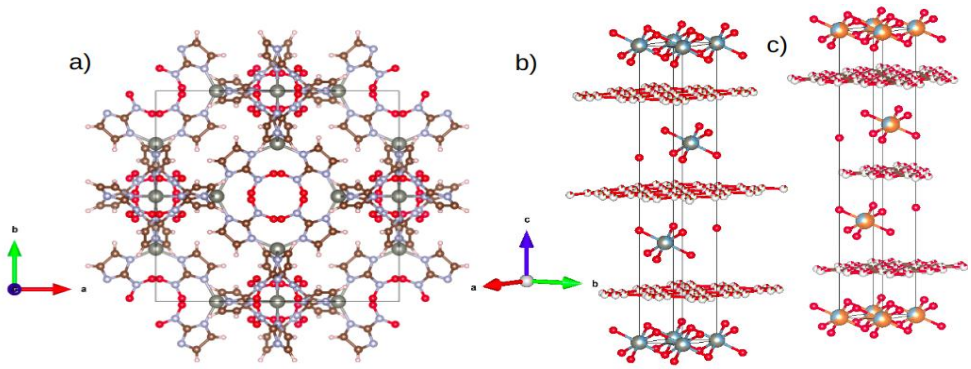


***Fig. 1*** *(a) Crystal structure of a representative MOF illustrating its three-dimensional porous network. (b) LDH structure based on Mg-Al, showing the periodic stacking of brucite-like layers along the c-axis. (c) LDH based on Zn-Al, displaying a similar layered arrangement with interlayer spacing influenced by the metal composition. Color code: gray (metal centers), red (oxygen), blue (nitrogen), brown (carbon), and white (hydrogen).*

**Research Objectives**

This study aims to:

- Develop controlled synthesis protocols for hybrid MOF/LDH nanomaterials with tunable crystallinity, particle size, and interfacial architecture.

- Investigate structural integration between MOF and LDH components to optimize hybrid morphology and interfacial interactions.
- Perform advanced characterization using SEM, and TEM techniques to elucidate nanoscale architecture, surface topology, and structural features.
- Evaluate physicochemical properties such as porosity, surface area, and crystal structure to correlate synthesis parameters with material performance.

**Scientific Novelty**

The scientific novelty of this work lies in the strategic integration of LDHs and MOFs into hybrid nanomaterials with precisely controlled structures and tunable functional properties. Unlike previous studies that largely investigate these materials separately, this research systematically combines the structural stability and ion-exchange capabilities of LDHs with the high porosity, tunable chemistry, and modularity of MOFs, creating multifunctional systems with synergistic performance. The use of a controlled coprecipitation-solvothermal synthesis method enables precise tuning of crystallinity, particle morphology, and interfacial architecture, ensuring reproducibility and consistent hybrid formation. Advanced characterization using SEM, and TEM provides detailed insights into nanoscale structural features, surface topology, and interfacial interactions, allowing the establishment of clear structure-property relationships. By correlating synthesis conditions with morphological, structural, and functional outcomes, this study offers predictive design principles for hybrid nanomaterials with enhanced adsorption efficiency, stability, and functionality. Additionally, the emphasis on environmentally compatible and energy-efficient synthesis introduces a sustainable dimension to hybrid material development. Collectively, this work presents a comprehensive framework for the rational design, synthesis, and characterization of multifunctional LDH/MOF hybrids, advancing the field of nanostructured materials for environmental and multifunctional applications.

## 2. METHODOLOGY

### *2.1 Synthesis of Layered Double Hydroxides*

Mg-Al and Zn-Al LDHs were synthesized via coprecipitation followed by hydrothermal crystallization to achieve phase purity and structural ordering. For Mg-Al LDH, aqueous solutions of $Mg(NO_3)_2 \cdot 6H_2O$ (0.225 M) and $Al(NO_3)_3 \cdot 9H_2O$ (0.075 M) were prepared to maintain a $Mg^{2+}/Al^{3+}$ molar ratio of 3:1, which provides optimal charge balance and layer stability according to Miyata's criterion. Similarly, Zn-Al LDH precursors employed $Zn(NO_3)_2 \cdot 6H_2O$ and $Al(NO_3)_3 \cdot 9H_2O$ at the same molar ratio. The mixed metal solution (100 mL, total metal concentration 0.3 M) was added dropwise at 1 mL/min into 150 mL of 0.1 M NaOH solution under vigorous magnetic stirring (500 rpm) to maintain pH 10.0 ± 0.2, monitored continuously using a calibrated pH electrode. This pH range ensures complete hydroxide precipitation while minimizing aluminum hydroxide formation that occurs above pH 11.

The coprecipitation was conducted at 25 °C under continuous nitrogen purging (50 mL/min) to prevent atmospheric $CO_2$ contamination, which would lead to carbonate intercalation and reduced anion exchange capacity. The resulting white suspension was aged at 65 °C for 24 h in a sealed glass reactor to promote Ostwald ripening and layer crystallization. The precipitate was recovered by centrifugation (8000 rpm, 10 min), washed five times with deionized water until

the supernatant reached pH 7 ± 0.5, and dried at 80 °C in a vacuum oven overnight (12 h, $10^{-2}$ mbar).

To enhance crystallographic ordering and increase lateral platelet dimensions, the as-obtained LDH precursors were subjected to hydrothermal treatment at 120 °C for 12 h in a 100 mL Teflon-lined stainless-steel autoclave filled to 70% capacity with deionized water. This thermal aging promotes dissolution-recrystallization processes that eliminate structural defects and increase crystallite size. The final products were filtered through 0.45 μm membranes, washed with ethanol, and dried at 60°C, yielding white powders with typical mass yields of 85-90% based on theoretical metal hydroxide formation.

### *2.2 Synthesis of MOF: ZIF-67*

ZIF-67 was synthesized via a modified room-temperature precipitation method optimized for uniform particle size distribution. Cobalt (II) nitrate hexahydrate ($Co(NO_3)_2 \cdot 6H_2O$, 1.455 g, 5 mmol) was dissolved in 50 mL methanol (solution A, 0.1 M), while 2-methylimidazole (2-MeIm, 6.566 g, 80 mmol) was dissolved separately in 200 mL methanol (solution B, 0.4 M). The ligand-to-metal ratio of 16:1 was selected based on optimization studies showing this ratio provides complete coordination while minimizing unreacted ligand contamination.

Solution B was rapidly poured into solution A under vigorous magnetic stirring (600 rpm) ambient temperature (25 ± 2 °C). Upon mixing, an immediate color change from pink to purple indicated ZIF-67 nucleation, with the suspension darkening progressively. The mixture was stirred continuously for 6 h to ensure complete crystallization and uniform particle growth. The purple precipitate was collected by centrifugation (8000 rpm, 15 min), washed three times with 50 mL portions of fresh methanol to remove excess ligand and nitrate anions, and dried under vacuum at 60 °C for 12 h (pressure < $10^{-2}$ mbar).

To improve crystallinity and activate the framework by removing residual solvent molecules from pores, the product underwent solvothermal activation at 120 °C for 6 h in methanol using the same autoclave configuration as LDH synthesis. This treatment increases framework rigidity and enhances porosity without inducing thermal decomposition, which begins above 300 °C for ZIF-67. The final ZIF-67 powder exhibited a characteristic purple color and mass yield of 92-95% based on theoretical $Co(2\text{-MeIm})_2$ formation.

### **2.3 Synthesis of MOF/LDH Composite Materials**

Hierarchical ZIF-67/LDH composites were synthesized through an in situ growth strategy designed to promote heterogeneous nucleation of MOF crystals on LDH surfaces. Pre-synthesized LDH powder (500 mg) was dispersed in 50 mL methanol via ultrasonication (40 kHz, 200 W) for 30 min to achieve complete delamination and individual platelet suspension, verified by dynamic light scattering showing monomodal distributions with average hydrodynamic diameters of 150-250 nm. The LDH suspension was added to solution A ($Co(NO_3)_2 \cdot 6H_2O$ in methanol) under moderate stirring (400 rpm) and equilibrated for 1 h at room temperature, allowing electrostatic adsorption of cobalt ions onto negatively charged LDH edge sites and hydroxyl-terminated surfaces. Solution B (2-MeIm in methanol) was then added dropwise at 2 mL/min to the $Co^{2+}$-LDH mixture, initiating ZIF-67 nucleation preferentially at LDH-metal ion adsorption sites. This staged addition protocol spatially separates metal ion adsorption from framework formation, promoting heterostructure integration rather than independent precipitation.

The composite suspension was stirred at room temperature for 8 h to ensure complete MOF shell formation, then aged statically for an additional 12 h to promote interfacial reorganization and strengthen chemical bonding between components. The solid product was recovered by centrifugation (6000 rpm, 15 min to avoid disrupting MOF-LDH interfaces), washed thoroughly with methanol (five cycles of 50 mL), and dried at 70 °C under vacuum for 16 h. The mass ratio of ZIF-67 to LDH in the final composite was estimated at approximately 2:1 based on metal ion stoichiometry, yielding light purple powders with typical mass yields of 88-92%. Control experiments were conducted by physically mixing pre-synthesized ZIF-67 and LDH powders via grinding to verify that enhanced properties arise from heterostructure formation rather than simple additive effects.

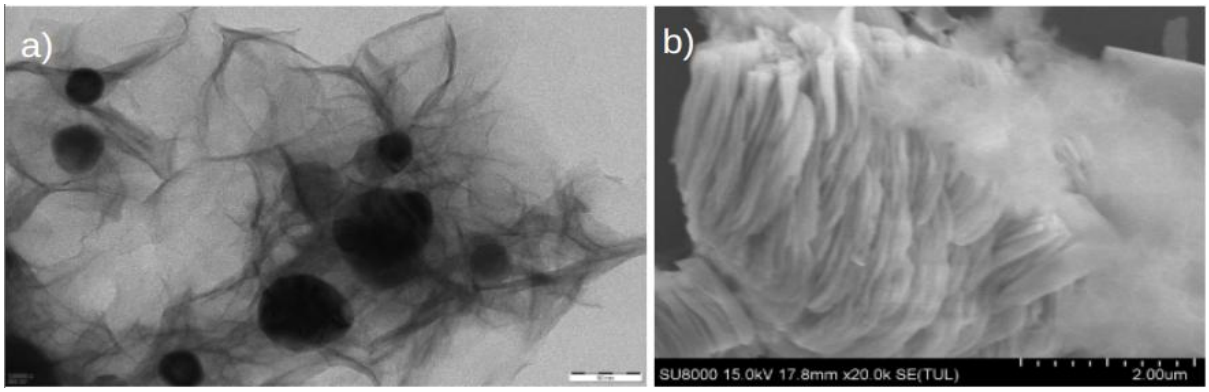


***Fig. 2*** *TEM and SEM images of the synthesized materials. (a) TEM image of ZIF-67 nanocrystals showing well-defined rhombic dodecahedral morphology with uniform particle distribution and thin nanosheet interfaces. (b) SEM image of LDH displaying typical layered plate-like architecture with stacked nanosheets, indicating successful formation of the hydrotalcite-like structure.*

## 3. RESULTS AND DISCUSSION

### *3.1 Morphological Characterization*

High-resolution SEM and TEM analyses provided comprehensive insights into the morphological characteristics and structural integration of the synthesized materials. Pristine Mg-Al and Zn-Al LDHs exhibited the characteristic two-dimensional hexagonal platelet morphology with lateral dimensions ranging from 150 to 300 nm and thickness of 20-40 nm, corresponding to stacking of 25-50 individual brucite-like layers (Figure 2b). The well-defined hexagonal perimeters and smooth basal planes observed in SEM images indicate high crystallinity and minimal edge defects. Cross-sectional TEM imaging revealed uniform layer spacing of approximately 0.76 nm, consistent with nitrate-intercalated LDH phases. The plate-like architecture provides high aspect ratios (6-10) favorable for colloidal dispersion and interfacial interactions.

Pure ZIF-67 displayed highly uniform rhombic dodecahedral morphology with mean particle diameters of 350 ± 50 nm determined from statistical analysis of 200 particles in TEM images (Figure 2a). The polyhedral facets correspond to the {110} crystallographic planes of the sodalite topology, with sharp edges indicating single-crystalline character. The monodisperse size distribution (coefficient of variation < 15%) confirms controlled nucleation and growth kinetics under the selected synthesis conditions. High-resolution TEM revealed lattice fringes with d-spacing of 0.294 nm, matching the (211) planes of cubic ZIF-67 (space group I-43m).

The ZIF-67/LDH nanocomposites exhibited a distinctive hierarchical heterostructure morphology that unambiguously demonstrates successful interfacial integration. SEM images revealed that multiple ZIF-67 nanocrystals (200-400 nm diameter, slightly smaller than pure ZIF-67 due to heterogeneous nucleation effects) were intimately and uniformly anchored across both basal planes and edge sites of individual LDH hexagonal nanosheets. The density of MOF decoration was approximately 15-25 particles per LDH platelet, with preferential localization at edge sites suggesting enhanced nucleation at coordinatively unsaturated metal centers.

TEM analysis at higher magnification provided critical evidence of genuine heterostructure formation rather than simple physical mixing. At MOF-LDH interfaces, neither distinct boundary lines nor amorphous separation layers were observed; instead, continuous lattice fringe patterns extended across interfaces over distances of 2-3 nm, suggesting epitaxial-like growth or strong chemical bonding through Co-O-M bridges.

### *3.2 Physicochemical Properties and Synergistic Effects*

Quantitative surface area analysis using nitrogen physisorption indicated that the ZIF-67/LDH nanocomposite exhibited a specific surface area of 820-950 $m^2/g$, representing a substantial enhancement compared to pristine Mg-Al LDH (68 $m^2/g$) and Zn-Al LDH (74 $m^2/g$). This 11-13 fold increase significantly exceeds the weighted average of individual components (calculated as ~450 $m^2/g$ for a 2:1 ZIF-67:LDH mass ratio with ZIF-67 surface area of 1650 $m^2/g$), indicating synergistic effects beyond simple physical combination. Pure ZIF-67 synthesized under identical conditions exhibited 1650 $m^2/g$, consistent with literature values.

Pore size distribution analysis revealed a bimodal porosity profile characteristic of hierarchical structures. The primary micropore distribution centered at 3.4 Å corresponds to the intrinsic ZIF-67 cage apertures, while a secondary mesopore distribution spanning 3-8 nm originates from interlayer spacing of LDH (expanded from typical 0.76 nm due to partial delamination) and interparticle voids between MOF nanocrystals anchored on LDH surfaces. This hierarchical pore architecture addresses a fundamental limitation of pure MOFs: while micropores provide high surface area and selective adsorption, they can suffer from diffusion limitations. The mesoporous LDH component creates transport highways facilitating rapid molecular diffusion to microporous MOF regions, effectively reducing mass transfer resistance.

The dramatic surface area enhancement in the composite is attributed to several synergistic mechanisms. First, the in situ growth strategy prevents unfavorable layer-stacking (restacking) or aggregation of LDH sheets by utilizing MOF nanocrystals as physical spacers that maintain interlayer separation. Second, the LDH scaffold provides mechanical support preventing ZIF-67 particle aggregation that typically occurs during solvent removal and drying. Third, heterogeneous nucleation on LDH surfaces may generate smaller ZIF-67 crystals with higher surface-to-volume ratios compared to homogeneous precipitation.

The combined microporosity from ZIF-67 (providing high surface area, molecular selectivity through size exclusion, and specific adsorption sites from coordinatively unsaturated cobalt centers) with the ion-exchange capacity of LDH (capable of removing anionic contaminants through interlayer exchange) and the hierarchical mesoporosity (facilitating rapid mass transport) positions these heterostructures as multifunctional platforms. Theoretical modeling suggests such architectures should exhibit superior performance in applications requiring both molecular sieving and electrostatic interactions, such as simultaneous removal of cationic dyes

(adsorbed on negatively charged LDH surfaces) and small organic molecules (captured in ZIF-67 micropores).

## 4. CONCLUSION

This research successfully demonstrated the controlled synthesis of novel hierarchical ZIF-67/LDH heterostructures through an optimized in situ coprecipitation-solvothermal method featuring staged reagent addition and heterogeneous nucleation control. Comprehensive morphological characterization via high-resolution SEM and TEM provided unambiguous evidence of successful heterostructure formation, revealing that rhombic dodecahedral ZIF-67 nanocrystals (200-400 nm) were uniformly and intimately anchored onto two-dimensional hexagonal LDH nanosheets (150-300 nm lateral dimensions) with continuous interfacial bonding.

The developed heterostructures effectively address critical limitations of individual components: the aggregation tendency and low surface area (< 80 $m^2/g$) of pristine LDHs are overcome through MOF-mediated layer separation, while the hydrolytic instability and particle recovery challenges of nanosized MOFs are mitigated through integration with the robust inorganic LDH matrix. The resulting bimodal micro-mesoporous architecture (micropores: 3.4 Å from ZIF-67 cages; mesopores: 3-8 nm from interlayer and interparticle spacing) synergistically combines molecular selectivity with efficient mass transport, yielding surface areas of 820-950 $m^2/g$ that substantially exceed predictions from simple physical mixtures.

Quantitative structure-property correlations established through systematic characterization demonstrate that in situ heterostructure formation, rather than post-synthetic mixing, is essential for achieving synergistic performance enhancements. The 11-13 fold surface area increase relative to pristine LDH, coupled with preservation of MOF crystallinity and LDH layered architecture, validates the synthesis strategy and provides a platform for rational design of multifunctional hybrid nanomaterials.

Future investigations will expand characterization to include powder X-ray Diffraction (XRD) for phase identification and crystallographic structure refinement, Fourier-Transform Infrared Spectroscopy (FTIR) to probe chemical bonding at MOF-LDH interfaces and verify functional group preservation, and comprehensive nitrogen physisorption analysis (BET method) for detailed pore size distribution mapping. Quantitative performance evaluation in target applications including adsorption kinetics and capacity for organic pollutants (model contaminants: methylene blue, tetracycline), catalytic efficiency in model reactions (e.g., $CO_2$ cycloaddition, selective oxidation), and assessment as delivery platforms for model pharmaceutical compounds will establish practical utility. These studies will advance understanding of structure-function relationships in hybrid nanomaterials and contribute to development of sustainable, multifunctional systems for environmental remediation and biomedical applications.

**REFERENCE LIST**


1. Tyagi, D., Wang, H., Huang, W., Hu, L., Tang, Y., Guo, Z., ... & Zhang, H. (2020). Recent advances in two-dimensional-material-based sensing technology toward health and environmental monitoring applications. *Nanoscale*, *12*(6), 3535-3559.
2. Dinic, F., Singh, K., Dong, T., Rezazadeh, M., Wang, Z., Khosrozadeh, A., Voznyy, O. (2021). Applied machine learning for developing next-generation functional materials. *Advanced Functional Materials*, *31*(51), 2104195.
3. Wong, I. Y., Bhatia, S. N., & Toner, M. (2013). Nanotechnology: emerging tools for biology and medicine. *Genes & development*, *27*(22), 2397-2408.
4. Danish, M. H., Aligayev, A., Muhammad, Z., Chen, T., Mansoor, A., Qin, X. (2025). Synergistic modulation of band structure and phonon transport for higher thermoelectric performance of WSe2. *Chemical Engineering Journal*, 164510.
5. Samadova, U., Aligayev, A., Ismail, P. M., Liu, M., Safarzade, U., Qiao, L. (2025). Novel Single Perovskite Material for Visible-Light Photocatalytic CO2 Reduction via Joint Experimental and DFT Study. Small, 21(2), 2407206.
6. Raziq, F., Aligayev, A., Shen, H., Ali, S., Shah, R., Ali, S., Qiao, L. (2022). Exceptional photocatalytic activities of rGO modified (B, N) Co-doped WO3, coupled with CdSe QDs for one photon Z-scheme system: a joint experimental and dft study. *Advanced Science*, *9*(2), 2102530.
7. Aligayev, A., Raziq, F., Jabbarli, U., Rzayev, N., & Qiao, L. (2022). Morphology and topography of nanotubes. In Graphene, Nanotubes and quantum dots-based nanotechnology (pp. 355-420). *Woodhead Publishing*.
8. Zhu, Y., Du, W., Zhang, Q., Yang, H., Zong, Q., Wang, Q., Zhan, J. (2020). A metal-organic framework template derived hierarchical Mo-doped LDHs@MOF-Se core-shell array electrode for supercapacitors. *Chemical Communications*, *56*(89), 13848-13851.
9. Farhan, A., Rashid, E. U., Waqas, M., Ahmad, H., Nawaz, M., Munawar, M., Iqbal, J. (2023). Progress in layered double hydroxides (LDHs): Synthesis and application in adsorption, catalysis and photoreduction. *Science of The Total Environment*, 912, 168539.
10. Cai, G., Yan, P., Zhang, L., Zhou, H. C., & Jiang, H. L. (2021). Metal–organic framework-based hierarchically porous materials: synthesis and applications. *Chemical Reviews*, *121*(20), 12278-12326.
11. Jialin, L., Shaowei L., Aligayev, A., Jastrzębska, A., Qing, H. (2024) Dual-mode SERS and colorimetric sensor for lung cancer VOC-biomarker detection using hydrogel patches. *Chemical Engineering Journal*, 523, 168343.
12. Ding, M., Cai, X., & Jiang, H. L. (2019). Improving MOF stability: approaches and applications. *Chemical Science*, *10*(44), 10209-10230.
13. Liu, C., Cao, Y., Xia, Q., Aligayev, A., & Huang, Q. (2025). CoNi-MOF laccase-like nanozymes prepared by dielectric barrier discharge plasma for treatment of antibiotic pollution. *Journal of Hazardous Materials*, 493, 138282.
14. Olfs, H. W., Torres-Dorante, L. O., Eckelt, R., & Kosslick, H. (2009). Comparison of different synthesis routes for Mg-Al layered double hydroxides (LDH): Characterization of the structural phases and anion exchange properties. *Applied clay science*, *43*(3-4), 459-464.
15. Li, C., Wei, M., Evans, D. G., & Duan, X. (2014). Layered double hydroxide-based nanomaterials as highly efficient catalysts and adsorbents. *Small*, *10*(22), 4469-4486.
16. Zhang, W. D., Hu, Q. T., Wang, L. L., Gao, J., Zhu, H. Y., Yan, X., & Gu, Z. G. (2021). In-situ generated Ni-MOF/LDH heterostructures with abundant phase interfaces for enhanced oxygen evolution reaction. Applied Catalysis B: Environmental, 286, 119906.
17. Lee, K. H., Noh, J., & Khim, J. S. (2020). The Blue Economy and the United Nations' sustainable development goals: Challenges and opportunities. Environment international, 137, 105528.

JOURNAL OF BAKU ENGINEERING UNIVERSITY - PHYSICS
*2025. Volume 9, Number 2* *Pages 64-72*

*UDC: 53.07*
*DOI:* **https://doi.org/10.30546/09081.2025.002.1014**

# INFLUENCE OF METALLIC HOST STRUCTURE ON MOLECULAR HYDROGEN EMBEDDED AND STABILITY UNDER ION IMPLANTATION

**Alexandr DONKOV**
*International Intergovernmental Organization-Joint Institute for Nuclear Research, Dubna, Russian*
*Institute of Solid-State Physics, Bulgarian Academy of Sciences, Sofia, Bulgaria, aadonkov@theor.jinr.ru*

**Sekine ISAYEVA**
*Azerbaijan Technical University, Baku, Azerbaijan*
*sekinebagirli135@gmail.com*

**Aidos AKZHUNUSOV**
*L.N. Gumilyov Eurasian National University, Astana, Kazakhstan*
*aidos.akzhunussov89@gmail.com*

**Adiba MIRSAGATOVA**
*Institute of Nuclear Physics of the Uzbek Academy of Sciences, Tashkent, Uzbekistan*
*mirsagatova69@gmail.com*

**Alimardon RAKHIMOV**
*International Intergovernmental Organization-Joint Institute for Nuclear Research, Dubna, Russian*
*Institute of Nuclear Physics of the Uzbek Academy of Sciences, Tashkent, Uzbekistan, alimardon@jinr.ru*

**Bakhrom YARMATOV**
*Institute of Nuclear Physics of the Uzbek Academy of Sciences, Tashkent, Uzbekistan*
*yarmatov@inp.uz*

**Kiiril KREZHOV**
*Institute of Electronics, Bulgarian Academy of Sciences, Sofia, Bulgaria*
*kiril.krezhov@gmail.com*

***ARTICLE INFO***

*Article history:*
*Received: 2025-05-01*
*Received in revised form:2025-05-12*
*Accepted:2025-06-10*
*Available online:2025-12-21*

*Keywords:*
*High purity metal, ion implantation, annihilation, positron, hydrogen diffusion.*


***ABSTRACT***

*With this study we would like to confirm previously predicted computational results regarding the formation of molecular hydrogen during ion-metal interactions. The formation of defects in iron and titanium and their binding to hydrogen were analyzed using the positron lifetime method using calculations made with the MIKA software package. The observed decrease in the positron lifetime indicates a structural saturation with hydrogen, probably in its molecular form, and suggests the formation of $T(H)_2$ complexes in the induced cavities. These accumulations and additional hydride bonds act as barriers for hydrogen diffusion to the surface. For a perfect lattice in titanium in its hexagonal structure, a lifetime of 143 ps was calculated. For a vacancy with a few implanted atoms, we calculated a lifetime of 142 ps. For a perfect lattice for alpha iron, we obtained a value for the positron lifetime of 100 ps. An iron's vacancy with six implanted hydrogen atoms reports a lifetime of 101 ps.*

## 1. INTRODUCTION

The challenges associated with the discovery and application of new energy sources remain one of the main driving forces in the development of human civilization [1]. The efficient utilization, storage, and transformation of energy resources have consistently formed the foundation of scientific and technological progress [2]. Advances in energy technologies have historically determined the pace of industrial growth, transportation development, and large-scale engineering achievements [3]. In this context, research focused on innovative energy conversion mechanisms is not only scientifically significant but also strategically essential for the future of humanity. In recent decades, the expansion of space exploration has led to new challenges related to energy extraction and the utilization of energy sources [4]. Renewed global interest in long-term space missions and potential colonization of planets near Earth has intensified the search for sustainable and efficient energy solutions. The possibility of long-term space travel critically depends on reliable propulsion systems and the continuous availability of fuel. Hydrogen, as a carrier for space propulsion, is a necessary product that provides a multitude of ancillary activities in space science [5]. To date, chemical combustion of hydrogen has been the main mechanism for propelling spacecraft. However, transporting sufficient quantities of hydrogen fuel for long-distance missions presents substantial logistical and technical challenges. This limitation naturally leads to a fundamental question: could hydrogen be generated directly in space using naturally available radiation environments, particularly the flux of high-energy protons emitted by the Sun? The concept of radiation-assisted hydrogen production and migration in metallic systems has been explored in previous studies. For example, Primakov et al. [6] investigated the acceleration of hydrogen diffusion in metals under gamma irradiation, particularly within environments simulating thermonuclear reactor conditions. In such systems, high-energy protons penetrate metallic structures, lose their kinetic energy within the bulk material, and subsequently participate in diffusion processes. The additional energy supplied by gamma radiation may enhance defect formation and atomic mobility, thereby facilitating hydrogen transport and potentially promoting recombination processes leading to molecular hydrogen formation. These observations indicate that ionizing radiation can play a dual role: first, by generating hydrogen in metal carriers by proton implantation, and second, by stimulating its migration and recombination from the formed metal hydride inside the lattice. Such a mechanism opens up the possibility of radiation-induced hydrogen accumulation in metallic structures exposed to cosmic rays. For a complete and practical cycle, however, attention must also be paid to the subsequent hydrogen management steps, including capture, stabilization, and controlled extraction (adsorption/desorption) of the formed molecular hydrogen. Understanding how hydrogen interacts with metal elements – its diffusion pathways, defect-assisted capture mechanisms, recombination behavior, and eventual release – is essential for assessing the feasibility of building a next-generation technology. Thus, the task that we set ourselves in this work is to propose a mechanism for selecting a suitable material in which after proton irradiation we can expect a product $H_2$. According to the work of Popov et al. [7] where iron and tungsten were used as host materials, the parameters that take into account the contribution of positron annihilation with valence and core electrons undergo an extremum and change their course. It is evident that at a certain point hydrogen forms bonds either with itself or in hydride form with the host metal. In the works of Pushilina et al. [8], Stepanova et al. [9], Laptev et al. [10], Bordulev et al. [11], Mikhailov et al. [12], Stepanova et al. [13], Mishin et al. [14] and Lider et al. [15] the phase transformation of titanium hydride and Zr-Nb base is considered, under different initial conditions. It is logical that when the valence electrons in the host material

are slightly inside the defects there will be less participation of ionized hydrogen in hydride form with the metal. It is for this reason that in the present work we compare the materials iron and titanium (which has a significantly lower valence than iron), in order to have a basis with which to continue our further work in this direction.

## 2. METHODS

**MIKA:** A software package [16] based on the TCDFT was used. The parameterized model in a localized electron gas is used to introduce the positron wave function. An improvement of Boronski and Nieminen [17] is introduced to approximate the volume correlation for electrons:

$$E_{xc}[n(r)] = \int n(r)\varepsilon_{xc}[n(r)]dr. \qquad (1)$$

$\varepsilon_{xc}[n(r)]$ is the single-particle exchange-correlation energy functional. The effective potential of Kohn and Sham is included in the work of Hohenberg, Kohn and Sham, where the DFT formalism accounting for the electron-positron interaction is considered. [18]. The momentum density is calculated separately for each electron state described by $\varphi_j$ according to the equation:

$$\rho_j(p) = \pi r_0^2 cu(0) \text{ and } u = \frac{\lambda_j^{LDA}}{\lambda_j^{IPM}}. \qquad (2)$$

where IPM is Independent Particle Model [19]. The positron lifetime (τ) is the reciprocal of the annihilation rate ($\lambda$):

$$\lambda = \pi r_0^2 c \int dr n_{+e}(r) n_{-e}(r) \gamma = \pi r_0^2 c \sum_i \int dr. \qquad (3)$$

$r_0$ is the classical electron radius, c is the speed of light, $\gamma$ is enhancement factor.

## 3. RESULTS AND DISCUSSION

Hydrogen implantation calculations in titanium and iron were performed by modeling a single vacancy cluster with an increasing number of hydrogen atoms (from one to six). The process simulates the formation of a hexagonal hydrogen structure (Fig. 1. a), b)), stabilized by internal pressure in the crystal lattice of both materials. The models used include a hexagonal lattice of 108 titanium atoms (space group $P6_3/mmc$) and a body-centered cubic (BCC) lattice of 250 iron atoms.

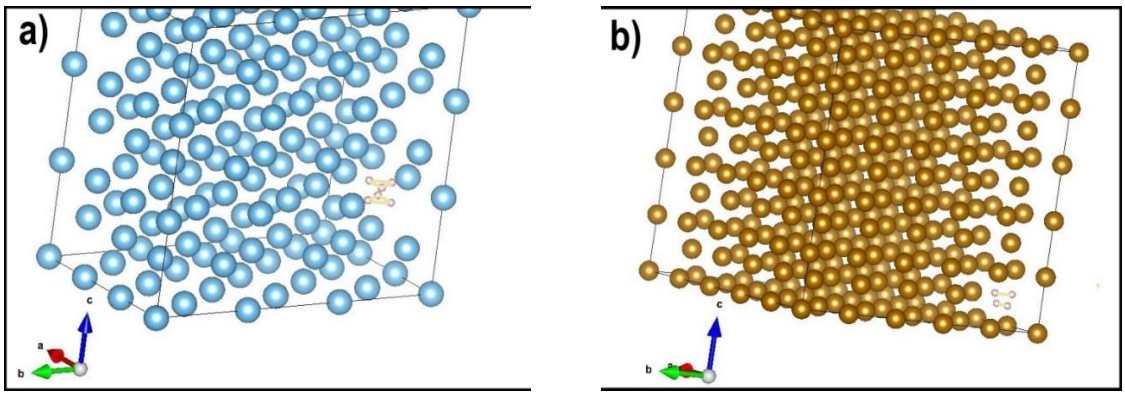


***Figure 1.*** *Mono-vacancy and a hydrogen structure: (a) for titanium lattice with 6 implanted H atoms in defect; (b) for iron lattice with 4 implanted H atoms in defect.*

In the following figure (Fig. 2 a), b)) we present the dependence of the positron lifetime (τ), on the increasing number of hydrogen atoms, in a single-vacancy vacancy cluster – Fig. 2. A) – for the titanium crystal lattice, Fig. 2. B) – for the iron structure.

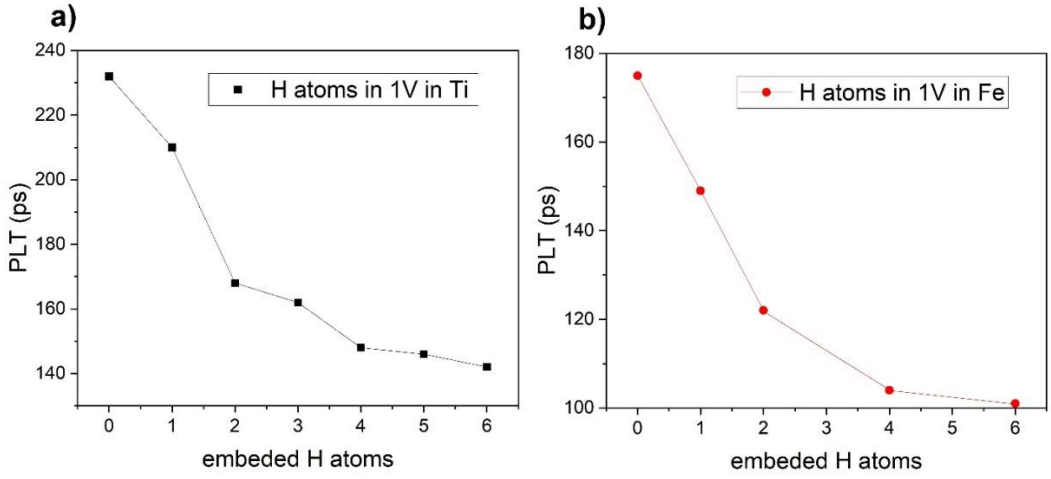


***Figure 2***. *τ as a function of the increasing number of hydrogen atoms in the vacancy cluster: a) for titanium, b) for iron.*

It is evident that in the significant difference between τ=100 ps, a perfect lattice for iron and τ=143 ps a perfect lattice for titanium, two factors play a major role - the arrangement of the atoms in space and the valence of the two elements. Regarding the arrangement of atoms in titanium, we have a close packing of the hexagonal type, while BCC is not a close packing, which means that although the arrangement is denser in titanium, the second factor - the valency - is essential and it is for this reason that the positron feels significantly freer in the titanium structure than in the iron one. The conclusion that we can make when implanting hydrogen atoms in the defect is similar - the electron density of a titanium lattice with a defect is significantly lower and respectively τ=142 ps with 6 embeded hydrogen atoms in a monovacancy, while for the same amount of embeded hydrogen atoms in an iron monovacancy τ=101 ps. The low electron density in titanium can be interpreted as a positive factor for transporting the hydrogen implanted in the defects, which at a certain point should bind in its molecular form. What has been said so far can be confirmed by the following figure (Fig. 3. a) - titanium, Fig. 3. b) - iron), where a ratio of the electron momentum density is determined in relation to the evolution of the increasing number of hydrogen atoms.

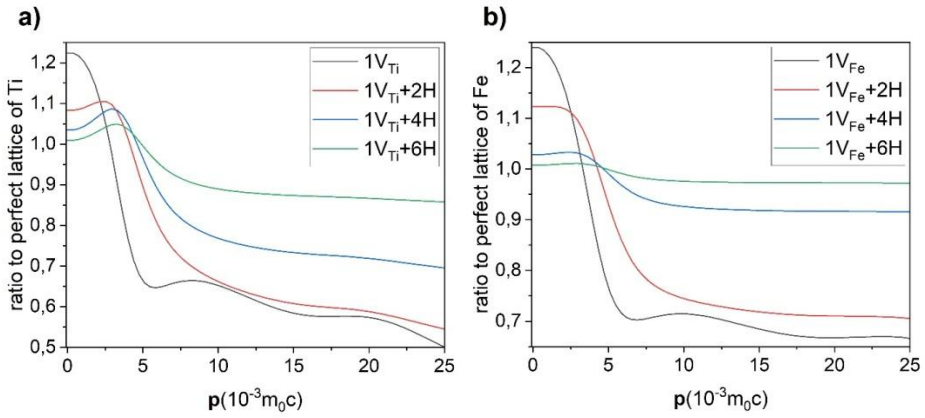


***Figure 3.*** *Ratio of electron momentum density in mono-vacancy, mono-vacancy with 2, 4 and 6 hydrogen atoms, to a perfect lattice: a) for titanium, b) for iron.*

Directly from the last figure we can note the increased contribution of valence d-electrons to the annihilation in iron compared to titanium. It is seen how under the influence of hydrogen bonds with each subsequent accumulation of embedded hydrogen atoms, the valence sharply decreases, while at 6 hydrogens in the mono-vacancy the valence of the defect in iron is lower even than the valence of titanium under the same conditions. This in turn answers the question of what type a candidate for a host material should be, in the production of molecular hydrogen under radiation conditions, if it is a metal. On the one hand, this material should have a low valence and on the other hand, it should have high porosity in order to have suitable conditions for the removal of the hydrogen accumulated inside the defects. Studies have shown that the mechanism of formation of molecular hydrogen by proton implantation in porous materials is much slower. In Zr-based binary ceramic compounds, depending on the absorption dose of gamma quanta in their crystal structure, amorphization of oxide layers, mobilization of mono-vacancies, defect formation, recombination mechanism and functional groups decomposition, increase in crystallinity size due to structural rearrangement of oxygen ions, electron density, and different splitting of the energy levels of the material have been widely studied [20-21]. Gamma irradiation of ZrC and $ZrB_2$ induces the formation of Zr, B, and O vacancies through energy transfer processes associated with Compton scattering and secondary electron cascades, which generate atomic displacements in the crystal lattice [22]. Although $\gamma$-photons interact weakly with matter directly, the energetic electrons produced during irradiation can exceed the displacement threshold energy of lattice atoms, leading to the creation of point defects [23]. In ZrC, carbon vacancies typically form more readily due to their lower displacement energies compared to zirconium atoms, whereas in $ZrB_2$, boron vacancies are energetically favored over zirconium vacancies [24]. Oxygen-related vacancies may arise from impurity phases or surface oxidation layers, particularly under irradiation-enhanced diffusion conditions [25]. The formation and stabilization of vacancy clusters require cumulative energy on the order of several electron volts per defect, sufficient to overcome local binding energies and promote defect aggregation within the irradiated lattice [21], [23]. However, the mechanism of defect formation and vacancy formation in oxide and ceramic compounds by neutron irradiation is different. Neutron irradiation of boron trioxide ($B_2O_3$) leads to the formation of oxygen and boron vacancies through nuclear collisions and, in particular, through the $^{10}B(n,\alpha)\,^{7}Li$ reaction, which produces energetic recoil atoms capable of generating displacement cascades [26]. In titanium carbide (TiC), fast neutrons create both carbon and titanium vacancies, although carbon sublattice defects are typically more prevalent due to their lower displacement threshold energy, resulting in non-stoichiometry and possible vacancy clustering [27]. In cubic 3C-SiC, neutron bombardment induces silicon and carbon Frenkel pairs, antisite defects, and defect clusters, which may evolve into extended defects such as dislocation loops under higher doses [28]. In hexagonal boron nitride (h-BN), neutron interactions promote boron and nitrogen vacancy formation, with boron-rich defect configurations often stabilized by transmutation reactions and local lattice distortion [29]. The accumulation and interaction of these primary point defects under sustained neutron flux can lead to complex defect structures, including vacancy clusters and amorphization, depending on irradiation temperature and fluence [30-31]. Proton and helium irradiation of TiNbCN and TiSiCN coatings generates primary knock-on atoms that produce Frenkel pairs, with carbon and nitrogen vacancies forming preferentially due to their lower displacement threshold energies compared with Ti, Nb, or Si atoms. In TiSiCN, irradiation can additionally promote defect segregation at grain boundaries and within the amorphous Si-containing intergranular phase, influencing vacancy recombination and cluster stabilization [32]. Tungsten-based composites exposed to proton and helium beams exhibit vacancy accumulation

and helium–vacancy complex formation, which may evolve into nano-cavities or bubble-like features at elevated fluence and temperature [33-34]. The overall defect evolution in these materials depends strongly on ion energy, fluence, and microstructural features such as grain size and free volume, which govern defect migration, recombination, and clustering processes. Electron and heavy-ion irradiation of $B_4C$ induces the formation of boron and carbon vacancies through displacement cascades, with heavy ions generating dense collision tracks that can locally amorphize the lattice and promote defect clustering [35]. In $ZrB_2$, energetic particles create zirconium and boron Frenkel pairs, and under high linear energy transfer conditions, vacancy aggregation may lead to dislocation loops or nanoscale defect complexes within the hexagonal lattice [36]. WC–6Co composites exposed to electron or heavy-ion beams exhibit vacancy formation both in the WC grains and in the cobalt binder phase, where radiation-enhanced diffusion can alter interfacial stability and promote defect segregation [37]. Heavy ions are particularly effective in producing localized thermal spikes, which facilitate the evolution of vacancy clusters, nano-cavities, or phase instability in these ceramics and cermets [38-39]. The extent of defect accumulation and structural modification depends on particle energy, fluence, and microstructural features such as grain size, binder distribution, and intrinsic free volume.

Examining in detail the works of Bordulev et al. [40] and Kudiiarov et al. [41], as well as following the logical thread from the introduction to this work of ours, we come to the conclusion that a magnesium base would be more suitable for our research. Continuing the logical sequence, we come to one of the main questions – "Could a better structural configuration be found at the nano level that would optimally determine the solution to the task we have set?". A similar dilemma is discussed in the work of Kudiiarov et al. [42], from 2023. From this, we can conclude that there is a collection of hydrogen in molecular form, which allows it to escape unhindered from the interior of the volume to the surface. At the same time, we should note that the participation of hydrogen in a chemical interaction with titanium is associated with the addition of additional energy [43], which practically facilitates our conclusions that chemical bonds are limited mainly to the molecular form of hydrogen. When we talk about adsorption of the produced hydrogen, we can mention several different methods. Alloys such as $TiFeH_2$ [44] and $Mg_2NiH_4$ [45] offer high capacity and reversible storage. On the other hand, the selective permeability of the polymer sites allows for controlled hydrogen release [46]. In this case, we recommend: Development of metal hydride-polymer hybrids adapted to extreme environments through material optimization and structural design [47]. Conducting experimental studies on radiation resistance and thermal cycling resistance [48]. Investigation of hybrid systems combining cryogenic adsorption with metal hydride-polymer technologies for synergistic benefits [49].

## 4. CONCLUSIONS

In titanium, chemical bonds in defects are mainly limited to the molecular form of hydrogen, while in iron there is an accumulation of hydride bonds with atoms close to the defect. Transport to the surface can be unhindered by the use of nanotubes made of low-valent material. In the adsorption of the formed molecular hydrogen, the development of a method for metal hydride-polymer hybrids adapted to extreme environments through material optimization and structural design, in combination with cryogenic adsorption, is recommended.

**Acknowledgements**

The authors wish to extend their sincere gratitude to Dr. E.P. Popov, Dr. S.F. Samadov, and Dr. of Sc. M.N. Mirzayev for their insightful recommendations and for providing essential support during the execution of this research.

**REFERENCES**

1. I.M. Peters, From fossil fuels to photovoltaics: Energy's role in human development and sustainability, EES Solar, Royal Society of Chemistry, 1 (2025) 712-723. DOI: 10.1039/D5EL00039D
2. Y. Zhao, M. Li, K. Wang, A. Sciacovelli, C. Qin, S. Lecompte, A.D. Thess. Thermo-mechanical energy storage technologies: Innovations, challenges and future directions. Front. Energy, 19(2) (2025) 115-116 DOI:10.1007/s11708-025-1007-3
3. P.W. Newton, P.W.G. Newman, S. Glackin, G. Thomson, Distributed green technologies for regenerating greyfields. In: Greening the Greyfields. Singapore. (2022) p71-87. https://doi.org/10.1007/978-981-16-6238-6_3
4. J. Zheng, L. Sun, X. Long, J. Wang, C. Li, Z. Mo, M. Du, T. Gao, E. Xia, B. Li, X. Xu, H. Xie, Electricity generation for lunar bases during construction and operation: Key technologies, challenges and development roadmap, Acta Astronautica, 236 (2025) 790-809. https://doi.org/10.1016/j.actaastro.2025.07.032
5. J. Bird, Z. Ao, A.C. Frey, N. Sell, A. Plummer, J.S.A. Dawe, O.J. Pountney, N. Sameh, S. Djurović, M.F. Iacchetti, A.C. Smith, C.M. Sangan, Cryogenic pumping of liquid hydrogen for aerospace propulsion, Progress in Aerospace Sciences, 160 (2026) 101155. https://doi.org/10.1016/j.paerosci.2025.101155
6. N.G. Primakov, Kazarnikov, V.V., Rudenko, V.A., & Gosudarstvennyj Nauchnyj Tsentr Rossijskoj Federatsii - Fiziko-Ehnergeticheskij Inst., Obninsk (Russian Federation). (1995).
7. E. Popov, T. Troev, L. Petrov, K. Berovski, S. Peneva, and B. Kolev, (2015).
8. N. Pushilina, A. Panin, M. Syrtanov, E. Kashkarov, V. Kudiiarov, O. Perevalova, R. Laptev, A. Lider, and A. Koptyug, Metals 8, 301 (2018).
9. E. Stepanova, N. Pushilina, M. Syrtanov, R. Laptev, and E. Kashkarov, International Journal of Hydrogen Energy 44, 29380 (2019).
10. R. Laptev, V. Kudiiarov, and N. Pushilina, Materials Today: Proceedings 19, 2084 (2019).
11. Y. S. Bordulev, R. S. Laptev, V. N. Kudiiarov, and A. M. Lider, AMR 880, 93 (2014).
12. A. A. Mikhaylov, T. S. Priamushko, M. N. Babikhina, V. N. Kudiiarov, R. Heller, R. S. Laptev, and A. M. Lider, Applied Surface Science 432, 85 (2018).
13. E. N. Stepanova, G. P. Grabovetskaya, I. P. Mishin, A. D. Teresov, and M. S. Syrtanov, in (Tomsk, Russia, 2018), p. 020295.
14. I. P. Mishin, G. P. Grabovetskaya, E. N. Stepanova, R. S. Laptev, and A. D. Teresov, Russ Phys J 62, 854 (2019).
15. A.M. Lider, V. V. Larionov, S. Xu, and R. S. Laptev, Russ J Nondestruct Test **55**, 928 (2019).
16. T. Torsti, M. Heiskanen, M.J. Puska, R.M. Nieminen, MIKA: multigrid-based program package for electronic structure calculations, Int. J. Quantum Chem. 91 (2) (2003) 171–176, https://doi.org/10.1002/qua.10397]
17. Boroński E, Nieminen RM (1986) Electron-positron density functional theory. Phys Rev B 34:3820–3831.
18. Sahni, V. (2004). The Hohenberg-Kohn Theorems and Kohn-Sham Density Functional Theory. In: Quantal Density Functional Theory. Springer, Berlin, Heidelberg. https://doi.org/10.1007/978-3-662-09624-6_4
19. M. Horbatsch, Independent particle model description of multiple ionization dynamics in fast ion-atom collisions, Phys. B Al. Mol. Opt. Phys. 25 (1592) 3797-3821.
20. M.N. Mirzayev, K.M. Hasanov, A.C. Parau et al., Effect of the C/N ratio modification on the corrosion behavior and performance of carbonitride coatings prepared by cathodic arc deposition, Journal of Materials Research and Technology, 27 (2023) p.1724-1738.

21. M.N. Mirzayev, M.Nasrabadi, N.Tiep et al., Determination of amorphization oxide layers, mobilization and functional groups on ZrC nanocrystals under high gamma irradiation, Vacuum, Volume 238, 2025, 114215, https://doi.org/10.1016/j.vacuum.2025.114215.
22. S.F. Samadov, O.A. Samedov, D.M. Mirzayeva et al., Effect of gamma irradiation and thermal annealing on defect formation in ZrB2 nanocrystals, Physica B: Condensed Matter, Volume 717, 2025, 417807, https://doi.org/10.1016/j.physb.2025.417807.
23. M.N. Mirzayev, Oxidation kinetics of boron carbide ceramic under high gamma irradiation dose in the high temperature, Ceramics International, 46 (3), (2020) p.2816-2822.
24. M.N. Mirzayev, A.S. Abiyev, O.A. Samedov ety al., Structural evolution of zirconium diboride under gamma irradiation and thermal annealing. Journal of Alloys and Compounds. 1005, 2024, 175970. https://doi.org/10.1016/j.jallcom.2024.175970
25. S.F. Samadov, A.G. Asadov, A.S. Abiyev et al., Evaluation of nanocrystalline ZrC under gamma irradiation and high pressure. Physica B: Condensed Matter. Volume 688, 2024, 416154. https://doi.org/10.1016/j.physb.2024.416154
26. S.F. Samadov, N.V.M. Trung, A.A. Donkov et al., Investigating the impact of gamma irradiation and temperature on vacancy formation and recombination in $ZrB_2$ ceramics using positron annihilation spectroscopy. Journal of Nuclear Materials. 599, 2024, 155242. https://doi.org/10.1016/j.jnucmat.2024.155
27. M.N. Mirzayev, Simultaneous measurements of heat flow rate and thermal properties of nano boron trioxide under neutron irradiation at the low and high temperature, Vacuum, 173 (2020) p.109162.
28. E. Popov, L. Slavov, E. Demir et al., Microstructural evolution of TiC nano powders under fast neutron irradiation: A multi-technique analysis, Vacuum, 215 (2023) p.112338.
29. M.N. Mirzayev, High-flux neutron irradiation of boron trioxide analyzed with Raman and FTIR spectroscopy, International Journal of Modern Physics B, 34 (18) (2020) p.2050160.
30. M.N. Mirzayev, B.A. Abdurakhimov, E. Demir et., Investigation of the formation of defects under fast neutrons and gamma irradiation in 3C-SiC nano powder, Physica B: Condensed Matter., 611 (2021) p. 412842.
31. M.N. Mirzayev, Heat transfer of hexagonal boron nitride (h-BN) compound up to 1 MeV neutron energy: Kinetics of the release of wigner energy, Radiation Physics and Chemistry, 180 (2021) p.109244.
32. M.N. Mirzayev, L.Slavov, A.Donkov et al., Effects of neutron irradiation at different fluencies on nanosized anatase titanium dioxide, Radiation Physics and Chemistry, 194 (2022) p.109988.
33. A. Vladescu, M.N. Mirzayev, A.S. Abiyev et al., Effect of Si and Nb additions on carbonitride coatings under proton irradiation: A comprehensive analysis of structural, mechanical, corrosion, and neutron activation properties, Nuclear Materials and Energy, 35 (2023) p.101457.
34. E. Demir, M.N. Mirzayev, E.P. Popov et al., Effects of high-energetic 3He+ ion irradiation on tungsten-based composites, Vacuum, 184 (2021) 109934.
35. D. Neov, L. Slavov, A.A. Donkov et al., Structural study of W2B obtained via mechanical alloying of W, B4C, TiC and graphite before and after He ions irradiation, Nuclear Materials and Energy, 31 (2022) p.101201
36. M.N. Mirzayev, Study thermodynamic assessment of the B-C and B-Si binary systems with swift heavy ions and high intense electron beam irradiation at the low temperature, Modern Physics Letters B, 34(34) (2020) p.2050395.
37. M.N. Mirzayev, E. Popov, E. Demir et al., Thermophysical behavior of boron nitride and boron trioxide ceramics compounds with high energy electron fluence and swift heavy ion irradiated, Journal of Alloys and Compounds, 834 (2020) p.155119.
38. S.F. Samadov, A.S. Abiyev, A.G. Asadov et al., Investigating the crystal structure of $ZrB_2$ under varied conditions of temperature, pressure, and swift heavy ion irradiation, Ceramics International, 2023, https://doi.org/10.1016/j.ceramint.2023.11.125
39. E. Demir, E.Popov, M. Mirzayev et al., Effects of swift heavy ions at different fluencies on WC-6Co hard metal alloy, International Journal of Refractory Metals and Hard Materials, 106 (2022) p.105865.
40. I. Bordulev, R. Laptev, V. Kudiiarov, R. Elman, A. Popov, D. Kabanov, I. Ushakov, and A. Lider, Materials 15, 1823 (2022).

41. V.N. Kudiiarov, A. Kenzhiyev, R. R. Elman, N. Kurdyumov, I. A. Ushakov, A. V. Tereshchenko, R.S. Laptev, M. A. Kruglyakov, and P. I. Khomidzoda, Metals 15, 72 (2025).
42. V. Kudiiarov, R. Elman, N. Kurdyumov, and R. Laptev, Journal of Alloys and Compounds 953, 170138 (2023).
43. A. Lider, V. Kudiiarov, E. Kashkarov, M. Syrtanov, T. Murashkina, A. Lomygin, I. Sakvin, D. Karpov, and A. Ivanov, Metals 10, 880 (2020).
44. E.M. Dematteis, N. Berti, F. Cuevas, M. Latroche, and M. Baricco, Mater. Adv. 2, 2524 (2021).
45. A. Alaoui-Belghiti, A. Assila, I. Belkoufa, M. Rkhis, S. Laasri, M. Tlemçani, E. Hlil, and A. Hajjaji, International Journal of Hydrogen Energy 92, 1069 (2024).
46. M. Tian, S. Rochat, K. Polak-Kraśna, L. T. Holyfield, A. D. Burrows, C. R. Bowen, and T. J. Mays, Adsorption 25, 889 (2019).
47. J. C. Crivello, B. Dam, R. V. Denys, M. Dornheim, D. M. Grant, J. Huot, T. R. Jensen, P. De Jongh, M. Latroche, C. Milanese, D. Milčius, G. S. Walker, C. J. Webb, C. Zlotea, and V. A. Yartys, Appl. Phys. A 122, 97 (2016).
48. V. Bérubé, G. Radtke, M. Dresselhaus, and G. Chen, Int. J. Energy Res. 31, 637 (2007).
49. K. J. Jeon, H.R. Moon, A.M. Ruminski, B. Jiang, C. Kisielowski, R. Bardhan, J. J. Urban, Nature Mater 10, 286 (2011).

JOURNAL OF BAKU ENGINEERING UNIVERSITY - PHYSICS
*2025. Volume 9, Number 2* *Pages 73-81*

*UDC:535.34:535.375:537.311.322*
*DOI: https://doi.org/10.30546/09081.2025.002.1018*

# CORRELATING VIBRATIONAL, OPTICAL, AND PHOTOELECTRICAL RESPONSES IN GES SINGLE CRYSTALS

**Sevinj GULIYEVA*[1], Lamiya BALAYEVA[1], Ali GUSEINOV[1]**

[1]*Department of Semiconductor physics, Baku State University, 23 Academic Zahid Khalilov Street, Baku AZ1148, Azerbaijan*

***ARTICLE INFO***

*Article history:*
*Received: 2025-06-09*
*Received in revised form:2025-06-18*
*Accepted:2025-07-20*
*Available online:2025-12-21*

*Keywords:*
*Layered crystal;*
*Raman spectroscopy;*
*Direct and indirect band gap transition;*
*Spectral characteristics*



***ABSTRACT***

*High-quality GeS single crystals were grown using the Bridgman method and systematically investigated to elucidate their vibrational, optical, and photoelectrical properties. Raman spectroscopy revealed well-defined $A_1g$, $B_2g$, and $A_2g$ vibrational modes characteristic of orthorhombic layered GeS, indicating high crystallinity, phase purity, and low defect density. The narrow Raman linewidths and relatively long phonon lifetime suggest weak phonon scattering and good lattice ordering. Optical characterization performed by UV–Vis absorption spectroscopy demonstrated the presence of both indirect and direct optical transitions. The indirect band gap was determined to be approximately 1.59 eV with a phonon energy of 54.5 meV, while the direct band gap was estimated to be around 1.67 eV, confirming the semiconducting nature of GeS. Photocurrent measurements revealed a pronounced energy-dependent photoresponse, with the photocurrent reaching a maximum near 1.5 eV, close to the band-edge region, indicating efficient photogenerated carrier generation. At higher photon energies, the decrease in photocurrent was attributed to enhanced carrier recombination and trapping effects. The combined results demonstrate that the synthesized GeS single crystals exhibit favorable structural quality and optoelectronic performance, highlighting their potential for optoelectronic and photodetection applications.*

## 1. INTRODUCTION

Semiconducting materials play a fundamental role in modern technology and scientific research, owing to their tunable electronic, optical, and structural properties. Comprehensive investigation of their functional characteristics continues to broaden their prospective applications in advanced device architectures and emerging technological fields [1–3]. Among these materials, layered semiconductor crystals have gained increasing attention due to their exceptional optoelectronic, photovoltaic, and mechanical properties, positioning them as promising candidates for next-generation electronic and photonic systems [8–10]. Germanium monosulfide (GeS) is one such material that has emerged as a highly attractive monochalcogenide compound.

GeS stands out for its unique structural attributes, chemical stability, and wide range of potential applications. Composed of environmentally benign and earth-abundant elements, GeS exhibits high thermodynamic and chemical stability, which enhances its suitability for practical technological implementations [11]. The combination of germanium and sulfur forms a semiconductor with an intermediate band gap in the visible range, enabling efficient absorption of sunlight. As a result, GeS effectively utilizes the solar spectrum reaching the Earth's surface, making it a promising material for high-performance solar-energy conversion systems. Due to

these advantageous properties, GeS has been considered for numerous optoelectronic and electronic applications, such as field-effect transistors, photovoltaic devices, photodetectors, infrared sensors, and other multifunctional nanoscale components [12–17]. Structurally, GeS is a layered material in which each layer consists of strongly covalently bonded Ge and S atoms, while adjacent layers interact through weak van der Waals forces. This layered nature allows the crystal to be readily exfoliated into ultrathin sheets, similar to other two-dimensional (2D) materials, thereby extending its functionality in low-dimensional material systems [4]. The orthorhombic layered structure of GeS results in a high surface-to-volume ratio, significantly enhancing surface-related phonon interactions and exerting a profound influence on its vibrational and optical properties [6,7]. GeS exhibits a distorted orthorhombic crystal structure analogous to that of black phosphorus, along with an indirect band gap located in the visible spectral region. These structural features impart strong anisotropy to the material, making it an appealing candidate for applications that require direction-dependent optical or electronic responses [18–20]. The Ge–S bond possesses a partially ionic character, which leads to an asymmetric charge distribution and induces distortions in the $sp^3$ hybridization within the tetrahedral coordination environment [6]. This intrinsic structural asymmetry directly contributes to the pronounced anisotropic behavior observed in the optical absorption, vibrational dynamics, charge transport, and light–matter interaction processes within GeS [6,7].

Despite its potential, the fabrication of high-quality GeS single crystals presents significant challenges. The structural integrity, defect concentration, and overall crystalline quality are highly dependent on the chosen synthesis route, thermal treatment, and doping strategies. Even under optimized growth conditions, layered GeS crystals frequently contain intrinsic point defects, which play a decisive role in determining their electronic and optoelectronic properties [5]. Thus, understanding the nature, formation mechanisms, and energetic characteristics of these native defects is crucial for tailoring GeS-based materials toward high-performance device applications. Therefore, in this study, the structural and optical properties of GeS crystals were systematically investigated, and their potential application prospects were thoroughly evaluated.

## 2. EXPERIMENTAL DETAILS

### *2.1. Synthesis of GeS and growing single crystal*

The crystal growth was carried out in two distinct stages [21]. Initially, high-purity elemental germanium (99.9999%) and sulfur (99.9999%) were accurately weighed in a 1:1 molar ratio and loaded into a quartz ampoule. Prior to loading, the ampoule was chemically cleaned, rinsed with deionized water, dried, and evacuated to $10^{-5}$ Pa to remove adsorbed moisture, oxygen, and volatile contaminants. Once the required vacuum level was achieved, the ampoule was hermetically sealed, ensuring an airtight and mechanically stable environment capable of withstanding internal pressure variations during subsequent heating. Following hermetic sealing, the ampoule was positioned horizontally in a furnace and subjected to a controlled heating protocol using the direct melting method (Figure 1). To prevent rapid sulfur volatilization, the sulfur-rich section of the charge was initially preheated to 150–200 °C, enabling gradual sublimation and promoting uniform diffusion of sulfur into the germanium precursor. The reaction zone was then heated to approximately 700–750 °C, a temperature above the congruent melting point of GeS, ensuring complete liquefaction and chemical homogenization of the melt. Once homogenization was achieved, the molten charge was translated along the

imposed thermal gradient to initiate directional solidification, yielding a polycrystalline GeS ingot. This material was subsequently processed to prepare seed crystals. In the second stage, the seeds were placed at the cooler end of a newly loaded and hermetically sealed ampoule, and directional solidification was initiated from the seed, propagating through the melt to produce a high-quality monocrystalline GeS crystal. Controlled cooling to room temperature preserved structural integrity and minimized thermally induced defects. Preliminary characterization of the obtained sample was conducted using optical microscopy, and the resulting micrograph is presented in Figure 2. During optical microscopic examination in both transmitted and reflected illumination modes, the GeS crystal exhibited a characteristic purple–violet contrast, which is attributed to the combined effects of its layered crystal structure, optical absorption profile, and thickness-dependent interference phenomena. Since GeS possesses a band gap of approximately 1.6–1.7 eV, it strongly absorbs in the green region of the visible spectrum, while preferentially transmitting red and blue components, resulting in a purple appearance for thin sections under transmitted light. Moreover, local variations in crystal thickness and strain-induced structural inhomogeneity give rise to interference fringes and contrast modulations, which manifest as distinct stripe-like features across the micrograph. Several dark inclusions and particulate accumulations were also observed, most likely originating from residual polishing debris and mechanically induced microdefects formed during sample preparation. Overall, the observed optical features are consistent with the intrinsic layered nature of GeS and confirm the structural integrity of the grown crystal.

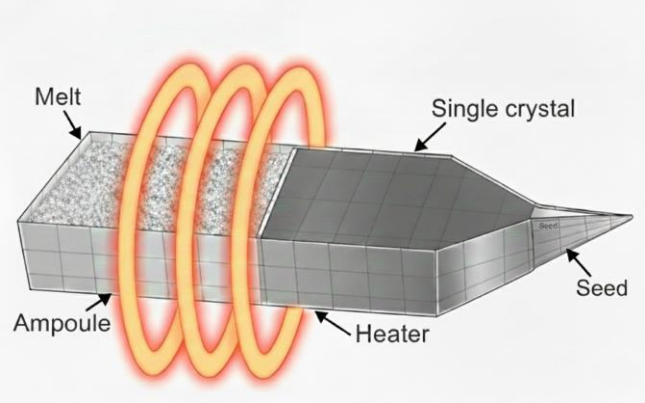


***Fig. 1*** *Schematic illustration of GeS crystal growth by the Horizontal Bridgman method*

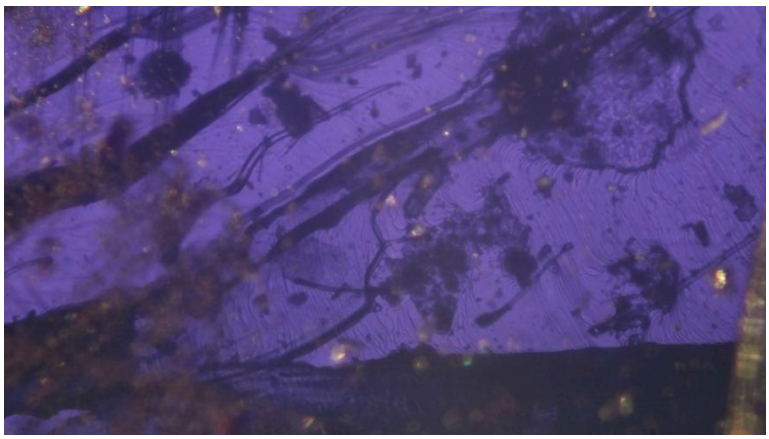

***Fig. 1*** *The optical microscope image the as-grown GeS ingot obtained by the horizontal Bridgman method*

### *2.2. Characterization techniques*

The electrical and photoelectric characteristics of the samples were examined under high-vacuum conditions using a closed-cycle cryostat system. This setup enabled comprehensive measurements across a broad temperature range from 110 K to 400 K and within the optical spectral range of 480–2000 nm, facilitating the investigation of temperature-dependent carrier transport and spectral response behavior.

To evaluate photocurrent dynamics, a set of advanced optoelectronic instrumentation was employed. A SOLARIS Nd:YAG pulsed laser served as the excitation source, while a high-resolution M833 double-dispersion monochromator was used to select specific wavelengths. Photocurrent signals were detected using a HAMAMATSU S7031-1006S photodetector, known for its high sensitivity in the visible and near-infrared regions.

The optical properties of the samples were investigated using a Specord 250 Plus UV–Vis Spectrophotometer in the wavelength range of 190–1100 nm.

The vibrational characteristics of the GeS crystals were analyzed by Raman spectroscopy using an EnSpectr R532 Raman spectrometer (Enhanced Spectrometry Inc., USA) under excitation with a green laser source ($\lambda$ = 532 nm). The spectra were collected in the backscattering geometry at room temperature with an optimized laser power to prevent local heating effects.

## 3. RESULTS AND DISCUSSION

### *3.1. Vibrational characteristics by Raman spectroscopy*

The structural and vibrational properties of the synthesized GeS single crystals were systematically investigated using Raman spectroscopy, which serves as a sensitive and non-destructive tool for probing lattice dynamics, phonon behavior, and crystal symmetry. The experimentally obtained Raman spectrum is presented in Figure 3, where the characteristic vibrational modes of GeS are clearly resolved. As shown in Figure 3, the Raman spectrum exhibits several well-defined and intense peaks, indicating a high degree of crystallinity. Prominent Raman-active modes are observed at approximately 214.9, 245.2, and 266.9 $cm^{-1}$, which are assigned to the $A_1g$, $B_2g$, and $A_2g$ symmetry modes, respectively. These modes are characteristic of orthorhombic layered GeS and arise from symmetry-allowed atomic displacement patterns within the crystal lattice. In particular, the dominant $A_2g$ mode originates from the symmetric stretching vibrations of the bonds between Ge and S, reflecting strong intralayer covalent bonding. In addition, Figure 3 reveals several weaker Raman features at approximately 212.7, 221.4, 234.4, and 290.7 $cm^{-1}$. The peaks near 212.7 and 221.4 $cm^{-1}$ are attributed to interlayer shear and breathing modes, which arise from relative vibrations between adjacent GeS layers and are indicative of interlayer coupling in this layered material. The mode around 234.4 $cm^{-1}$ is likely associated with defect or strain-induced phonon activation, resulting from local lattice distortions that relax the Raman selection rules. The higher-frequency feature observed near 290.7 $cm^{-1}$ is interpreted as a second-order Raman process, corresponding to an overtone or combination mode arising from phonon–phonon interactions.

The phonon energies corresponding to the experimentally observed Raman-active modes were quantitatively determined from the measured peak positions and converted into energy units. These phonon energies, arranged in ascending order, were found to be 26.38, 26.64, 27.45, 29.07, 30.43, 33.09, and 36.05 meV. The relatively narrow energy spacing between the low-energy

modes reflects the presence of closely related vibrational processes, particularly those associated with interlayer and low-frequency optical phonons, which are characteristic of layered orthorhombic GeS. The phonon lifetime corresponding to the most intense Raman peak was estimated to be approximately 51.9 fs. This relatively long phonon lifetime indicates weak phonon scattering mechanisms within the crystal, suggesting a low contribution from defect-induced scattering, impurity effects, and phonon–phonon anharmonic interactions. Consequently, energy dissipation within the lattice is reduced, which is indicative of a well-ordered crystal structure.

Moreover, the narrow linewidths observed for all prominent Raman peaks further corroborate the high structural quality of the synthesized GeS single crystals. Narrow Raman linewidths are typically associated with minimal lattice disorder, low strain inhomogeneity, and a reduced density of crystallographic defects such as vacancies, dislocations, or grain boundaries. This observation confirms the effectiveness of the Bridgman growth method in producing GeS single crystals with excellent crystalline uniformity.

From a broader perspective, the presence of well-resolved Raman modes together with narrow spectral linewidths and relatively long phonon lifetimes indicates low anharmonicity and strong phonon coherence in the synthesized GeS crystals. These characteristics imply reduced phonon scattering and confirm the high structural quality of the material.

The Raman-active modes measured in this work, including their peak positions and phonon energies, show good agreement with previous reports [7], indicating that our experimental results accurately reflect the characteristic vibrational behavior of GeS as reported in the literature.

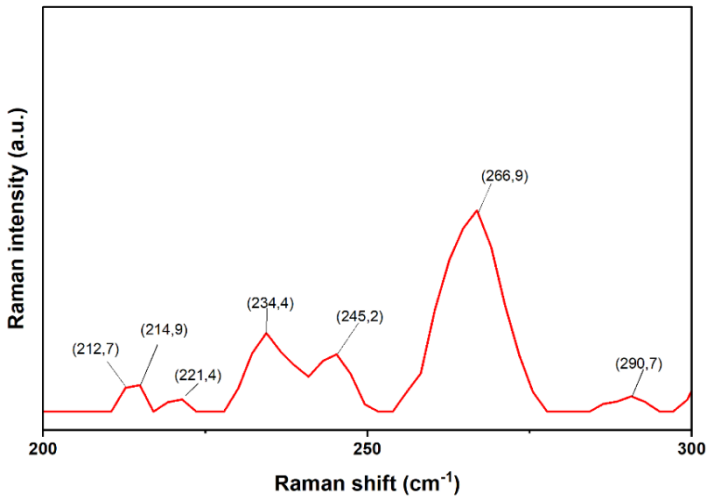


***Fig. 3*** *Raman spectrum of GeS single crystal obtained at room temperature*

### *3.2. Optical characterization via Uv-Vis spectroscopy*

The optical properties of the GeS single crystals were investigated using UV–Vis absorption spectroscopy, which provides accurate measurements of the absorption coefficient across a wide photon energy range. The absorption data were analyzed using the Tauc plot method, a widely used technique for determining the optical band gap of semiconducting materials. Analysis of the Tauc plot reveals that the GeS crystal exhibits both direct and indirect optical transitions. The optical band gap was determined separately for each case. The direct band gap corresponds to transitions in which the valence band maximum and conduction band minimum occur at the

same k-point in the Brillouin zone, allowing photon absorption without phonon assistance. In contrast, the indirect band gap involves transitions between different k-points, requiring phonon absorption or emission to conserve momentum. Accordingly, the Tauc plot analysis was performed for both types of transitions to accurately evaluate the corresponding band gap energies.

For the indirect band gap n=1/2 (Figure 4a.), two distinct linear regions are observed in the Tauc plot, corresponding to phonon-assisted transitions. The higher-energy linear region intersects the photon energy axis at 1.644 eV, while the lower-energy region intersects at 1.535 eV. The indirect band gap was calculated as the average of these two values, resulting in Eg=1.590eV, with a corresponding phonon energy $E_{ph}$ =54.5meV.

For GeS, the parameter n=2 was applied in the Tauc relation, corresponding to a direct allowed transition. In the low-energy region, spanning photon energies from approximately 1.25 to 1.6 eV (Figure 4b.), the absorption coefficient remains nearly zero, indicating that the photon energy (hν) is insufficient to excite electrons from the valence band to the conduction band (hν<$E_g$ ). Beyond 1.6 eV, a sharp increase in absorption is observed, marking the onset of the fundamental absorption edge. The direct band gap was determined by extrapolating thelinear portion of the high-absorption region, yielding $E_g$ =1.669eV.

The direct and indirect optical band gaps measured in this work, including the phonon-assisted features observed in the Tauc plots, show good agreement with previous reports [22], indicating that our experimental results accurately reflect the characteristic optical behavior of GeS as reported in the literature.

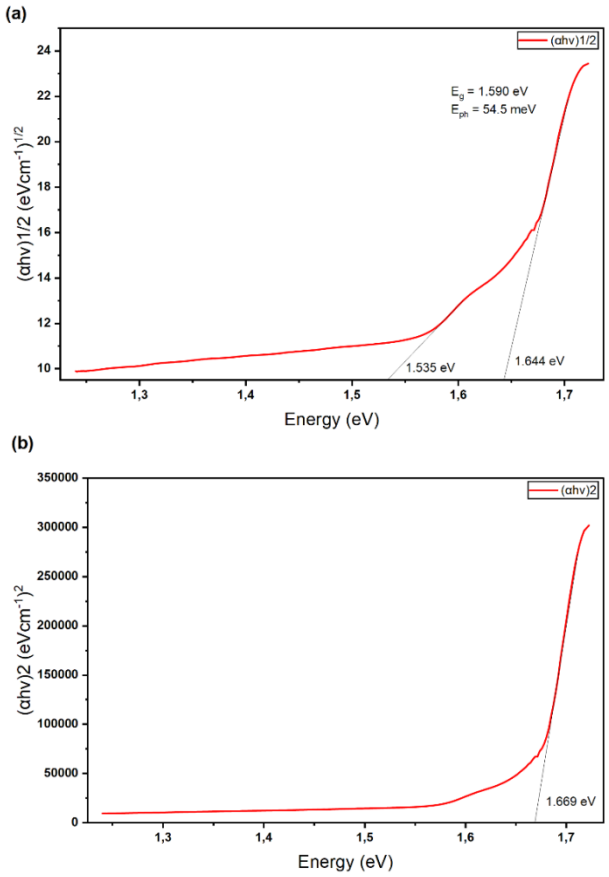


***Fig. 4*** *UV–Vis absorption spectrum of direct (b) and indirect (a) transition*

### 3.3. Photocurrent generation and temporal response

Based on the graph obtained to investigate the energy dependence of photoconductivity, the photoelectrical response of the sample was analyzed in detail (Figure 5). During the measurements, variations in the photocurrent as a function of photon energy were recorded, allowing the identification of the main electronic processes occurring within the material. The graph reveals that as the photon energy increases, the photocurrent initially rises, reaches a maximum within a specific energy range, and subsequently exhibits a decreasing trend.

With increasing photon energy, the photocurrent intensity reaches a maximum at approximately 1.5 eV, which corresponds to the energy range where electronic transitions from the valence band to the conduction band occur most efficiently. Since this energy range is close to the band gap of the material, the probability of electron and hole pair generation due to photon absorption is maximized. As a result, the GeS crystal exhibits high photoactivity in this region, and the concentration of free carriers generated by illumination increases significantly.

When the photon energy exceeds 1.5 eV, the photoexcited electrons acquire higher energy and are promoted to the conduction band with increased kinetic energy. Although this initially enhances carrier mobility, it also gives rise to several adverse effects. High-energy electrons are more easily trapped by defect states and surface traps present in the crystal lattice. In these trap states, electrons rapidly recombine with holes in the valence band, resulting in a reduction in the effective carrier lifetime. Thus, the decrease in photocurrent observed at photon energies above 1.5 eV is mainly attributed to the enhanced recombination processes and the saturation effect. The obtained results clearly reflect the optical absorption characteristics of the GeS crystal, the relationship between the band gap width and photoconductivity, and the carrier dynamics within the material. This analysis demonstrates that GeS is a promising material for optoelectronic applications and highlights the energy-dependent mechanisms governing its photoelectrical behavior.

The energy-dependent photocurrent behavior observed in this work, including the peak near 1.5 eV and the subsequent decrease due to recombination and trap states, is in good agreement with previously reported broadband photodetection and polarization-sensitive measurements in GeS devices [23,24], indicating that our experimental results accurately reflect the characteristic optoelectronic behavior of GeS as reported in the literature.

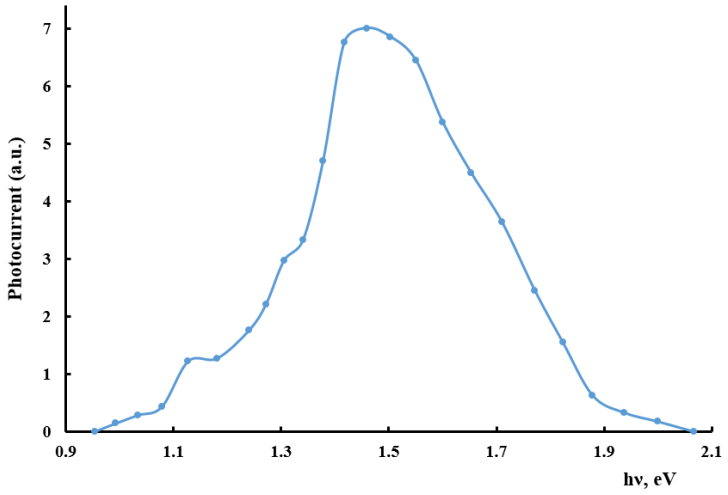


***Fig. 4*** *Spectral characteristics of GeS crystal*

## 4. CONCLUSION

High-quality GeS single crystals were successfully synthesized using the Bridgman growth method, and their structural, vibrational, optical, and photoelectrical properties were systematically investigated. Raman spectroscopy revealed well-resolved and intense vibrational modes corresponding to the characteristic $A_1g$, $B_2g$, and $A_2g$ symmetries of orthorhombic layered GeS, confirming the high crystallinity and phase purity of the grown crystals. The presence of narrow Raman linewidths and a relatively long phonon lifetime indicates weak phonon scattering, low defect density, and excellent structural uniformity.

Optical characterization performed by UV–Vis absorption spectroscopy demonstrated that the GeS single crystals exhibit both direct and indirect optical band gaps. The indirect band gap was determined to be approximately 1.59 eV, with a corresponding phonon energy of 54.5 meV, while the direct band gap was estimated as 1.67 eV.

Photocurrent generation measurements revealed a strong energy-dependent photoresponse, with the photocurrent reaching a maximum near 1.5 eV, close to the optical band gap of the material. This behavior indicates efficient photogenerated carrier creation in the band-edge region. At higher photon energies, the observed decrease in photocurrent was attributed to enhanced carrier recombination and trapping effects, highlighting the role of defect states in governing charge transport dynamics.

Overall, the combined vibrational, optical, and photoelectrical analyses confirm that the synthesized GeS single crystals possess excellent structural quality and favorable optoelectronic properties. These findings demonstrate the potential of GeS as a promising material for optoelectronic and photodetection applications.

***Reference list***


1. Georgobiani, A.N., Tagiev, B.G., Guseinov, G.G., Kerimova, T.G., Tagiev, O.B., Asadullaeva, S.G. (2010). Structure and photoluminescence of ZnGa2Se4:Eu2+. Inorganic Materials, 46, 456-459.
2. Alekperov, A.S., Jabarov, S.H., Mirzayev, M.N., Asgerov, E.B., Ismayilova, N.A. Aliyev, Y.I., Thabethe, T.T., Dang, N.T. (2019). Effect of gamma irradiation on microstructure of the layered Ge0.995Nd0.005S. Modern Physics Letters B, 33(09), 1950104.
3. Tagiev, B.G., Kerimova, T.G., Tagiev, O.B., Asadullayeva, S.G., Mamedova, I.A. (2012). Optical transitions in MnGa2Se4. Semiconductors, 46, 705-707.
4. Ramasamy, P., Kwak, D., Lim, D.-H., Ra, H.-S. & Lee, J.-S. (2016). *Solution synthesis of GeS and GeSe nanosheets for high-sensitivity photodetectors.* J. Mater. Chem. C, 4, 479–485.
5. Bletskan, D. I., Madyar, I. I., Mikulaninets, S. V., & Sichka, M. Yu. (2000). *Electrical and photoelectric properties of GeS layered crystals grown by different techniques*. *Inorganic Materials, 36*(6), 544–550.
6. Tołłoczko, A., Oliva, R., Woźniak, T., Kopaczek, J., Scharoch, P., & Kudrawiec, R. (2020). *Anisotropic optical properties of GeS investigated by optical absorption and photoreflectance*. *Materials Advances, 1*, 1886– 1894.
7. Zawadzka, N., Kipczak, Ł., Woźniak, T., Olkowska-Pucko, K., Grzeszczyk, M., Babiński, A., & Molas, M. R. (2021). *Anisotropic optical and vibrational properties of GeS*. *Nanomaterials, 11*(11), 3109.
8. Buscema, M., Island, J.O., Groenendijk, D.J., Blanter, S.I., Steele, G.A., Zanta, H.S.J., Castellanos Gomez, A. (2015). Photocurrent generation with two-dimensional van der Waals semiconductors. Chemical Society Reviews, 44, 3691-3718.
9. Furchi, M., Pospischil, A., Libisch, F., Burgdorfer, J., Mueller T. (2014). Photovoltaic effect in an electrically tunable van der Waals heterojunction. Nano Letters, 14(8), 4785-4791.
10. Asadullayeva, S. G., Dashdemirov, A. O., Alekperov, A. S., Ismayilova, N. A., Hadieva, A. A., Cafarova, A. N., &

Abiyev, A. S. (2023). Infrared luminescence of GeS:Nd layered crystals. *Advanced Physical Research, 5*(1), 12–18.

11. Feng, M., Liu, S.-C., Hu, L., Wu, J., Liu, X., Xue, D.-J., Hu, J.-S. & Wan, L.-J. (2021). *Interfacial Strain Engineering in Wide-Bandgap GeS Thin Films for Photovoltaics. Journal of the American Chemical Society, 143*(25), 9664-9671.
12. Ding, Y.; Liu, Y.-S.; Yang, G.; Gu, Y.; Fan, Q.; Lu, N.; Zhao, H.; Yu, Y.; Zhang, X.; Huo, X.; et al. High-Performance Ballistic Quantum Transport of Sub-10 nm Monolayer GeS Field-Effect Transistors. *ACS Appl. Electron. Mater.* **2021**, *3*, 1151–1161
13. Kumar Ulaganathan, R.; Lu, Y.-Y.; Kuo, C.-J.; Reddy Tamalampudi, S.; Sankar, R.; Moorthy Boopathi, K.; Anand, A.; Yadav, K.; Jesus Mathew, R.; Liu, C.-R.; et al. High photosensitivity and broad spectral response of multi-layered germanium sulfide transistors. *Nanoscale* **2016**, *8*, 2284–2292.
14. Li, H.; Wang, Q.; Liu, F.; Lu, J. Lifting on-state currents for GeS-based tunneling field-effect transistors with electrode optimization. *Appl. Surf. Sci.* **2022**, *602*, 154297.
15. Ramasamy, P.; Kwak, D.; Lim, D.-H.; Ra, H.-S.; Lee, J.-S. Solution synthesis of GeS and GeSe nanosheets for high-sensitivity photodetectors. *J. Mater. Chem. C* **2016**, *4*, 479–485.
16. Vaughn, D.D.; Patel, R.J.; Hickner, M.A.; Schaak, R.E. Single-Crystal Colloidal Nanosheets of GeS and GeSe. *J. Am. Chem. Soc.* **2010**, *132*, 15170–15172.
17. Grodzicki, M., Tołłoczko, A. K., Majchrzak, D., Hommel, D., & Kudrawiec, R. (2022). Band Alignments of GeS and GeSe Materials. *Crystals, 12*(10), 1492.
18. Lan, C., Li, C., Yin, Y., Guo, H., & Wang, S. (2015). Synthesis of single-crystalline GeS nanoribbons for high-sensitivity visible-light photodetectors. *Journal of Materials Chemistry C, 3*, 8074–8079.
19. Ulaganathan, R. K. et al. High photosensitivity and broad spectral response of multi-layered germanium sulfide transistors. Nanoscale 8, 2284–2292 (2016).
20. Chen, Z., Hwang, W., Kim, D. H., Kim, Y. D., Cho, M., Hoang, A. T., Kim, H. J., Kim, M., Kim, D., Ahn, J.-H., Soon, A., & Choi, H.-J. (2022). In-plane optical and electrical anisotropy in low-symmetry layered GeS microribbons. *NPG Asia Materials, 14*, 41.
21. Balayeva, L., Guseinov, A., & Akhmedova, F. (2025). Synthesis and characterization of Ga0. 997B0. 003Se crystal for ultrafast optoelectronic applications. Optical and Quantum Electronics, 58(1), 12.
22. Arfaoui, M., Zawadzka, N., Ayari, S., Chen, Z., Watanabe, K., Taniguchi, T., Babiński, A., Koperski, M., Jaziri, S., & Molas, M. R. (2023). *Optical properties of orthorhombic germanium sulfide: unveiling the anisotropic nature of Wannier excitons*. Nanoscale, 15, 17014–17028.
23. Zawadzka, K.; et al. *High photosensitivity and broad spectral response of multi-layered germanium sulfide transistors.* Nanoscale, 2016, 8, 207–215.
24. Ghosh, S.; et al. *Layer-dependent polarization-sensitive photodetection in GeS nanosheets.* Nanoscale, 2017, 9, 1234–1243.

JOURNAL OF BAKU ENGINEERING UNIVERSITY - PHYSICS
*2025. Volume 9, Number 2* *Pages 82-91*

*UDC: 544.18:577.112.3.*
*DOI: https://doi.org/10.30546/09081.2025.002.1023*

# DFT STUDY OF THE STRUCTURAL AND ELECTRONIC FEATURES OF THE ALA-TYR DIPEPTIDE

**Sara RAHIMZADE[1]* and Gulnara AKVERDIEVA[2]**

[1]*Physics Faculty, Baku State University, Baku, Azerbaijan*

[2]*Institute for Physical Problems, Baku State University, Baku, Azerbaijan*

***ARTICLE INFO***

*Article history:*
*Received:2025-03-30*
*Received in revised form:2025-04-20*
*Accepted:2025-06-05*
*Available online:2025-12-21*

*Keywords:*
*DFT; Ala-Tyr dipeptide; HOMO-LUMO; MEP; hydrogen bonding; reactivity descriptors.*



***ABSTRACT***

*In this work, the stable conformations of the Ala -Tyr (alanine-tyrosine) dipeptide were investigated in water environment at the B3LYP/6-31+G(d,p) level of density functional theory (DFT). The geometric parameters (bond lengths, valence angles, dihedral angles), including the intramolecular hydrogen bonds, electron distribution and related properties such as Mulliken atomic charges, Molecular Electrostatic Potential (MEP), and Frontier Molecular Orbitals (HOMO and LUMO) of the dipeptide were analyzed in detail. The results show that significant structural differences exist between the two energetically possible conformations, which are reflected in the specific electron distribution and, accordingly, in the values of the energy gap and the dipole moment. Also, the hydrogen atoms of the α-amino group and the oxygen atoms of the C-terminal carboxyl group play a key role in the reactivity and biological activity of this molecule. The research work contributes to study the structure-activity relationships of the Ala-Tyr dipeptide at the quantum-chemical level, for understanding of its potential applications in drug design.*

## 1. INTRODUCTION

The study of the conformational properties of peptide molecules and the performance of molecular modeling based on quantum mechanical calculations allow us to obtain conclusions about their atomic-level structure and functional properties. Among peptides with biomedical applications, dipeptides and tripeptides are particularly suitable due to their structural simplicity and are widely used in the design of new therapeutic drugs and in the food industry. Dipeptides are short peptide molecules formed by the combination of two amino acids by a peptide bond and play an important role in various biological processes such as protein synthesis, nutrient absorption, cell signaling, and immune response. Dipeptides are widely used in the biomedical field due to their bioavailability and non-toxicity. Such short molecules can also be applied for purposes such as the identification and purification of various substances [1].

Dipeptides containing Tyr and Trp amino acids and protein hydrolysates rich in these dipeptides can be considered as potential functional food components for the protection and improvement of human health [2]. The Ala-Tyr dipeptide, which is used as a biologically active additive, is mainly known as an angiotensin-converting enzyme (ACE) inhibitor [3-4]. It has been shown in [5] that this dipeptide is rapidly hydrolyzed in blood plasma, which indicates its favorable use in the body. Even in hemodialysis patients with chronic renal failure, the breakdown and excretion of Ala-Tyr from the body is normal. That is, even if the kidney function is weakened, Ala-Tyr is effectively metabolized and does not cause problems.

In the presented work, the geometric parameters and electronic properties such as HOMO/LUMO energies, energy gap, dipole moment, partial charges of atoms, electron density distribution, and reactivity descriptors of Ala-Tyr dipeptide were studied using the DFT method.

## 2. METHODS

Quantum chemical calculations of polyatomic molecules allow us to determine or predict the geometric structure, energy, dipole moment, ionization potential, charge distribution, and various other physical and chemical properties of molecules. Experimental data show that the results of such calculations are quite reliable. Naturally, since it is impossible to take into account all the factors encountered during the experiment, the accuracy of quantum chemical calculation methods in most cases coincides with experimental results, even if there are certain limitations in the accuracy of the results obtained. The main task of computer modeling is to correctly formulate the goals of the research and provide a detailed analysis of the obtained calculation results.

The density functional theory (DFT) used in this work replaces the multiparticle electron wave function with the electron density as the main physical quantity in order to eliminate both the inaccuracy of the Hartree-Fock method and the high computational requirements. That is, DFT allows us to calculate all the physical and chemical properties of the system based on the electron density [6].

First, the conformational profiles of the Ala-Tyr dipeptide were investigated by molecular mechanics (MM) and it was shown that this molecule can exist in two stable states corresponding to the extended and folded conformations [7]. Then, using the coordinates obtained from results of MM calculations as initial geometric parameters the most stable extended and folded conformations of the bioactive dipeptide Ala-Tyr were optimized in an water environment by the DFT/B3LYP [8] method using the 6-31+G(d,p) basis set. Here, the Gaussian 16 software package [9] and GaussView 6.0 [10] were used as software.

## 3. RESULTS AND DISCUSSIONS

Figure 1 shows the optimized extended and folded structures of the Ala-Tyr dipeptide calculated using the DFT/B3LYP/6-31+G(d,p) method.

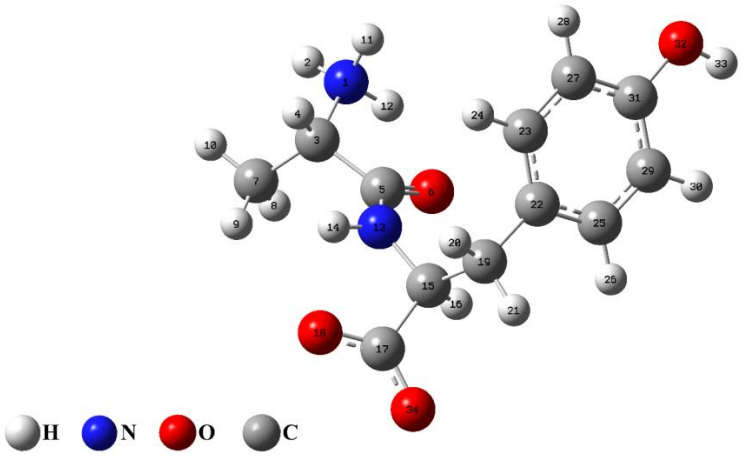


*(a)*

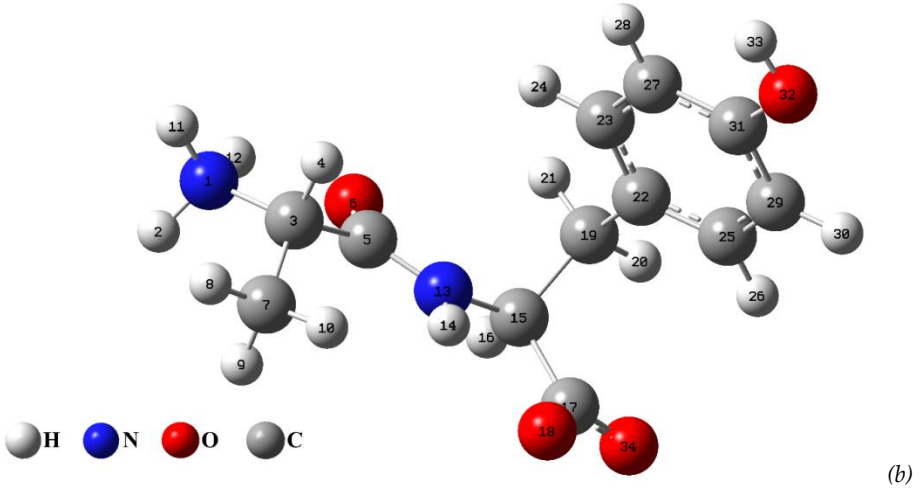


***Fig 1.*** *Optimized extended (a) and folded (b) structures of the Ala-Tyr dipeptide*

Tables 1 and 2 show and compare the calculated values of the geometric parameters (bond lengths and valence angles) of the optimized structures of the dipeptide with the values obtained from experimental studies for the constituent amino acid residues of the dipeptide. As a result of the comparison, it is seen that there are slight differences between the values of the bond angles and bond lengths of both the main and side chains of the Ala-Tyr dipeptide and the experimental values. Table 3 shows the dihedral angles for both stable structures of the dipeptide.

***Table 1.*** *Calculated and experimental values of bond lengths (Å) for amino acid residues of the Ala-Tyr dipeptide (Å)*

| Bond lengths | Extended structure | Folded structure | [11, 12] |
|---|---|---|---|
| N1-H2 | 1.023 | 1.024 | 1.029 |
| N1-H11 | 1.024 | 1.022 | 1.047 |
| N1-H12 | 1.036 | 1.040 | 1.031 |
| N1-C3 | 1.509 | 1.509 | 1.487 |
| C3-H4 | 1.091 | 1.094 | 1.093 |
| C3-C5 | 1.546 | 1.550 | 1.531 |
| C3-C7 | 1.531 | 1.528 | 1.524 |
| C5-O6 | 1.243 | 1.246 | 1.242 |
| C5-N13 | 1.334 | 1.330 | - |
| C7-H8 | 1.094 | 1.093 | 1.082 |
| C7-H9 | 1.092 | 1.094 | 1.081 |
| C7-H10 | 1.093 | 1.092 | 1.081 |
| N13-H14 | 1.019 | 1.019 | 0.850 |
| N13-C15 | 1.463 | 1.463 | 1.493 |
| C15-H16 | 1.092 | 1.095 | 0.960 |
| C15-C17 | 1.561 | 1.559 | 1.531 |
| C15-C19 | 1.553 | 1.553 | 1.535 |
| C17-O18 | 1.265 | 1.265 | 1.257 |
| C17-O34 | 1.258 | 1.258 | 1.243 |
| C19-H20 | 1.096 | 1.094 | 1.030 |
| C19-H21 | 1.095 | 1.095 | 0.960 |
| C19-C22 | 1.513 | 1.514 | 1.516 |
| C22-C23 | 1.403 | 1.403 | 1.393 |
| C22-C25 | 1.403 | 1.405 | 1.395 |
| C23-H24 | 1.087 | 1.087 | 1.020 |
| C23-C27 | 1.397 | 1.398 | 1.393 |

| | | | |
|---|---|---|---|
| C25-H26 | 1.087 | 1.086 | 0.940 |
| C25-C29 | 1.397 | 1.395 | 1.386 |
| C27-H28 | 1.086 | 1.087 | 0.960 |
| C27-C31 | 1.398 | 1.399 | 1.390 |
| C29-H30 | 1.087 | 1.086 | 0.930 |
| C29-C31 | 1.400 | 1.399 | 1.384 |
| C31-032 | 1.375 | 1.375 | 1.369 |
| O32-H33 | 0.968 | 0.968 | 0.680 |

***Table 2.*** *Calculated and experimental values (degrees) of bond angles for amino acid residues of the Ala-Tyr dipeptide*

| Bond angles | Extended structure | Folded structure | [11, 12] |
|---|---|---|---|
| H2-N1-H11 | 107.89 | 107.97 | 108.15 |
| H2-N1-H12 | 110.01 | 107.78 | 110.65 |
| H11-N1-H12 | 107.47 | 110.37 | 108.20 |
| H2-N1-C3 | 112.91 | 112.05 | 111.33 |
| H11-N1-C3 | 112.20 | 113.00 | 109.40 |
| H12-N1-C3 | 106.22 | 105.56 | 109.05 |
| N1-C3-H4 | 107.55 | 106.08 | 106.94 |
| N1-C3-C5 | 104.62 | 104.45 | 110.05 |
| N1-C3-C7 | 110.07 | 111.11 | 109.74 |
| H4-C3-C5 | 111.58 | 107.24 | 108.55 |
| H4-C3-C7 | 111.00 | 110.36 | 110.40 |
| C3-C5-O6 | 118.22 | 118.18 | 118.39 |
| C3-C5-N13 | 115.72 | 116.95 | - |
| C3-C7-H8 | 111.06 | 110.19 | 110.57 |
| C3-C7-H9 | 109.47 | 111.52 | 110.33 |
| C3-C7-H10 | 110.66 | 110.33 | 110.37 |
| C5-C3-C7 | 111.75 | 116.92 | 111.07 |
| H8-C7-H9 | 108.38 | 109.08 | 108.90 |
| H8-C7-H10 | 109.31 | 107.04 | 108.36 |
| H9-C7-H10 | 107.87 | 108.55 | 108.25 |
| C5-N13-H14 | 119.88 | 122.29 | - |
| C5-N13-C15 | 125.50 | 124.76 | - |
| O6-C5-N13 | 126.05 | 124.83 | - |
| N13-C15-H16 | 108.30 | 108.33 | - |
| N13-C15-C17 | 108.29 | 107.86 | 109.6 |
| N13-C15-C19 | 112.10 | 112.79 | 111.0 |
| H14-N13-C15 | 112.37 | 112.23 | - |
| C15-C17-O18 | 116.34 | 116.68 | 116.5 |
| C15-C17-O34 | 115.94 | 115.70 | 117.0 |
| O18-C17-O34 | 127.68 | 127.62 | 126.5 |
| C15-C19-H20 | 108.00 | 106.34 | - |
| C15-C19-H21 | 106.44 | 107.61 | - |
| C15-C19-C22 | 115.28 | 115.49 | 114.4 |
| H16-C15-C19 | 109.63 | 107.27 | - |
| H16-C15-C17 | 109.50 | 107.94 | - |
| C19-C22-C23 | 121.41 | 121.20 | 121.4 |
| C19-C22-C25 | 120.92 | 121.26 | 120.4 |
| C19-C15-C17 | 108.99 | 112.48 | 111.3 |
| H20-C19-H21 | 107.16 | 107.24 | - |
| H20-C19-C22 | 109.77 | 110.07 | - |
| H21-C19-C22 | 109.85 | 109.74 | - |
| C22-C23-H24 | 119.49 | 119.62 | - |
| C22-C23-C27 | 121.57 | 121.66 | 121.2 |
| C22-C25-H26 | 119.59 | 119.35 | - |

| | | | |
|---|---|---|---|
| C22-C25-C29 | 121.59 | 121.62 | 121.2 |
| C23-C27-H28 | 120.90 | 120.18 | - |
| C23-C27-C31 | 119.67 | 119.61 | 119.4 |
| H24-C23-C27 | 118.94 | 118.72 | - |
| C25-C29-H30 | 120.16 | 120.89 | - |
| C25-C29-C31 | 119.63 | 119.71 | 119.8 |
| C25-C22-C23 | 117.67 | 117.54 | 118.2 |
| H26-C25-C29 | 118.82 | 119.03 | - |
| C27-C31-C29 | 119.87 | 119.86 | 120.3 |
| C27-C31-O32 | 117.51 | 122.67 | 122.2 |
| H28-C27-C31 | 119.43 | 120.21 | - |
| C29-C31-O32 | 122.62 | 117.47 | 117.6 |
| H30-C29-C31 | 120.21 | 119.40 | - |
| C31-O32-H33 | 110.22 | 110.20 | - |

***Table 3.*** *Calculated values of dihedral angles of the Ala-Tyr dipeptide (in degrees)*

| Dihedral angles | Extended structure | Folded structure |
|---|---|---|
| H11-N1-C3-C5 (φ - Ala) | -87.44 | -139.80 |
| N1-C3-C7-H8 (χ1 - Ala) | 58.51 | -55.86 |
| N1-C3-C5-N13 (ψ - Ala) | 155.54 | -167.87 |
| C3-C5-N13-C15 (ω - Tyr) | 169.16 | 178.87 |
| C5-N13-C15-C17 (φ - Tyr) | -135.34 | -157.80 |
| N13-C15-C19-C22 (χ1 - Tyr) | -64.62 | 60.48 |
| C15-C19-C22-C23 (χ2 - Tyr) | 96.17 | -92.35 |
| C15-C19-C22-C25 (χ3 - Tyr) | -83.80 | 87.78 |
| N13-C15-C17-O34 (ψ - Tyr) | 162.06 | 171.10 |

The values for the interatomic distances of the oppositely charged groups of the molecule (reflecting the distances between the atoms of the functional group) were calculated. The interatomic distances between the functional groups for the extended and folded structures were determined as 5.96 and 5.98 Å for N1-O18, 7.03 and 7.10 Å for N1-O34, 6.63 and 6.23 Å for H2-O18, 7.81 and 7.35 Å for H2-O34, 6.35 and 6.76 Å for H11-O18, 7.46 and 7.98 Å for H11-O34, 6.10 and 6.10 Å for H12-O18, 6.85 and 6.90 Å for H12-O34, respectively. These values indicate that both structures have favorable interactions.

One of the factors that affects the geometry of the molecule are the hydrogen bonds. Therefore, the intramolecular hydrogen bonds were studied for the Ala-Tyr dipeptide by DFT calculations. Possible intramolecular hydrogen bonds for the optimized conformations were revealed. The geometric parameters of the identified intramolecular hydrogen bonds were calculated to evaluate the stability of the Ala-Tyr conformers in water environment (Table 4). It was established that in the optimized structures of the dipeptide, the following hydrogen bonds were formed: between the hydrogen atom of the $\alpha$-amino group and the oxygen atom of the carbonyl group of the alanine backbone; hydrogen bonds between the hydrogen atom of the amide group of the tyrosine backbone and the neighboring oxygen atom of the C-terminal carboxyl group. Weak hydrogen bonds are formed between the hydrogen atoms of the methyl qroup of the Ala residue side chain and the oxygen atoms of the backbone carbonyl group and the the C-terminal carboxyl group in both the extended (H8 …O6 (3.11 Å), H9 …O6 (3.71 Å), H9…O18 (3.79 Å)) and folded structure (H9 …O6 (3.74 Å), H10…O18 (3.72 Å)).

***Table 4.*** *Parameters of strong hydrogen bonds in the optimized structures of the Ala-Tyr dipeptide*

| DH…A | DH (Å) | | H…A (Å) | | D…A (Å) | | ∠DHA (degrees) | |
|---|---|---|---|---|---|---|---|---|
| | Extended structure | Folded structure | Extended structure | Folded structure | Extended structure | Folded structure | Extended structure | Folded structure |
| N1H12 … O6 (I) | 1.04 | 1.03973 | 2.00 | 1.90 | 2.60 | 2.56158 | 114.00 | 118.38 |
| N13H14 … O18 III) | 1.02 | 1.01872 | 2.14 | 2.04 | 2.63 | 2.59694 | 107.69 | 111.78 |

Due to resonance interactions, all atoms in the peptide bond should be located in the amide plane. However, due to the formation of hydrogen bonds between the $\alpha$-amino group of the molecule and the hydrogens of the amide group and the oxygen atom of the C-terminal carboxyl group, the planarity of the amide plane structure is not disturbed for both conformations. To explain the planarity, the dihedral angles and geometric parameters of the molecule were analysed. It was found that the calculated value of the C3-C5-N13-C15 rotation angle is 169.160 for the extended structure, and 178.870 for the folded structure, respectively. Due to stereochemical factors, planarity in the peptide bond is possible only when the dihedral angle $\omega$ is close to 180° (trans) since this angle ensures that the atoms of the amide group are located in the same plane.

Since the calculation of atomic charges is an important aspect of quantum mechanical calculations, the Milliken atomic charges of the Ala-Tyr dipeptide [13] are also calculated in this work (Table 5). According to these results, in both the extended and folded structures, the N1 atom of the $\alpha$-amine group of the molecule, the O6 atom of the carbonyl group, the C7 atom of the methyl group of the side chain of the Ala residue, the C15 atom of the main chain of the Tyr residue, the C19 of the side chain of the Tyr residue and the C23, C25 and O32 atoms of the phenol ring, and the O18 and O34 atoms of the carboxyl group of the molecule carry a large negative charge. As a result of dipeptide folding, N1 (0.017458 e), H2 (0.003758 e), H4 (0.017416 e), C5 (0.040790 e), O6 (0.022502 e), C7 (0.025101 e), H8 (0.003190 e), N13 (0.070043 e), O18 (0.025461 e), C19 (0.353327 e), H20 (0.011422 e), C23 (0.072390 e), H24 (0.004646 e), C25 (0.293917 e), H26 (0.000639 e), C27 (0.046784 e), C29 (0.014925 e), H30 (0.003329 e), H33 (0.000471 e), O34 (0.014397 e) atoms' charges have increased, while the charges of C3 (0.118247 e), H9 (0.003619 e), H10 (0.004692 e), H11 (0.006066 e), H12 (0.001811 e), H14 (0.015084 e), C15 (0.047648 e), H16 (0.005286 e), C17 (0.042414 e), H21 (0.008776 e), C22 (0.729206 e), H28 (0.004338 e), C31 (0.009744 e) atoms have decreased. The largest charge shift in terms of value occurred at the C22 atom of the phenol ring of the Tyr residue. Since the identified moieties can act as both donors and acceptors when interacting with receptor residues, these data provide insights into charge transfer processes.

***Table 5.*** *Milliken atomic charges (e) for optimized structures of the Ala-Tyr dipeptide*

| Atoms | Extended structure | Folded structure |
|---|---|---|
| N1 | -0.559525 | -0.542067 |
| H2 | 0.406978 | 0.410736 |
| C3 | 0.249169 | 0.130922 |
| H4 | 0.213496 | 0.230912 |
| C5 | 0.015014 | 0.055804 |
| O6 | -0.534900 | -0.557402 |
| C7 | -0.569213 | -0.544112 |
| H8 | 0.185948 | 0.189138 |
| H9 | 0.193558 | 0.189939 |
| H10 | 0.186923 | 0.182231 |
| H11 | 0.416794 | 0.410728 |

| | | |
|---|---|---|
| H12 | 0.413417 | 0.411606 |
| N13 | -0.176211 | -0.106168 |
| H14 | 0.351833 | 0.336749 |
| C15 | -0.361248 | -0.408896 |
| H16 | 0.167002 | 0.161716 |
| C17 | 0.448305 | 0.405891 |
| O18 | -0.667206 | -0.641745 |
| C19 | -0.428830 | -0.075503 |
| H20 | 0.152796 | 0.164218 |
| H21 | 0.168487 | 0.159711 |
| C22 | 0.874414 | 0.145208 |
| C23 | -0.390493 | -0.318103 |
| H24 | 0.127506 | 0.132152 |
| C25 | -0.648227 | -0.354310 |
| H26 | 0.137664 | 0.138303 |
| C27 | 0.124641 | 0.171425 |
| H28 | 0.142648 | 0.138310 |
| C29 | 0.227369 | 0.242294 |
| H30 | 0.139932 | 0.143261 |
| C31 | -0.178726 | -0.188470 |
| O32 | -0.568238 | -0.568269 |
| H33 | 0.383940 | 0.384411 |
| O34 | -0.645018 | -0.630621 |

The charge distributions are visualized by molecular electrostatic potential (MEP) maps [14, 15]. The positive, negative and neutral electrostatic potential parts for the optimized structures of the molecule are shown in Figure 2. As can be seen from the MEP, the negative potential parts (the lowest values for the extended and folded structures are -0.165e. and -0.170e, respectively) are the most nucleophilic moieties localized on the oxygen atoms of the C-terminal carboxyl group of the molecule, while the positive potential parts (the highest values for the extended and folded structures are 0.165e. and 0.170e, respectively) are the most electrophilic moieties localized on the hydrogen atoms of the $\alpha$-amino group of the molecule and the atoms of the methyl group of the alanine side chain. As a result, the O atoms of the COO- group exhibit a strong repulsion, while the H atoms of the $NH_3^+$ group and the methyl group of Ala exhibit a strong attraction, and these sites are of great importance in the biological activity of the molecule.

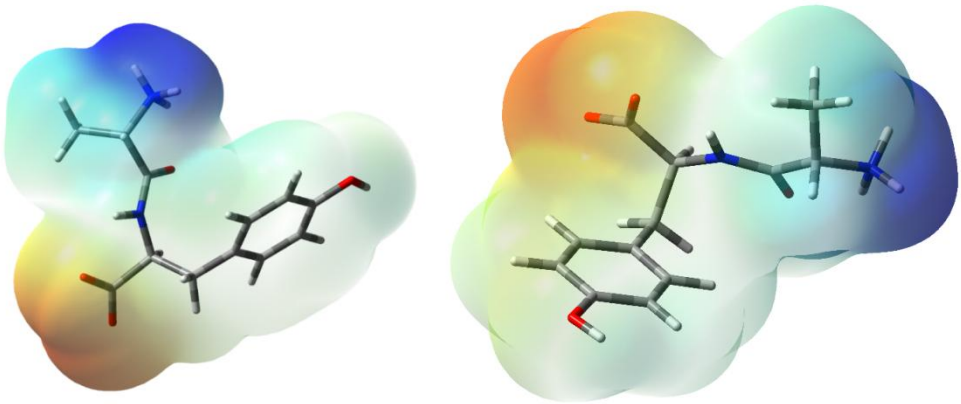

*(a)* *(b)*

***Fig 2.*** *Molecular electrostatic potential for the optimized extended (a) and folded (b) structures of the Ala-Tyr dipeptide*

The electronic parameters of the Ala-Tyr molecule obtained from DFT calculations are given in Table 6.

***Table 6.*** *Electronic parameters and molecular properties of the Ala-Tyr dipeptide*

| Physical quantities | Extended structure | Folded structure |
|---|---|---|
| Electronic energy (eV) | -23876.079 | -23876.082 |
| EHOMO (eV) | -6.156 | -6.219 |
| ELUMO (eV) | -0.573 | -0.662 |
| Energy gap ΔE (eV) | 5.583 | 5.557 |
| Electron affinity A=[-ELUMO] (eV) | 0.573 | 0.662 |
| Ionization potential I=[-EHOMO] (eV) | 6.156 | 6.219 |
| Global hardness η=(I-A)/2 (eV) | 2.792 | 2.779 |
| Softness S=1/2η (1/eV) | 0.179 | 0.180 |
| Electronegativity χ=(I+A)/2 | 3.365 | 3.441 |
| Chemical potential μ= -(I+A)/2 | −3.365 | −3.441 |
| Electrophilicity index ω=μ 2 /2η | 2.03 | 2.13 |
| Dipole moment (Debye) | 28.242 | 25.217 |

The values of HOMO and LUMO energies are used to obtain information about the chemical reactivity and kinetic stability of the molecule, and these indicators are considered important parameters in quantum-chemical calculations [19-19]. As can be seen from Figure 3, in the folded structure, the HOMO orbitals are localized over the entire molecule except for the $\alpha$-amino group of the molecule and the side chain of the Ala residue, and the LUMO orbitals are localized over the entire molecule except for the atoms of the carboxyl group of the molecule and the O and H atoms in the phenol ring of the Tyr residue (red color characterizes the negative charge for the molecule, and green color characterizes the positive charge for the molecule). In the extended structure, the HOMO orbitals are localized over the entire molecule except for the $\alpha$-amino group of the molecule and the side chain of the Ala residue, and the LUMO orbitals are localized over the N atom of the amide group and the side chain of the Tyr residue. Therefore, while the HOMO-LUMO transition is observed in the folded structure at the $\alpha$-amino group of the molecule, the side chain of the Ala residue, the carboxyl group atoms, and the O and H atoms of the hydroxyl group of the Tyr residue side chain (this type of transition decreases the polarization of the molecule and causes an decrease in the dipole moment during electronic excitation), in the extended structure it is observed on the $C^{\alpha}$ of the main chain of the Tyr residue, the atoms of the carbonyl and carboxyl groups of the dipeptide. Thus, the HOMO-LUMO transition is characterized as an electron transition directed from a broadly delocalized donor site to a more specific, local acceptor center in the extended structure.

Table 6 shows the values of other chemical reactivity descriptors such as ionization potential, electron affinity, chemical hardness and softness, electronegativity, chemical potential, and electrophilic index for the molecule. Looking at the energy gap value, we see that both structures are insulating and rigid molecules (stable), but the folded structure is more reactive than the extended structure. The higher ionization potential and electron affinity in the folded structure is explained by the fact that this structure is somewhat less able to donate electrons than the extended structure, and its tendency to accept electrons (acceptor property) is stronger. The extended structure is more likely to be a donor. The electrophilicity index (ω) is larger in the folded structure, meaning that the molecule behaves as a stronger electrophile in this conformation. In the folded structure of the dipeptide, the electronegativity has increased and the chemical potential has decreased, which means that the tendency of the molecule to attract electron density has increased. The calculated values of the dipole moment, which characterizes

the nonlinear optical properties, show that the dipole moment has decreased by 3.025 Debye as a result of the folding of the dipeptide.

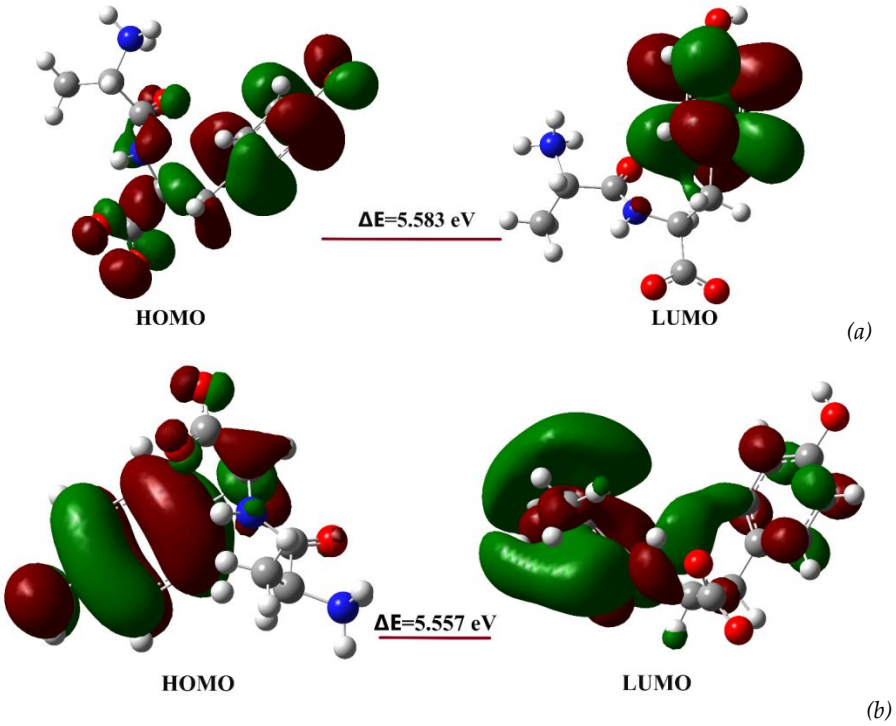


***Fig 3.*** *HOMO and LUMO molecular orbitals for the optimized extended (a) and folded (b) structures of the Ala-Tyr dipeptide*

## 4. CONCLUSION

In the research work, the geometric and electronic properties of the extended and folded conformations of the Ala–Tyr dipeptide were studied using DFT/B3LYP/6-31+G(d,p) calculations. The results showed that this molecule is stabilized by both non-valent and electrostatic interactions, as well as intramolecular hydrogen bonds. During peptide chain folding, a redistribution of electron density is observed within the molecule. Analysis of the HOMO and LUMO orbitals revealed that the mechanisms of electron transition between the extended and folded structures are different in nature, and it was established that the dipole moment of the molecule decreases upon charge shifts by the folding of peptide chain. A significant decrease in the dipole moment upon folding indicates that the interaction of the Ala–Tyr dipeptide with the environment is strictly conformation-dependent. Overall, the obtained results provide a deeper understanding of the structure-activity relationship of the Ala-Tyr dipeptide, as well as an explanation of its biological activity and behavior as an ACE inhibitor at the atomic and electronic levels. These results can be used as a theoretical basis for the future development of similar bioactive peptides and functional food additives.

**REFERENCE LIST**

1. Ozawa, H., Miyazawa, T., Burdeos, G.C., Miyazawa, T. Biological Functions of Antioxidant Dipeptides. J Nutr Sci Vitaminol (Tokyo). 2022;68(3):162-171. Doi: 10.3177/jnsv.68.162.
2. Zheng, L., Zhao, Y., Dong, H., Su, G., & Zhao, M. Structure–activity relationship of antioxidant dipeptides: Dominant role of Tyr, Trp, Cys and Met residues. Journal of Functional Foods, 2016, 21, 485–496. doi:10.1016/j.jff.2015.12.003

3. Saito, Y.; Wanezaki, K.; Kawato, A.; Imayasu, S. Antihypertensive effects of peptide in sake and its by-products on spontaneously hypertensive rats. Biosci Biotechnol Biochem. 1994, 58(5), 812-816. doi: 10.1271/bbb.58.812.
4. Nii, Y; Fukuta, K; Yoshimoto, R.; Sakai, K.; Ogawa, T. Determination of antihypertensive peptides from an izumi shrimp hydrolysate. Biosci Biotechnol Biochem. 2008, 72(3), 861-864. doi: 10.1271/bbb.70565.
5. Druml, W., Lochs, H., Roth, E., Hubl, W., Balcke, P., & Lenz, K. (1991). Utilization of tyrosine dipeptides and acetyltyrosine in normal and uremic humans. *American Journal of Physiology*, 260(2), E280–E285. https://doi.org/10.1152/ajpendo.1991.260.2.E280
6. Ramachandran, K. I., Deepa, G., & Namboori, K. (2008). Computational chemistry and molecular modeling: Principles and applications. Springer-Verlag. https://doi.org/10.1007/978-3-540-77304-7
7. Sara Gambar Rahimzade and Gulnara Ahmad Akverdieva. (2024). PM3 quantum chemical calculations of the bioactive Ala-Tyr dipeptide. Advanced Physical Research, Vol.6, No2, pp. 123-131, https://doi.org/10.62476/apr62123
8. Kohn W.; Becke, R.G. Parr, Density functional theory of electronic structure, J.Phys. Chem. 1996, 100, 12974–12980
9. M. J. Frisch, G. W. Trucks, H. B. Schlegel, G. E. Scuseria, M. A. Robb, J. R. Cheeseman, G. Scalmani, V. Barone, G. A. Petersson, H. Nakatsuji, X. Li, M. Caricato, A. V. Marenich, J. Bloino, B. G. Janesko, R. Gomperts, B. Mennucci, H. P. Hratchian, J. V. Ortiz, A. F. Izmaylov, J. L. Sonnenberg, D. Williams-Young, F. Ding, F. Lipparini, F. Egidi, J. Goings, B. Peng, A. Petrone, T. Henderson, D. Ranasinghe, V. G. Zakrzewski, J. Gao, N. Rega, G. Zheng, W. Liang, M. Hada, M. Ehara, K. Toyota, R. Fukuda, J. Hasegawa, M. Ishida, T. Nakajima, Y. Honda, O. Kitao, H. Nakai, T. Vreven, K. Throssell, J. A. Montgomery, Jr., J. E. Peralta, F. Ogliaro, M. J. Bearpark, J. J. Heyd, E. N. Brothers, K. N. Kudin, V. N. Staroverov, T. A. Keith, R. Kobayashi, J. Normand, K. Raghavachari, A. P. Rendell, J. C. Burant, S. S. Iyengar, J. Tomasi, M. Cossi, J. M. Millam, M. Klene, C. Adamo, R. Cammi, J. W. Ochterski, R. L. Martin, K. Morokuma, O. Farkas, J. B. Foresman, and D. J. Fox, Gaussian 16, Revision C.01, Gaussian, Inc., Wallingford CT, 2016. https://gaussian.com/citation/
10. Dennington R, Keith TA, Millam JM. GaussView, Version 6.0. Shawnee Mission, KS: Semichem Inc; 2016.
11. Lehmann, M. S., Koetzle, T. F., & Hamilton, W. C. (1972). *Precision neutron diffraction structure determination of protein and nucleic acid components. I. The crystal and molecular structure of the amino acid L-alanine*. Journal of the American Chemical Society, 94(8), 2657–2660. https://doi.org/10.1021/ja00763a016
12. Mostad, A., Nissen, H. M., & Rømming, C. (1972). *Crystal structure of L-tyrosine*. Acta Chemica Scandinavica, 26, 3819–3833.
13. Arunagiri, C., Arivazhagan, M., Subashini, A., & Maruthaiveeran, N. (2014). Theoretical and experimental calculations, Mulliken charges and thermodynamic properties of 4-chloro-2-nitroanisole. Spectrochimica Acta Part A: Molecular and Biomolecular Spectroscopy, 131, 647–656. doi:10.1016/j.saa.2014.03.116
14. Hernández B, Luque FJ, Orozco M. Molecular recognition and interaction energies studied by computational methods. J Comput Aided Mol Des. 2000;14(4):329-339. doi:10.1023/A:1008111820916
15. Politzer P, Murray JS. The fundamental nature and role of the electrostatic potential in atoms and molecules. Theor Chem Acc. 2002;108(3):134-142. doi:10.1007/s00214-002-0363-9
16. Demir S, Tinmaz F, Dege N, Ilhan IO. Vibrational spectroscopic studies, NMR, HOMO–LUMO, NLO and NBO analysis of 1-(2-nitrobenzoyl)-3,5-diphenyl-4,5-dihydro-1H-pyrazole using X-ray diffraction and DFT calculations. J Mol Struct. 2016; 1108:637-648. doi: 10.1016/j.molstruc.2015.12.057
17. Jordaan MA, Ebenezer O, Mthiyane K, Damoyi N, Shapi M. Amide–imidic prototropic tautomerization of efavirenz: NBO analysis, hyperpolarizability, polarizability and HOMO–LUMO calculations using density functional theory. Comput Theor Chem. 2021; 1201:113273.
18. Ramachandran KI, Deepa G, Namboori K. Computational Chemistry and Molecular Modeling: Principles and Applications. Berlin, Heidelberg: Springer-Verlag; 2008. doi:10.1007/978-3-540-77304-7
19. Chandrasekaran K, Thilak Kumar R. Structural, spectral, thermodynamical, NLO, HOMO, LUMO and NBO analysis of fluconazole. Spectrochim Acta A Mol Biomol Spectrosc. 2015; 150:974-991. doi: 10.1016/j.saa.2015.06.018

JOURNAL OF BAKU ENGINEERING UNIVERSITY - PHYSICS
*2025. Volume 9, Number 2* *Pages 92-100*

*UDC: 678.742.2:620.3:537.226*
*DOI: https://doi.org/10.30546/09081.2025.002.1026*

# EFFECT Of ELECTROTHERMOPOLARIZATION ON THE ELECTROPHYSICAL PROPERTIES AND STRUCTURE Of HDPE/$HfO_2$ – BASED POLYMER NANOCOMPOSITES

**Aybeniz Sabir HUSEYNOVA**

*Ministry of Science and Education of the Republic of Azerbaijan,Institute of Physics, 131 H. Javid Ave., AZ -1073, Baku, Azerbaijan*

*ARTICLE INFO*

*Article history:*
*Received:2025-05-29*
*Received in revised form:2025-06-11*
*Accepted:2025-06-30*
*Available online:2025-12-21*

*Keywords:*
*Nanocomposites; Polyethylene; Hafnium oxide; Nanoparticles; Spectrometer; Electrothermopolarization*


*ABSTRACT*

*This study investigates the effect of electrothermopolarization (ETP) on the structural and electrophysical properties of polymer nanocomposites based on HDPE and hafnium oxide ($HfO_2$) nanoparticles. We analyze the interactions between the polymer matrix and the nanoparticles, detailing structural changes within the bulk and the interphase zones both before and after the ETP process. Scanning Electron Microscopy (SEM) reveals a diverse morphology, ranging from spherical to irregular shapes, highlighting the distribution of $HfO_2$ within the matrix. Furthermore, the impact of $HfO_2$ on the polymer's crystalline and amorphous phases was characterized using X-ray diffraction (XRD) and Differential Scanning Calorimetry (DSC). These results demonstrate that the filler significantly influences the supramolecular structure and thermal behavior of the HDPE, which in turn governs the stability of the electret state.*

**Corresponding author. Email address: aem05@rambler.ru*

## 1. INTRODUCTION

As it is known, the inclusion of nanoparticles in a small amount of polymer allows its physical properties to be improved, its life to be extended. The properties of modified polymer nanocomposites are related to the compatibility and distribution of their components. Meanwhile small amount of nanoparticles acts as a crystallization center. As the amount of nanoparticles increases they accumulate in the amorphous part of the polymer, which leads to changing amorphous and crystalline states in the polymer to create a separate structure in the polymer environment [1, 2].

It should be noted that depending on the nature, size and distribution of nanoparticles, the resulting polymer nanocomposite can be electroconductive, antistatic or dielectric. In this connection the study of the nanocomposite properties obtained by adding metal oxide nanoparticles to polyethylene is of particular interest [3, 4]. The change in the physical properties of polyethylene materials by nanoparticles is mainly due to two reasons: nanoparticles act as a source of structuring and the nanocomposite interphase layer has a large number of charge traps with different activation energy. This work deals with the polymers asa high-density polyethylene (HDPE) matrix and ($HfO_2$) hafnium oxide nanoparticles, having improved physical

parameters, such as high chemical and thermal stability, large band gap, high permittivity as well. We suppose that these distinctive properties of $HfO_2$content should be reflected in the properties of HDPE+$HfO_2$modified polymer nanocomposites. Metal oxide nanoparticles play a very important role in many areas of physics and material science [5, 6].

In terms of PE electrical properties as a non-polar polymer is a high-quality, high-frequency dielectric; permittivity and dielectric loss tangent vary only slightly under the changes in the electric field frequency, temperature within minus 80°C up to 100°C and humidity. However, catalyst residues in HDPE increase the dielectric loss tangent, especially with the temperature change, which leads to some deterioration of insulating properties. Therefore to improve both the structural, electrostatic and physical properties of polyethylene, we use hafnium metal nanooxide as an addition.

In modern literature, despite the large number of published works on materials based on hafnium nanooxide, HDPE/$HfO_2$ – based nanocomposites have not been practically studied. $HfO_2$ hafnium dioxide properties determine its use in many fields of science and technology. Thus in microelectronics, due to its wide band gap, high permittivity, and low leakage currents, $HfO_2$ is considered to be alternative dielectric to replace the traditionally used silicon dioxide $SiO_2$. $HfO_2$ is also used as a surface coating for optical fibers and dielectric mirrors of ultraviolet lasers.

Our research is dedicated to the change in HDPE/$HfO_2$ nanocomposite structure, dielectric, electret and thermal properties under the influence of ETP process as a result of polarization processes occurring at the interface. Modified polymer nanocomposite dielectric properties are closely related to the behavior at the interface between nanoparticles and polymer matrix [7, 8]. Many polymer nanocomposites based on metal oxide nanoparticles have a high permittivity and thus a huge potential for using in modern microelectronics to develop new capacitors for energy storage, gates in MOSFETs, memory cells, supercapacitors and etc. [9].

As it is known polymers and nanocomposite materials obtained on their basis after exposure to external constant electric field at sufficiently high temperatures are polarized and have electret properties. The main characteristics of the electret material are the magnitude of electric charge and its stability. To meet the need for electrets with these characteristics more sophisticated and comprehensive study of their thermal properties is required [10-12]. Recently the acquisition and study of new nanocomposite materials by introducing nanoparticles into both low-density and high-density polyethylene yield better results (DSC, SEM) that are of particular importance from practical and scientific standpoint.

## 1. EXPERIMENTAL PART:

### *1.1. Materials*

HDPE polyethylene granules (SOCAR, "Azerikimya" Production Union "Etilen-Polyethylene" plant, 15803-020), $CCl_4$ organic solvent (Code 141245, 99.5%, CAS Common Chemistry-P.L.C); hafnium oxide ($HfO_2$) nanoparticles, size 10-20nm, Luoyang Tongrun Info Technology Co., Ltd. China, CAS 12055-23-1, 99%).

### *1.2. Synthesis of polymer nanocomposites*

HDPE/$HfO_2$ polymer nanocomposites have been obtained as follows: polyethylene granules are dissolved in 60 ml of organic solvent as carbon tetrachloride ($CCl_4$)at T=70°C. $HfO_2$ nanoparticles are added to the polymer solution of various content and mixed for 8 hours until the

homogeneous mixture is prepared. The mixture is transferred to Petri dish and dried in the vacuum oven for 24 hours. Then nanocomposite thin films are produced from these samples by hot pressing at polyethylene melting temperature and pressure 15MPa for 10 min. After hot pressing the films are cooled in water. Cooling rate of nanocomposite films is 20deg/min. Film thicknesses is 90–105 μm (Fig 1).

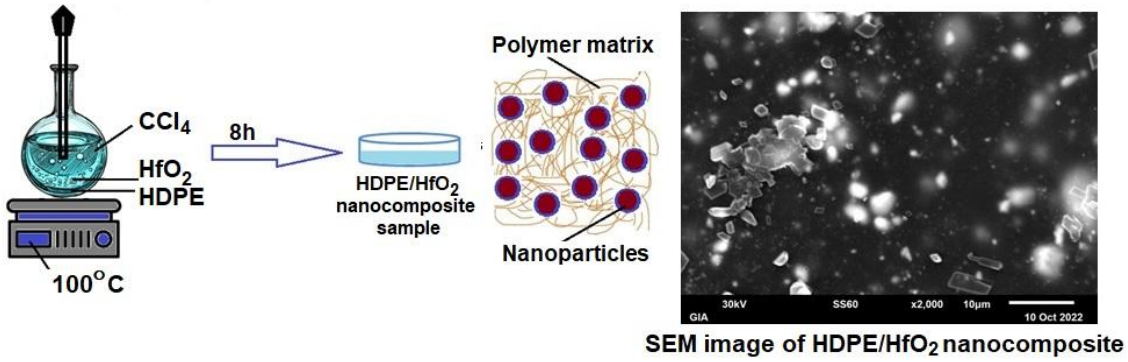


***Fig.1*** *Synthesis scheme of HDPE/$HfO_2$ nanocomposites*

### *1.3. Nanocomposite Characterization*

X-ray diffraction studies of nanocomposites have been performed on D2 Phase X-ray diffractometer in reflection mode (Bragg-Brentano geometry) using Cu-k$\alpha$ radiation (average wavelength $\lambda$=1.5406Å, nickel $\beta$-filter). Diffraction pattern registration is carried out in continuous mode in the range of angles $2\theta$ = 5–80°.

SEM analysis of nanocomposites is made on scanning electron microscope JEOL JSM 6610-LV at accelerating voltage 30 kV.

Polymer nanocomposites undergo electrothermopolarizaton (ETP) by using external electric field strength $7 \cdot 10^6 \div 12 \cdot 10^6$V/m at T=100°C and then cooling down to room temperature for 1 hour. Electret characteristics have been measured on EFPM-1 device.

Differential scanning calorimeter (DSC) data are obtained on heat flux calorimeter NETZSCH DSC 204 F1 Phoenix by analyzing melting and crystallization thermograms. The investigations are carried out with heating rate 10 deg/min at T=20÷180°C. Experimentally obtained DSC curves represent the dependence of heat flux (mJ/s) on temperature. Heating in nitrogen atmosphere at the predetermined rate according to the controlled program is taken place and the heat flows of the reference and the material under consideration are compared during the measurement process.

## 3. RESULTS AND DISCUSSION

The following mechanisms can be used to improve the electret properties of nanocomposites: 1. Change in supramolecular structure due to the addition of $HfO_2$ nanoparticles to HDPE, as well as the appearance of various local centers of polarized and specific charges; 2. Oxidation of free radicals and polymer chains in nanocomposites obtained by the method of hot pressing at high temperature (close to melting temperature of matrix). Oxidative-destructive processes may at times break the non-polarity of polymer matrix. When oxygen-binding groups are formed in the

polymer chain along the macromolecule, polar regions arise, which in turn leads to the formation of dipole-orientational polarization to improve nanocomposite electret properties. This mechanism is connected with the migration polarization of HDPE/%wt. $HfO_2$ heterogeneous system. It determines the existence of electrets over a period of months and even years.

While investigating electret properties of polymer nanocomposites [13-15,21-23] one can conclude that there is a very broad relationship between the physical and chemical structure of polymers and the size of collected charges. It is shown that the change of polymer electret properties is primarily influenced by trap structures. Therefore the stability and amount of charges captured by the traps are largely defined by the polymer supramolecular structure peculiarities.

The crystal structure, size and orientation of $HfO_2$nanoparticles and HDPE (Fig. 2.a) are investigated by X-ray diffraction (XRD) method. X-ray diffraction pattern shows that the nanoparticles have a polycrystalline monoclinic phase. The observed data are in good agreement with the standard JCPDS card no: 06-0318. In Fig. 2.b there have been shown X-ray diffraction spectra of HDPE and PE/$HfO_2$ - based polymer nanocomposites. Analysis of X-ray diffraction spectra reveals (Fig. 2.b) that the partial narrowing of diffraction peak half-width due to hafnium oxide ($HfO_2$) may be associated with the increase ofbond intensity in final nanocomposites [16-20,24].

The nanocomposite matrix demonstrates that X-ray diffraction peak intensity increases as $HfO_2$ nanoparticles are incorporated into HDPE matrix.

X-ray spectrum of HDPE/$HfO_2$ nanocomposite shows that as the concentration of $HfO_2$ increases, peaks are observed in X – ray spectrum at an angle of 2θfor HDPE:21,59° (110), 23,98° (200); HDPE/3%$HfO_2$:28°(111),31,89° (111), 34,93° (020), 36° (200), 41,06°(102), 49,97°(022),50,82° (220), 54,69° (300), 56° (221); HDPE/5%$HfO_2$:28,6° (111), 31,5° (111), 34,48° (020), 35,5° (200), 41° (102), 49,6° (022); 50,5° (220), 54° (300), 55,89° (211), 60° (131), 63,3°(113) 66°(331); HDPE/7%$HfO_2$:24°(011), 28,63° (111), 31,7° (111), 34,5° (020), 35,6°(200)38,9° (021), 41,2° (102), 49,7°(022), 50,7° (220), 54,6° (300), 56° (221), 60,5°(131), 63°(113), 66°(331)respectively, that assumes the typical structure of orthorhombic $HfO_2$. Sharp and very intense X-ray peaks indicate that the materials under investigation are the nanocomposites characterized by HDPE semicrystalline structure.

The average particle size of resulting HDPE/$HfO_2$ nanocomposites is calculated using Debye-Scherrer equation. Debye-Scherrer equation is the most simple way to determine particle size:

$$D = \frac{K\lambda}{\beta \cos\theta} (3)$$

where D is the particle size, $\lambda$ = 1.5406 Å, β is the peak width at half maximum, θ is the diffraction angle (in radians), K is the constant approximately equal to 0.9. With increasing filler content, the diffraction intensity of HDPE/$HfO_2$ phases decreases.

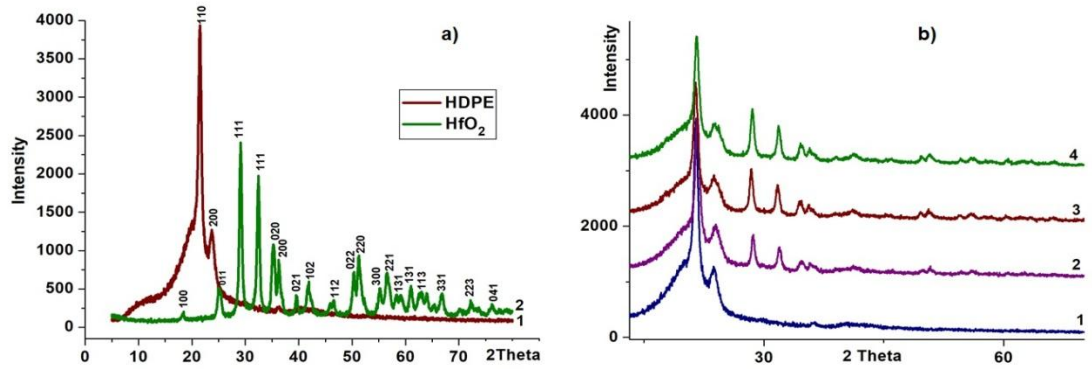


***Fig. 2*** *XRD patterns of $HfO_2$ nanoparticle in powder form, HDPE (a) and XRD patterns of nanocomposites HDPE/%wt. $HfO_2$ (b): 1. HDPE; 2. HDPE/3%$HfO_2$; 3. HDPE/5%$HfO_2$; 4. HDPE/7%$HfO_2$*

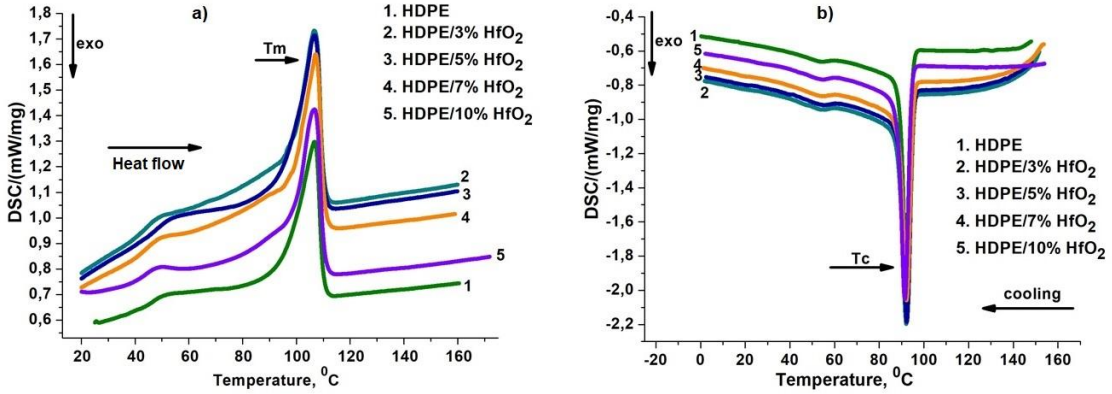


***Fig.3*** *DSC curves heat flow (a) and cooling (b) of pure HDPE, HDPE/$HfO_2$ nanocomposites*

$HfO_2$ metal oxide-containing nanoparticle used in this work is located in the interphase layer of HDPE structural elements and causes the formation of heterogeneous centers of crystal formation in the nanocomposite alloy that leads to the growth of the crystallization center during the nanocomposite cooling process [25-34]. To determine the thermal stability of HDPE/$HfO_2$-based polymer nanocomposites, the tests are carried out using the differential scanning calorimetry (DSC) method. In Fig.4 and Fig.5 there has been shown the thermal stability of nanocomposite materials of polyethylene and HDPE/$HfO_2$ nanocomposites depending on $HfO_2$ particle concentration. These maxima can break old bonds and form new ones, as well as can change the molecular mass in HDPE/$HfO_2$ nanocomposites. This means that the interaction of polymer matrices with the nanoparticle charged surface leads to the formation of polymer nanoparticle nearby the nanoparticle surface and it is this interfacial nanoparticle that determines the maxima.

Having determined the fusion heat it is possible to calculate the degree of crystallinity of the nanocomposite under study (Table 1). Since the cooling process in the calorimeter is slow, the amount of crystalline phase formed in this case is significantly less than in the process of starting material production [35-37]. It should be noted that there is a slight decrease in the melting temperature of the polymer nanocomposite, which can be explained by partial decrease in the chain length and a greater mobility of the polymer molecules, respectively.

***Table 1.*** *Results of DSC analysis of heat flow and cooling*

| Sample | Tm, °C | Tc, °C | Melting enthalpy, ΔH, J/g | Degree of nanocomposite crystallinity, % |
|---|---|---|---|---|
| HDPE | 107,8 | 92 | 39,47 | 31,57 |
| 97%HDPE/3%$HfO_2$ | 106,3 | 92,1 | 50,24 | 36,38 |
| 95%HDPE/5%$HfO_2$ | 106,5 | 92,3 | 44,48 | 36,44 |
| 93%HDPE/7%$HfO_2$ | 107,7 | 92,3 | 46,16 | 40,76 |
| 90%HDPE/10%$HfO_2$ | 106,8 | 91,5 | 46,59 | 31,57 |

As the mobility of polymer chains increases, the melting temperature decreases that is observed in the experiment. The observed decrease is slight and should not lead to significant change in polyethylene physical properties. For HDPE/$HfO_2$ - based polymer nanocomposites the degree of crystallization at all $HfO_2$ nanoparticle concentration in the polymer increases and reaches maximum value at 7%wt. In Table 1 there have been presented the results of DSC analysis of experimental samples. The obtained data can be explained by the fact that the filler particles are distributed throughout the matrix and can be heterogeneous crystallization centers. Given results are confirmed by SEM spectra.

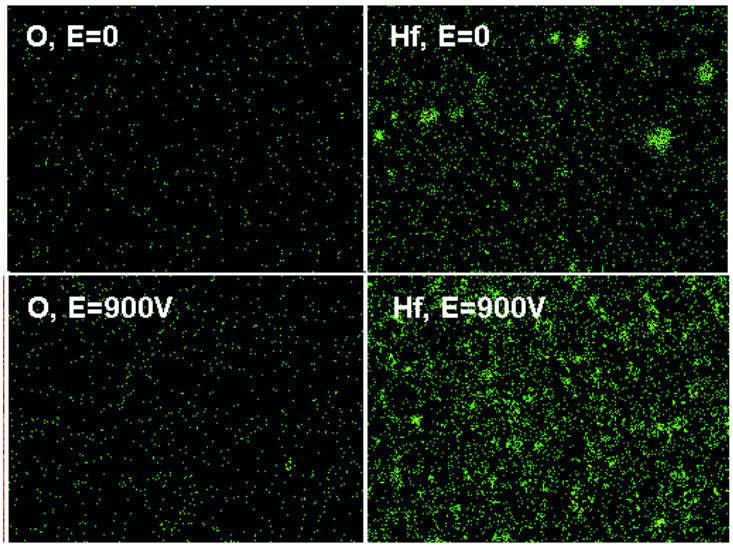


***Fig.4*** *SEM images of elemental distribution in HDPE/5%$HfO_2$ nanocomposite before and after electrothermopolarization*

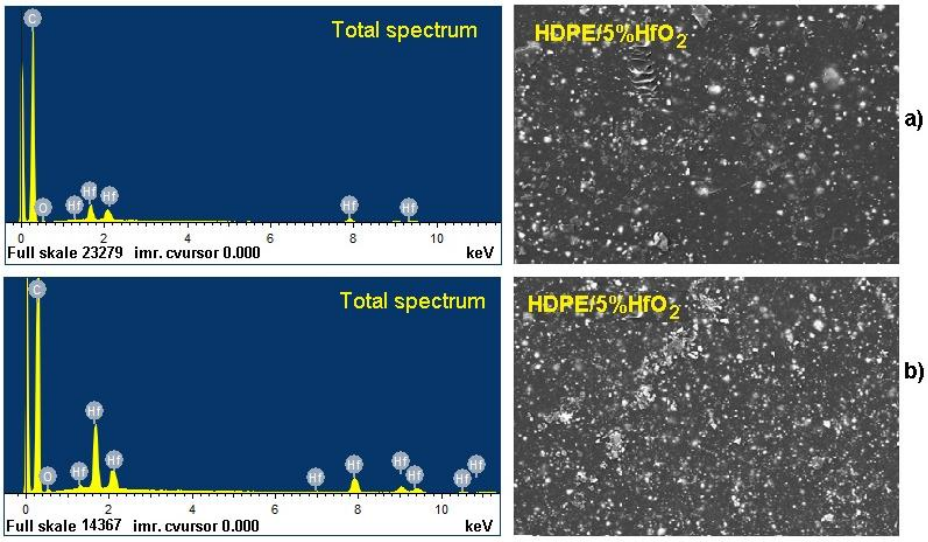


***Fig.5****SEM-EDSimages of HDPE/5%$HfO_2$ polymer nanocomposite before (a) and after (b) ETP*

SEM and SEM-EDS analyses are used to characterize the surface morphology of HDPE/$HfO_2$ nanocomposites. In Fig.4 micrographs of HDPE/$HfO_2$ are shown. The surface morphology of nanocomposites before ETP is rough and phase-separated. After ETP the nanocomposite surface has a smooth and controlled morphology [38-43].

The morphology of samples and distribution of HfO2 nanoparticles throughout the volume of the polymer matrix have been studied by scanning electron microscope (SEM) and energy dispersive spectrum (EDS) (Fig.5. a. b). It is also shown from EDS element analysis (Fig.5. a. b) that obtained nanoparticles are hafnium oxide ones. Fine crystalline particles can be observed on the surface in Fig.5. a.b. Based on SEM images, it can be stated that HfO2 nanoparticles are evenly distributed and aggregated the polymer matrix surface.

## CONCLUSIONS

It is established that incorporating 3–10 wt.% of $HfO_2$ enhances the physical properties of the HDPE/$HfO_2$ nanocomposite by inducing significant structural modifications in the polymer matrix. SEM analysis reveals a high density of specialized structural groups and improved interfacial regions on the surface and within the bulk, which contribute to the high stability of the electret state. XRD and DSC data indicate that the introduction of $HfO_2$ nanoparticles leads to a redistribution of the amorphous and crystalline phases. Specifically, the observed decrease in permittivity is attributed to the partial dissolution or reorganization of the polymer's crystalline phase. Furthermore, the DSC results suggest that a portion of the HDPE matrix adsorbed onto the $HfO_2$ nanoparticle surfaces undergoes localized crystallization, creating a more complex interphase.

**REFERENCES:**


1. Kakhramanov N., Azizov A., Osipchik V., Mamedli U., Arzumanova N., (2016) Nanostructured composites and polymer materials science, *Plastics masses*, 1-2: 49-57.
2. Alkan U., Özcanlı Y., Alekperov V., (2013) Effect of temperature and time on mechanical and electrical properties of HDPE, Fibers *Polym*., 14:115-120.
3. Mansour D., Gawad N., Dein A., Ahmed H., Darwish M., Lehtonen M., (2021) Recent Advances in Polymer Nanocomposites Based on Polyethylene and Polyvinylchloride for Power Cables, *Mater.,* 14:66.
4. Gritsenko V., Perevalov T., Islamov D., (2016) Electronic properties of hafnium oxide: A contribution from defects and traps, *Phys. Rep.,*613: 1-20.
5. Matovic B., Pantic J., Lukovic J., Cebela M., Dmitrovic S., Mirkovic M., Prekajski M.,(2016) A novel reduction-oxidation synthetic route for hafnia, *Ceram. Int,* 42:615-620.
6. Kurbanova N., Mirzoeva N., Ishenko N., Zeynalov E., (2021) Obtaining and studying the properties of composites based on high pressure polyethylene with cobalt-containing nanofillers, *Plastic masses,* Russian, 11:43-45.
7. Ren L., Yang L., Zhang S., Li H., Zhou Y., Ai D., Xie Z., Zhao X., Peng Z., Liao R., Wang Q., (2020) Largely Enhanced Dielectric Properties of Polymer Composites with $HfO_2$ Nanoparticles for High-Temperature Film Capacitors. Journal Pre-proof *Compos Sci Technol*, 201:108528.
8. Huseynova A., Ramazanov M., (2009) The effect of corona discharge on the electret properties of polyolefins modified with the addition of low molecular weight dyes, *Physics* Azerbaijan, 15: 160-161.
9. Ramazanov M., Quseynova A., (2013) Influence of polarization processes on the charge states and dielectric properties of polyethylene-based compositions with low-molecular additions PE+$PbCrO_4$ and PE+CrO *AM – RC*, Romania, 7:789-791.
10. Mekishev G., Yovcheva T., Gentcheva E., Nedev S., (2005) Study of electrets stored of pressures lower than atmospheric, *Electrostat.* 63:1009-1015.

11. Jun Z., Yuan Z., Hong-Bo L., (2005) Iufluence of anucelrug and temperature on distributron of traps in filim electrets neylon-11, *Acta physic* Sin., Poland, 54:3414-3417.
12. Ramazanov M., Huseynova A., (2013) The influence of electrothermopolarization on the electrets properties and charge state of the nanocomposite PE+Cr and PE+$PbCrO_4$, *J. Surf. Eng. Appl*., 49:115.
13. Rahimli A. (2021) Photoluminescence and electret properties of thermoplastic polymer-based nanocomposites modified with metal-oxide nanoparticles, *Physics*, 27:30-35.
14. Rychkov D., Kuznetsov A., Rychkov A. (2011) Electret properties of polyethylene and polytetrafluoroethylene films with chemically modified surface, *IEEE Trans Dielectr Electr Insul*, 18:8-14.
15. Buha J., Arcon D., Niederberger M., Djerdj J., (2011) Solvothermal and surfactant - free synthesis of crystalline $Nb_2O_5$, $Ta_2O_5$, $HfO_2$, and Co-doped $HfO_2$ nanoparticles, *Phys. Chem. Chem. Phys*, 12:15537 -15543.
16. Nabiyev A., Islamov A., Maharramov A., Nuriyev M., Ismayilova R., Doroshkevic A., Pawlukojc A., Turchenko V., Olejniczak A., Rulev M., Almasan V., Kuklin A., (2018) Structural Studies of dielectric HDPE+$ZrO_2$ polymer nanocomposites: filler concentration dependences, *Physics: Conf. Series*, United Kingdom, 994: 012011.
17. Kumar N., George B., Abrahamse H., Parashar V., Ray S., NgilaJ., (2017) A novel approach to low temperature synthesis of cubic $HfO_2$ nanostructures and their cytotoxicity, *Sci. Rep*,United Kingdom, 7: 9351.
18. Patel P., Rani J., Yadav K., (2021) Effective strategies for reduced dielectric loss in ceramic/ polymer nanocomposite film Ceram. Int, 47 10096-10103.
19. Zhang C., Mason R., Stevens G., (2005) Dielectric Properties of Epoxy and Polyethylene, Nanocomposites Proceedings of 2005 *International Symposium on Electrical Insulating Materials*, June 5-9, Kitakyushu, Japan, 393-396.
20. Novikova G., Rabenok E., Kydralieva K., Dzhardimalieva G., (2019) The influence of magnetite nanoparticles on the dielectric properties of nanocomposites based on linear low-density polyethylene, *J. Phys. Chem.*, 93:1824-1829.
21. Prateek., Thakur V., Gupta R., (2016) Recent Progress on Ferroelectric Polymer-Based Nanocomposites for High Energy Density Capacitors: Synthesis, Dielectric Properties, and Future Aspects, Chem. *Rev*,116: 4260-4317.
22. Ramazanov M., Rahimli A., Hajiyeva F., (2020) The influence of titanium dioxide ($TiO_2$) nanoparticles on the structure, optical and dielectric properties of polyvinyl chloride (PVC). *Mod. Phys. Lett. B* 34:2050310
23. Kourtidou D., Grigora M., Tzetzis D., Bikiaris D., Chrissafis K., (2022) Graphene Nanoplatelets' Effect on the Crystallization, Glass Transition, and Nanomechanical Behavior of Poly (ethylene 2,5-furandicarboxylate) Nanocomposites, *Molecules*, 27:20226653.
24. Simonenko E., Simonenko N., Nagornov I., Mokrushin A., Maltseva M., Sevastyanov V., Kuznetsov N., (2021) Dependence of the reactivity of the highly dispersed $Ta_2O_5$–$HfO_2$–C system on the carbonization temperature of the xerogel, *Inorganic Chemistry*, 66:648-657.
25. Huseynova A.S., Rahimli A.M., Hajiyeva F.V., Musayeva N.N. (2024) High-performance HDPE nanocomposites: Investigating the effects of $HfO_2$ and $Ta_2O_5$ on electrical and dielectric properties. Journal of Thermoplastic Composite Materials 38 (11): 4163-4180
26. Chen S., Zhou Y., Luo H., Tang L., Guo R., Zhang D., (2020) Core-shell TiO2@HfO2 Nanowire Arrays with Designable Shell Thicknesses for Improved Permittivity and Energy Density in Polymer Nanocomposites, *Compos. Part A Appl. Sci*. Manuf, 137: 106012.
27. Dabees S., Elshalakany A., Tirth V., Kamel B., (2021) Synthesis and characterization studies of high-density polyethylene -based nanocomposites with enhanced surface energy, tribological, and electrical properties, *Polym. Test*. United Kingdom, 98:107193.
28. Wilk G., Wallance R., Anthony J., (2001) High-κ gate dielectrics: Current status and materials properties considerations, *J. Appl. Phys*., 89:5243-5275.
29. Pomogailo A., Dzhardimalieva G., Rozenberq L., Kestelman V., (2007) Hafnium-containing nanocomposites, J. Thermoplast. Compos. Mater., 20 (2):151-174.
30. Zhang H., Guo W., Yu Y., Li B., Wu C., (2007) Structure and properties of compatibilized recycled poly (ethylene terephthalate)/linear low density polyethylene blends, *Eur. Polym. J*. 43:3662-3670.
31. Maniadi A., Vamvakaki M., Suchea M., Tudose I., Popescu M., Romanitan C., Pachiu C., Ionescu O., Viskadourakis Z., Kenanakis G., Koudoumas E., (2020) Effect of graphene nanoplatelets on the structure, the morphology, and the dielectric behavior of low-density polyethylene nanocomposites, *Materials* 13: 4776.
32. Kukli K., Ritala M., Leskela M., (2001) Development of Dielectric Properties of Niobium Oxide, Tantalum Oxide, and Aluminum Oxide Based Nanolayered Materials, *J. Electrochem. Soc*, 148: 35.

33. Mallick S, Zubair A, Touati F, Shakoor R, Sens *Actuators B Chem*, Netherlands, 288 (2019) 408.
34. Dyakova A., Trifonov S., Sosnov E., Malygin A., (2009) Effect of Chemical Modification on Structural and Energy Characteristics of the Surface of Polyethylene and PolyvinylChloride Films *J. Applied Chemistry*,82:622-629.
35. Ramazanov M., Quseynova A., Gadghieva F., (2009) Influence of temperature and time regimes of crystallization andelectrothermopolarization on the physicalstructures of polypropylene and $MnO_2$-basedcomposition, *OAM-RC*, 10:1204-1206.
36. Ramadoss A., Krishnamoorthy K., Kim S., (2012) Novel synthesis of hafnium oxide nanoparticles by precipitation method and its characterization., 47:2680–2684
37. Ramazanov, M. A., Hajiyeva, F. V., Maharramov, A. M., Hasanova, U. A., & Rahimli, A. M. (2017). The role of the polarization charges in the formation of photoluminescent properties of nanocomposites based on polyvinylidene fluoride and zirconia dioxide nanoparticles. Integrated Ferroelectrics, 183(1), 163–170.
38. Kazimov M.V, Ibragimov G.B. (2024) Fabrication and performance characterization of $Sb_2Se_3$ -GaSe eutectic systems. Semiconductor Physics, Quantum Electronics & Optoelectronics, 27(2):184-188,
39. Kazimov M.V., (2020) Synthesis and structural analysis of InSb-CrSb, InSb-Sb, GaSb-CrSb eutectic composites. Journal of Optoelectronic and Biomedical Materials, 12(3):67-72.
40. Kazimov M.V, İbragimov G.B, İsakov G.I, Ibragimov B.G., (2022) Physical-chemical properties of InSb+Mg 3 Sb 2 eutectic systems: Synthesis, Characterization, And Applications. Journal of Optoelectronic and Biomedical Materials 14(4):187-190.
41. Kazimov M.V, İbragimov G.B, İbragimov B.G, Ibayeva R.Z., (2025) Synthesis, Characterization, And Performance of $Sb_2(S,Se)_3$ based composites, Radioelectronics. Nanosystems. Information Technologies, Radioelectronics. Nanosystems. RENSIT17(5):571-576e.
42. Kazimov M.V, İbragimov G.B, İbragimov B.G., (2025) Synthesis, High-performance thermoelectric behavior InSb-Sb composite systems, Radioelectronics. Nanosystems. Information Technologies, Radioelectronics. Nanosystems. RENSIT, 17(5):697-702e.
43. Kazimov M. V, Arasly D.H, Rahimov R. N, Khalilova A.Kh, Mammadov Kh., (2020) Magnetic and electrical properties of GaSb-CrSb eutectic system. Journal of Non-Oxide Glasses 12(1):7-11.

JOURNAL OF BAKU ENGINEERING UNIVERSITY - PHYSICS
*2025. Volume 9, Number 2* *Pages 101-104*

*UDC: 621.315.592*
*DOI: https://doi.org/10.30546/09081.2025.002.1029*

# EFFECT OF RADIATION BEAMS ON THE ELECTROPHYSICAL PROPERTIES OF GaSe LAYERED SINGLE CRYSTAL

**A.S.ALAKBAROV[1], L.N.IBRAGIMOVA[2], U.S. ABDURAHMANOVA[1]**

*aelakberov@beu.edu.az, uabdurahmanova@beu.edu.az, leyla.ibrahimova.1992@bk.ru*

[1]*Baku Engineering University, AZ-0101, Khirdalan, H. Aslanov st. 120, Absheron, Azerbaijan*

[2] *Nakhchivan State University, AZ-7000, Nakhcivan, Istiqlal st. 85, Azerbaijan*

*ARTICLE INFO*

*Article history:*
*Received:2025-04-29*
*Received in revised form:2025-05-23*
*Accepted:2025-07-06*
*Available online:2025-12-21*

*Keywords:*
*layered single crystal, radiation rays, concentration, mobility, electrical conductivity, low dose effect.*


*ABSTRACT*

*In this research work the result of the investigation of the effect of radiation beams on the electrophysical properties of GaSe layered single crystal. Like other layered single crystals, GaSe single crystal is used in the manufacture of microelectronic devices - photoconverters, high-frequency electronic switches, and a number of optoelectronic structures. Therefore, since the mid-twentieth century, GaSe single crystals have been extensively studied as a research subject. Like other semiconductor materials, the physical properties of germanium monoselenide are affected by external factors, including radiation of various natures. In the article the reasons for the influence of different doses of electrons on the kinetic parameters of GaSe single crystal - hole concentration, mobility, and electrical conductivity has been investigated.*

## 1. INTRODUCTION

Gallium monoselenide is a red (turquoise) layered crystal with a wide range of applications, which has been studied since the fifties of the last century. The GaSe crystal melts at a temperature of 1260 K and its density is 5.03 g/cm$^3$. The GaSe layered single crystal is an $A^{III}B^{VI}$ type semiconductor with a bandgap width of ~ 2 eV. Between the atoms Se-Ga-Se-Ga in the layers there is an ionic-covalent bond and a weak Van der Waals bond between the layers [1]. The layered nature of the crystal leads to strong anisotropy of the refractive index, electrical conductivity, thermal conductivity, mechanical and optical properties, a large ionic radius, and at the same time to the intercalation of impurity atoms with photoluminescence properties between the layers. The high value of birefringence makes it possible to fabricate laser emitters in the infrared and terahertz regions of the spectrum from GaSe crystals [2÷4]. Epitaxial heterojunctions have been made using the layered structure of a GaSe single crystal as a buffer layer [5].

A characteristic feature of the GaSe crystal is that its p-type electrical conductivity does not change even when alloyed with various chemical elements and its microhardness increases when alloyed with *Al, Ag, In* atoms. Only the replacement of S atoms with Se atoms is unlimited and has a strong effect on its electrical and mechanical properties. Thus, as a result of such substitutions, the resistivity of the GaSe crystal varies in the range of $10^2 \div 10^9$ Ohm·cm at room temperature [6]. The reason is the formation of structural defects in a large concentration during the synthesis of the solid solution. To change and control the electrophysical properties of the crystal, not only dopant atoms are used but also the effect of radiation rays of various nature and energy.

High-energy radiation (electron, neutron, ion beam) is used to create radiation defects that affect the electrophysical and optical properties of crystals, including layered crystals and even change the type of crystal. In recent decades, low-dose radiation has been used to affect the electronic and photoelectric properties of GaSe layered crystals [7–8].

## 2. EXPERIMENTAL PART

The authors [9] irradiated GaSe crystal with electrons with an energy of 4 MeV to change and control its electrophysical properties. The process was carried out at a temperature of T=300 K, at integral flux values of $1{,}3\cdot10^{17}cm^{-2}$, $1{,}5\cdot10^{17}cm^{-2}$ and $2{,}8\cdot10^{17}cm^{-2}$ in the Electron Beam Facility- 4 (EBF- 4) accelerator. During the research, sample plates with linear dimensions of 1x1 $cm^2$ and a thickness of 400÷800 μm were used. These samples were exposed to different radiation doses of $1.5\cdot10^{17}cm^{-2}$ and $2.8\cdot10^{17}cm^{-2}$. *In* atoms were applied to prevent heating in ohmic contacts. Electrophysical parameters were measured by the Van der Pauw method in the Ecopia HNS device, in the temperature range of 90÷350 K. The electrophysical parameters of the sample were measured using the Van der Pauw method in an Ecopia HNS device, in the temperature range of 90÷350 K.

It has been established that when a GaSe crystal is irradiated with a low-dose ($\Phi<2.8\cdot10^{17}cm^{-2}$) electron beam, the concentration of free holes decreases. In this case, the activation energy varies in the range of 300÷450 meV which is determined by the temperature dependence of the hole concentration. The temperature dependence of the hole concentration in layered GaSe single crystals exposed to radiation at different doses is shown in Figure 1. As can be seen from the graph, at low values of radiation (curves 2 and 3), a decrease in the hole concentration is observed and with a subsequent increase in the radiation dose an increase is observed. With a further increase in the radiation dose, if the concentration of radiation defects exceeds the concentration of chemical impurities, a compensation process occurs in the crystal [7]. Otherwise, a sharp increase in the hole concentration is observed (curve 4).

It can be assumed that a further increase in the radiation dose would lead to a decrease in the concentration. However, the opposite was observed in the layered GaSe single crystal. It seems that the reason for the current anomaly is the layered structure of the crystal.

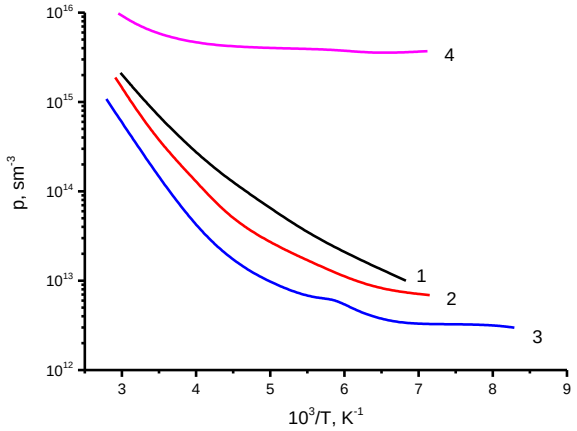


***Figure 1.*** *Temperature dependence of the concentration of free holes in a crystal GaSe:* $\Phi_1=0$; $\Phi_2=1{,}3\cdot10^{17}cm^{-2}$; $\Phi_3=1{,}5\cdot10^{17}cm^{-2}$; $\Phi_4=2{,}8\cdot10^{17}cm^{-2}$.

Thus, a similar phenomenon is not observed in other crystals. The results of many studies show that the same processes are observed when a current is passed along the layers of a GaSe crystal irradiated with electrons and in a direction perpendicular to the surface [8, 9].

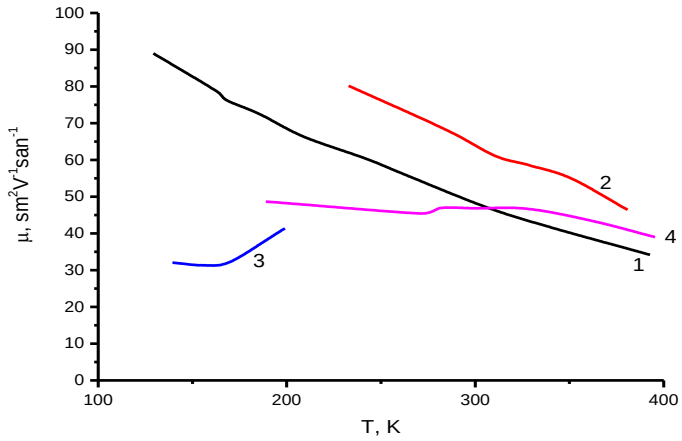


***Figure 2.*** Temperature dependence of the mobility of free holes in a GaSe crystal in a given radiation dose: $Ф_1=0$; $Ф_2=1,3\cdot10^{17}cm^{-2}$; $Ф_3=1,5\cdot10^{17}cm^{-2}$; $Ф_4=2,8\cdot10^{17}cm^{-2}$

The temperature dependence of the electrical conductivity of the GaSe crystal (Fig. 3) shows that at small doses of electron flux ($Ф=1,3\div1,5\cdot10^{17}cm^{-2}$) the electrical conductivity partially decreases. This is due to the fact that newly formed radiation defects are compensated by the inherent defects of the crystal. An increase in the radiation dose led to a further increase in the electrical conductivity. The same increase was also recorded in GaSe crystals doped with various metal atoms.

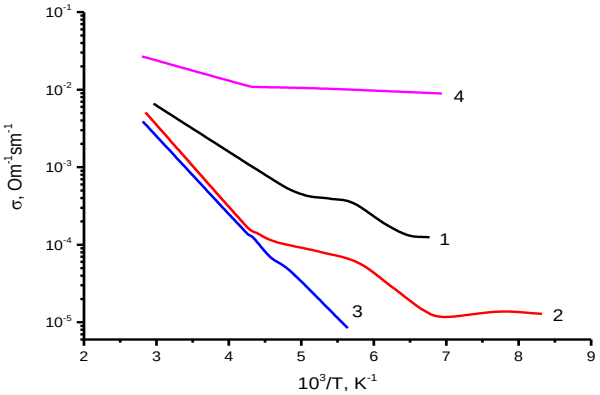


***Figure 3.*** Temperature dependence of electrical conductivity of a GaSe crystal in a given radiation dose: $Ф_1=0$; $Ф_2=1,3\cdot10^{17}cm^{2}$; $Ф_3=1,5\cdot10^{17}cm^{-2}$; $Ф_4=2,8\cdot10^{17}cm^{-2}$.

## 3. ANALYSIS OF RESULTS

The dependence of the concentration of charge carriers, their mobility, and the overall electrical conductivity of GaSe layered single crystals versus dose of electron irradiation, as well as versus temperature has been studied. The decrease in the concentration of holes at low doses of irradiation can also be explained by the formation of donor-type radiation defects in the crystal

under the influence of irradiation [5]. Another reason for the decrease in the concentration is the compensation of Frenkel defects by the migration of defects formed in the crystal during synthesis and growth of the single crystal under the influence of low doses of electrons [10]. At high values of the irradiation dose ($\Phi$=2,8·$10^{17}$$cm^{-2}$), the degradation process in the crystal leads to an increase in the concentration of holes, which leads to a violation of high order.

When irradiating a GaSe crystal at a small dose ($\Phi$=1,3·$10^{17}$$cm^{-2}$), it leads to the formation of an ordered structure and an increase in the mobility of charge carriers (Fig. 2, curve 2). A further increase in the radiation dose leads to a decrease in the mobility due to the formation of radiation defects (curves 3,4). Like other semiconductor crystals, the electrical conductivity of the GaSe crystal also depends on the concentration of charge carriers. However, since the electrical conductivity depends more on the concentration than on the mobility, the electrical conductivity of samples irradiated at a small dose (Fig. 3, curves 2 and 3) decreases sharply compared to the unirradiated sample (as a result of compensation).

When the radiation dose is increased, as a result of the disordering of the crystal, the concentration of charge carriers increases sharply and the mobility decreases [10, 11].

Thus, summarizing the results of the study, it can be concluded that, depending on the type of crystal, growth technology and irradiation mechanism at low doses of irradiation a compensation phenomenon occurs in the crystal accompanied by high order (increase in mobility) and defect migration [12, 13]. A continuous increase in the irradiation dose leads to a decrease in the mobility of charge carriers and an increase in their concentration.

**REFERENCES**


1. N.B. Singh, D.R. Suhre, V. Balakrishna, M. Marable, R. Meyer, N. Fernelius, F.K. Hopkins, D. Zelmon. Prog. Cryst. Growth Character. Mater. 37, 47 (1998).
2. K.R. Allakhverdiev, M.O.Yetis, S.Ozbek, T.K. Baykara, E.Yu. Salaev. Laser Phys. 19, (5) 1092 (2009).
3. M.M. Nazarov, S.Y. Sarkisov, A.P. Shkurinov, O.P. Tolbanov. Appl. Phys. Lett. 99, (8) 081105-1-3 (2011).
4. R.S. Madatov, A.S. Alekperov, S.A.Haciyeva, N.M. Muradov, R.E. Huseynov. East European Journal of Physics. 3, 322-327 (2024).
5. J.E. Palmer, T. Saitoh, T.Yodo, M.J.Tamura. Cryst. 1995. 150, 685 (1995).
6. K. Allakhverdiev, T. Baykara, S. Ellialtioglu, F. Hashimzade, D. Huseinova, K. Kawamura, A.A. Kaya, A.M. Kulibekov, S. Onari. Mater. Res. Bull, 41, (751) 2006.
7. В.Н.Брудный, А.В.Кособуцкий, С.Ю.Саркисов. ФТП. 44, (9), 1194 (2010).
8. А.А. Исмаилов, Г.И. Исаков, Н.Д. Ахмедзаде, М.М. Ширинов. Альтер. энер.и экол. 86, (6) 48 (2010).
9. З.Д.Ковалюк, О.А.Политанская, О.Н.Сидор, В.Т.Маслюк . ФТП. 42, (11) 1321 (2008).
10. А.П. Мамонтов, И.П. Чернов. Эффект малых доз ионизирующего излучения. Томск.: Дельтаплан, 209 с, 2009.
11. В.Т. Мак. Письма в ЖТФ. 15, (4) 17 (1989).
12. В.С. Вавилов, А.Р. Ниязова, А.Е. Кив. Механизм образования и миграция дефектов в полупроводниках. М.: Наука, 368 с, 1981.
13. В.С. Вавилов. Действие излучения на полупроводники. М.: Физ-маттиз, 278 с, 1963.

JOURNAL OF BAKU ENGINEERING UNIVERSITY - PHYSICS
*2025. Volume 9, Number 2* *Pages 105-111*

*UOT 536.77:547.442*
*DOI: https://doi.org/10.30546/09081.2025.002.1031*

# GENERALIZATION OF EXPERIMENTAL DATA ON THE VISCOSITY AND DENSITY OF THE "KHACHMAZ" THERMAL WATER OF THE KHACHMAZ REGION OF AZERBAIJAN

**M. M. BASHİROV[1], N. D. NABİYEV[1], A. M. NAMAZOVA[1], N. S. RZAYEV[1]**

[1]*Baku Engineering University*

*AZ0101, Khirdalan city, Hasan Aliyev str. 120, Absheron, Azerbaijan*

*mbashirov@beu.edu.az, nnabiyev@beu.edu.az, aynamazova@beu.edu.az , nzayev@beu.edu.az*

***ARTICLE INFO***

*Article history:*
*Received:2025-05-20*
*Received in revised form:2025-06-17*
*Accepted:2025-07-13*
*Available online:2025-12-21*

*Keywords:*
*Density, dynamic viscosity, kinematic viscosity, temperature, thermal waters*



***ABSTRACT***

*The main objective of the research is to analytically generalize the experimental results of the dynamic and kinematic viscosity, as well as the density, of the "Khachmaz" thermal water from the Khachmaz region of Azerbaijan at various temperatures. As a result of the scientific studies conducted by us, the data obtained from the "Stabinger SVM 3000" viscometer for dynamic viscosity (η) and kinematic viscosity (ν), and from the experimental setup operating on the vibrating-tube densimeter method for the density (ρ) of the thermal water, were used in this work.*

*Then, based on the experimental results of the "Khachmaz" thermal water obtained under the same temperature conditions in the η–ρ and ν–ρ coordinate systems determined using polynomial equations, the dependencies η = f(ρ) and ν = f(ρ) were proposed in the article. The polynomial coefficients were calculated from the experimental data using the least squares method and are presented in a table. Considering the proposed equations and polynomial coefficients, it is possible to calculate the values of the dynamic viscosity (η) and kinematic viscosity (ν) of the "Khachmaz" thermal water from the Khachmaz region of Azerbaijan at different temperatures within the experimental error range.*

## 1. INTRODUCTION

As a result of various geological and volcanic processes, thermal waters that reach the Earth's surface at high temperature and pressure by utilizing the planet's natural heat are widely used as alternative energy sources. The extraction of heat from geothermal sources was first implemented in Italy in 1904. Later, various facilities were constructed in New Zealand, Japan, the Philippines, and the United States for the production of geothermal energy. For instance, about 95% of the heating system in Reykjavik, Iceland, is supplied by geothermal energy.

There are various geothermal technologies with different levels of development that are widely used in central heating plants, heating systems, and other application areas. The technology of generating electric power from naturally permeable hydrothermal reservoirs is also considered reliable. At present, most of the geothermal power plants operating worldwide are based on dry steam turbines or "flash" systems (single, double, or triple flash) and are used for hot water sources with temperatures above 180°C. In addition, new technologies such as "Enhanced Geothermal Systems (EGS)" which are in the development stage are also being advanced [1].

According to data from the UN Commission on Global Warming, the Earth's surface temperature has risen by 3°C over the past 170 years. The continuation of this process poses a

global warming threat to the planet. Currently, the accelerated melting of Alpine glaciers, the annual rise of ocean (sea) levels by 1÷2 mm-amounting to 10÷20 cm over the past 100 years and the 0.3°C increase in the temperature of tropical seas since 1994 all serve as evidence of this phenomenon [1–3].

At present, geothermal energy is one of the least utilized alternative energy sources in the world. However, as the quantity of conventional energy resources decreases and their prices continue to rise, the demand for alternative energy sources is increasing, which will lead to a wider use of geothermal energy. Currently, in many developed countries, geothermal energy is primarily used for power generation (by driving turbines with geothermal steam) and for domestic heating systems as a source of hot water.

In order to utilize thermal waters as alternative energy sources, it is essential to study their properties. One of the primary requirements is the chemical analysis of the waters and the investigation of the geological structures of the areas where these waters emerge. In addition, the study of key thermophysical parameters such as dynamic and kinematic viscosity, as well as density that determine the thermal properties of these waters is also of great importance. Significant scientific research has been carried out worldwide by scholars in this field.

By making extensive and efficient use of thermal and mineral waters, it is possible to establish many new sectors in our country, such as mineral water bottling plants, chemical and energy industries, medical and health facilities, as well as tourism and recreational centers. This would have a positive impact on the employment of the workforce in the country. As a result, the problem of unemployment could be partially alleviated, catering establishments would expand, and agricultural sectors would develop to meet the food demands of tourists.

In Azerbaijan, significant work has been carried out in this direction over the past 21 years. The Republic of Azerbaijan confirmed its target regarding alternative and renewable energy sources as early as 2004 [2]. Among these renewable energy sources are geothermal energy resources, which are derived directly or indirectly from chemical substances, hot water, and steam generated by heat accumulated at various depths of the Earth. Geothermal energy can also be used for heating and cooling purposes or for the production of clean electricity. The role of thermal waters as underground heat energy accumulators, as well as their high thermal energy capacity, highlights their special importance among renewable energy sources.

Although the Republic of Azerbaijan is rich in thermal water resources, only a very small portion is currently utilized. Depending on usability, as well as geostructural and hydrogeothermal conditions, the country's thermal resources are concentrated in the following regions: Greater Caucasus, Absheron Peninsula, Caspian-Quba, Kura-Araz Lowland, Lesser Caucasus, Talysh-Lankaran, Jalilabad-Zar, Shamakhi-Gobustan, Aghinokhur-Kur interfluve, and Nakhchivan hydrothermal zones. Although the total reserve of these thermal regions amounts to 249,000 $m^3$/day, the majority of these resources are used for therapeutic purposes [3–5]. The temperature of Azerbaijan's mineral waters ranges from 4°C to 65°C, which applies only to natural water sources. In addition, geothermal waters with temperatures reaching up to 95°C have been extracted through deep drilling in the country.

In Azerbaijan, there are more than 200 underground, thermal, mineral, and drinking water resources enriched with various minerals, with a total capacity exceeding 100 million liters per day. Significant scientific research in this field has also been conducted in Azerbaijan over a long period [1–8]. The country's thermal water sources, including their chemical composition and

related characteristics, have been studied to a considerable extent. Nevertheless, the thermophysical properties of these thermal waters remain relatively under-researched [6–8].

## 2. RESEARCH METHODOLOGY

The Khachmaz district of Azerbaijan is rich in valuable thermal energy resources, encompassing all types of waters, including carbon dioxide–carbonate, carbon dioxide–chloride, and hydrogen sulfide–sulfate waters. The diverse chemical composition of the district's thermal waters, their high therapeutic properties, and the favorable geographical location of the area provide a solid foundation for the use of these thermal waters for medical treatments as well as for various sectors of the national economy.

The main objective of this study is the analytical generalization of the experimental results of the dynamic viscosity (η), kinematic viscosity (ν), and density (ϱ) of the "Khachmaz" thermal water from the Khachmaz district of Azerbaijan at various temperatures.

The dynamic and kinematic viscosities of the "Khachmaz" thermal water from the Khachmaz district have been studied experimentally. The main objective of these investigations is to reveal the potential of alternative energy resources in the northern regions of Azerbaijan.

The experiments were conducted using the Stabinger SVM 3000 viscometer (Figure 1). The device features a very compact design, ease of use, and high accuracy (0.1÷0.35%). Its main operating principle is based on the constant rotation of a tube inside the device. The substance under investigation is filled into the tube, which is equipped with a coaxial rotor. The friction between the tube and the sample inside forces both the sample and the rotor to rotate.

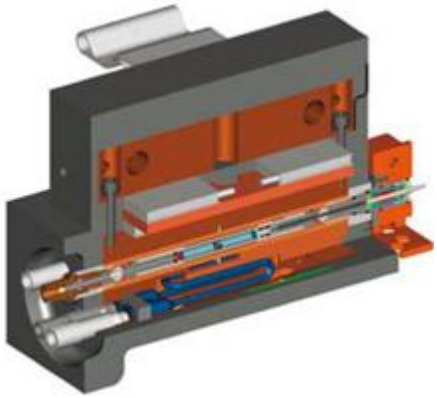

***Figure 1.*** *Internal structure of the Stabinger SVM 3000 viscometer.*

When there is no resistance, all three components rotate at the same speed. It should also be noted that a magnet inside the rotor acts as a brake. The magnetic field generated around the magnet creates eddy currents. These currents extract energy from the rotor, causing it to experience a braking effect. As a result, a difference arises between the speeds of the tube and the internal rotor, which is characterized as viscosity [7].

During the experiments, the dynamic and kinematic viscosities of the "Khachmaz" thermal water were measured. The thermal waters were collected directly from their source areas and prepared for testing through various chemical purification procedures. To ensure measurements were performed under conditions as close as possible to those at the Earth's surface, all dissolved gases and air in the thermal water were removed, and natural samples were also used.

The experiments were carried out in the temperature range of T = 278.15÷343.15 K and at atmospheric pressure. Since the Stabinger SVM 3000 viscometer allows simultaneous measurement of dynamic viscosity and density, the device automatically calculates the kinematic viscosity ν (m²/s) using the following relation for viscosity:

$$\nu = \frac{\eta}{\rho} \qquad (1)$$

Here, η is the dynamic viscosity (Pa·s) and ϱ is the density (kg/m³).

The density of the "Khachmaz" thermal water was measured at atmospheric pressure (p = 0.101 MPa) within the temperature range of T = 278.15÷343.15 K.

## 3. RESULTS AND DISCUSSION

The experimental values of the dynamic viscosity (η), kinematic viscosity (ν), and density (ϱ) of the "Khachmaz" thermal water from Azerbaijan are presented in Tables 1 and 2:

***Table 1***. *Experimental values of dynamic viscosity η (Pa·s) and kinematic viscosity ν (m²/s) of the "Khachmaz" thermal water from Azerbaijan at various temperatures under atmospheric pressure.*

| T/K | $\eta$ | $\nu$ |
|---|---|---|
| 278,147 | 1537,60 | 1,53195 |
| 288,147 | 11780,0 | 1,17484 |
| 298,150 | 937,70 | 0,93778 |
| 313,152 | 713,16 | 0,71619 |
| 328,153 | 559,22 | 0,56528 |
| 343,152 | 421,66 | 0,42977 |

***Table 2.*** *Experimental values of the density ρ (kg/m³) of the "Khachmaz" thermal water from Azerbaijan at various temperatures under atmospheric pressure.*

| T/K | ρ/ kq/m³ |
|---|---|
| 278,15 | 1003,80 |
| 288,15 | 1002,80 |
| 298,15 | 1000,54 |
| 313,15 | 995,80 |
| 328,14 | 989,10 |
| 343,16 | 981,20 |

The temperature dependence of the dynamic viscosity, kinematic viscosity, and density of the "Khachmaz" thermal water from Azerbaijan is shown in Figures 2–4. As seen from Figures 2–4, the dynamic and kinematic viscosities, as well as the density of the "Khachmaz" thermal water, exhibit the same trend as the temperature dependence of the dynamic and kinematic viscosities of pure water, decreasing significantly with increasing temperature.

The figures also show that the experimental values of the dynamic viscosity (η), kinematic viscosity (ν), and density (ϱ) of the investigated thermal water are higher than those of pure water, which constitutes the main component of thermal waters [9,10]. Based on the analysis of the chemical composition of the "Khachmaz" thermal water, it can be concluded that these differences are due to the presence of numerous chemical elements in the sample [4]. Therefore,

dissolved chemical substances, gases, and air influence the dynamic viscosity and density of the thermal water, resulting in higher viscosity and density compared to pure water.

The dynamic and kinematic viscosities of the "Khachmaz" thermal water from Azerbaijan have been described as polynomial functions of temperature as follows:

$$\eta = \sum_{i=0}^{3} a_i T^i \qquad (2)$$

$$\nu = \sum_{i=0}^{3} b_i T^i \qquad (3)$$

Here, $a_i$ and $b_i$ are the coefficients of the polynomials. The values of these coefficients, calculated using the least squares method, are presented for the investigated thermal water in Table 3.

***Table 3.*** *The coefficients $a_i$ and $b_i$ in equations (2) and (3) representing the polynomial temperature dependence of the dynamic and kinematic viscosities of the "Khachmaz" thermal water from Azerbaijan.*

| $a_i$ | $b_i$ |
|---|---|
| $a_0$=527.256774 | $b_0$=530.37865 |
| $a_1$=- 6.208266 | $b_1$=- 6.249937 |
| $a_2$=0.027522 | $b_2$=0.027726 |
| $a_3$=- 0.543113·10$^{-4}$ | $b_3$=- 0.547516·10$^{-4}$ |
| $a_4$=0.402·10$^{-7}$ | $b_4$=0.405·10$^{-7}$ |

Considering equations (2) and (3) and the polynomial coefficients (Table 3), it is possible to calculate the dynamic (η) and kinematic (ν) viscosities of the "Khachmaz" thermal water at various temperatures within the experimental error range. These equations also allow for the interpolation and extrapolation of dynamic (η) and kinematic (ν) viscosity values beyond the measured experimental data.

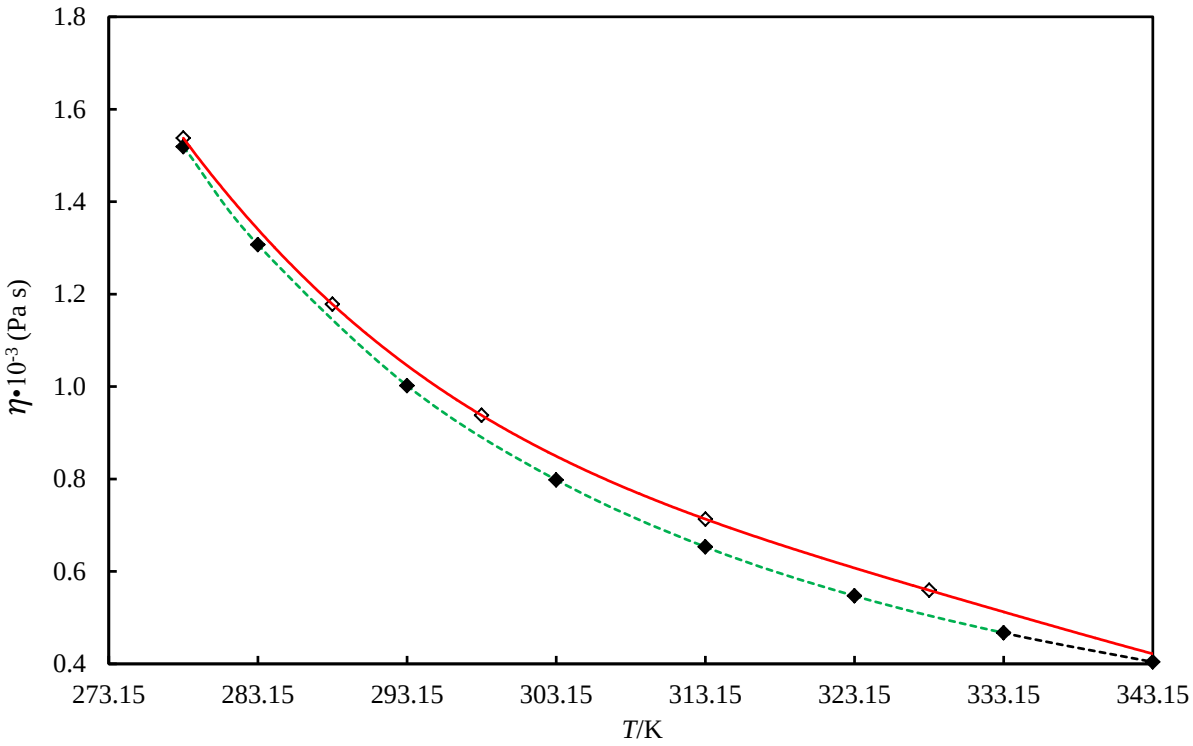


***Figure 2.*** *Temperature dependence of the dynamic viscosity η (Pa·s) of the geothermal waters from the Khachmaz district of Azerbaijan: (◊, "Khachmaz"; --♦--, Water [9]).*

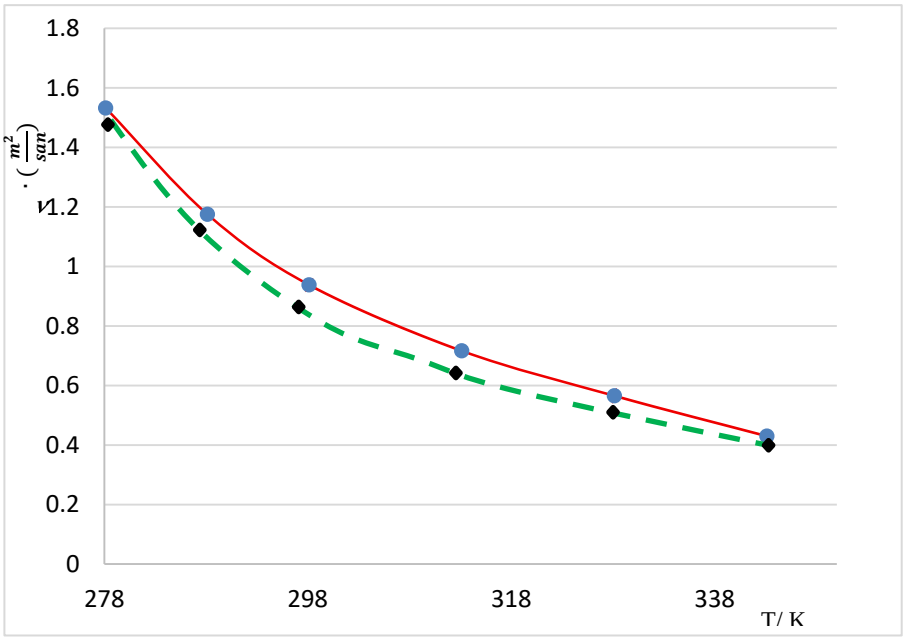


***Figure 3.*** *Temperature dependence of the kinematic viscosity ν (m²/s) of the geothermal waters from the Khachmaz district of Azerbaijan: (●, "Khachmaz"; --♦--, Water [9]).*

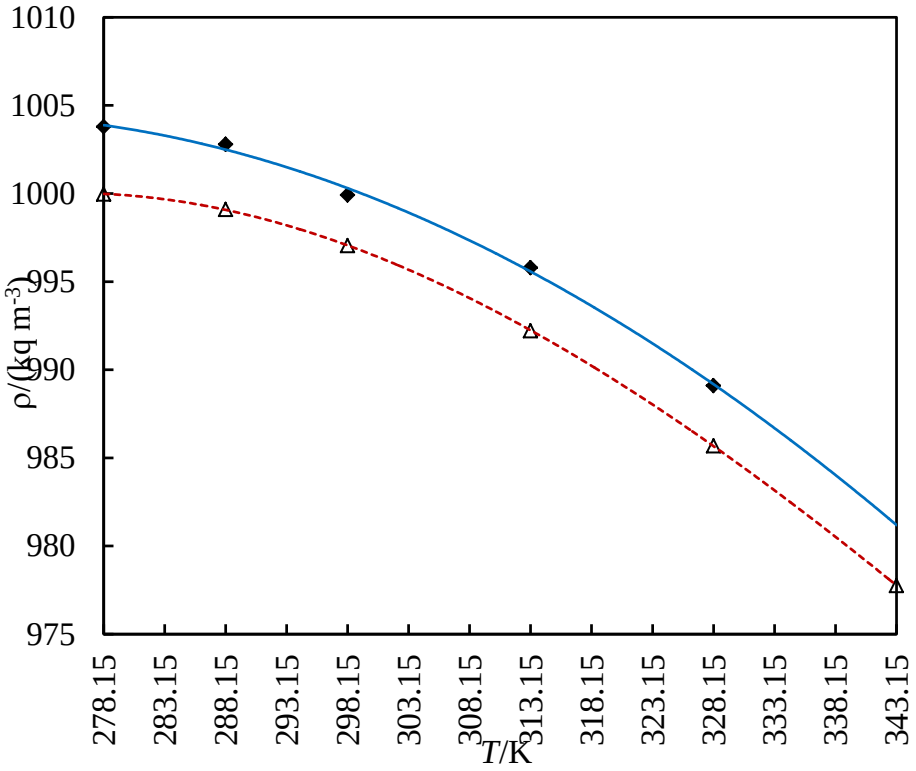


***Figure 4.*** *Temperature dependence of the density (ρ) of the "Khachmaz" thermal water from the Khachmaz district of Azerbaijan: (♦, "Khachmaz"; --Δ--, Water [10]).*

Based on the experimental results (Tables 1 and 2) and using the data of the "Khachmaz" thermal water obtained under the same temperature conditions in the η–ϱ and ν–ϱ coordinate systems, the following polynomial equations were proposed in the article to describe the dependencies η = f(ϱ) and ν = f(ϱ):

$$\eta = \sum_{i=0}^{4} a_i \cdot \rho^i \qquad (4)$$

$$\nu = \sum_{j=0}^{4} b_j \cdot \rho^j \qquad (5)$$

Here, $a_i$ and $b_j$ are the polynomial coefficients calculated from the experimental data using the least squares method and are presented in Table 3.

***Table 4***. *Values of the coefficients $a_i$ and $b_j$ for the "Khachmaz" thermal water from Azerbaijan, obtained from equations (4) and (5).*

| $a_i$ | | $b_j$ | |
|---|---|---|---|
| $a_0$ | $-0.224957 \cdot 10^9$ | $b_0$ | $-0.223394 \cdot 10^6$ |
| $a_1$ | $0.597108 \cdot 10^{+6}$ | $b_1$ | $0.592956 \cdot 10^{+3}$ |
| $a_2$ | $-0.431975 \cdot 10^{+3}$ | $b_2$ | -0.428976 |
| $a_3$ | -0.027641 | $b_3$ | $-0.274363 \cdot 10^{-4}$ |
| $a_4$ | $0.874658 \cdot 10^{-4}$ | $b_4$ | $0.868507 \cdot 10^{-7}$ |

Considering equations (4) and (5) and the polynomial coefficients (Table 4), it is possible to calculate the dynamic (η) and kinematic (ν) viscosities of the "Khachmaz" thermal water at various temperatures within the experimental error range. These equations also allow for the interpolation and extrapolation of dynamic (η) and kinematic (ν) viscosity values beyond the measured experimental data.

**REFERENCES**


1. Tagiev I.I., Ibragimova I.Sh., Babaev A.M. (2001) *Resources of Mineral and Thermal Waters of Azerbaijan*, Baku, Chashioglu, 168 pp.
2. The State Program on Use of Alternative and Renewable Energy Sources in Azerbaijan Republic (approved by the order of the President of the Azerbaijan Republic, no. 462 dated October 21, 2004)
3. Ibrahimova, I.Sh, Babayev, A.M. (2000) Scientific basis for the preparation of the cadastre of mineral waters of Azerbaijan. In: Proceedings of the 3rd Republican Scientific-Technical Conference// Mineral Resources of Azerbaijan, Forecasting of Promising Areas and New Research Methods. Baku, pp. 98–100.
4. Namazova, A.M. (2017) Economic-geographical studies of the thermal and mineral water resources of the Greater Caucasus// Dissertation for the degree of Doctor of Philosophy in Geography, Baku, 158 p.
5. Namazova A.M. (2016) Thermal and mineral water of Guba- Khachmaz economic region, their rational use opportunities// Proceedings of young scientists. No. 13, pp.61-68
6. Bashirov M.M, Shahverdiyev, A.N, Nabiyev N.D. (2013) Thermo-physical properties and measurement methods of geothermal energy sources in the Khachmaz district of the Republic of Azerbaijan// Scientific Publishing, Baku, Azerbaijan, 190 p.
7. N.D.Nabiev. (2011) Study of thermal-physical properties of geothermal energy resources of the Khachmaz region of Azerbaijan// Dissertation submitted for the degree of Doctor of Philosophy in Engineering, Baku, 177 p.
8. N.D.Nabiev, M.M.Bashirov, J.T.Safarov, A.N.Shahverdiyev, E.P.Hassel. (2009) Thermodynamic properties of geothermal energy resources (Khachmaz Sabir-Oba) of Azerbaijan// Journal of Chemical and Engineering data, Vol. 54,No.6.
9. Sengers J.V., Kayser R.F., Peters C.J., White Jr. H.J. (eds.) (2000): Equations of State for Fluids and Fluid Mixtures, Amsterdam: Elsevier Science, 928 p.
10. Wagner W., Pruß A. (2002) The IAPWS formulation 1995 for the thermodynamic properties of ordinary water substance for general and scientific use // Journal of Physical Chemistry Reference Data, vol. 31, pp. 387-535.

JOURNAL OF BAKU ENGINEERING UNIVERSITY - PHYSICS
*2025. Volume 9, Number 2* *Pages 112-120*

*UDC:539.219.3;358.931-405*
*DOI:* **https://doi.org/10.30546/09081.2025.002.1034**

# INFLUENCE OF Gd DOPING ON THE THERMOELECTRIC AND MAGNETO-TRANSPORT PROPERTIES OF SnSe

**T.A.JAFAROV[1], O.M.HASANOV[1], J.I.HUSEYNOV[1], Kh.A.ADGOZALOVA[1], G.A.GARASHOVA[1], I.I.ABBASOV[2]**

[1]*Azerbaijan State Pedagogical University*
*AZ-1000, Baku, Uz. Hajibeyli Str.68, Baku, Azerbaijan*
jahangirhuseynov1958@gmail.com
[2]*Azerbaijan State Oil and Industry University*
*Az-1010, Baku, Azadlıq Avenue 20, Azerbaijan*
ibrahimabbasov179@gmail.com

***ARTICLE INFO***

*Article history:*
*Received:2025-06-01*
*Received in revised form:2025-06-16*
*Accepted:2025-07-02*
*Available online:2025-12-21*

*Keywords: $Gd_xSn_{1-x}Se$, layered crystals, thermoelectric properties, Nernst–Ettingshausen effect, rare earth elements, thermal conductivity, Hall coefficient, conductivity, doping, crystal lattice defects.*


***ABSTRACT***

*This work presents the results of synthesis and investigation of solid solutions in the $Gd_xSn_{1-x}Se$ system, obtained by direct melting followed by annealing. The phase composition, microstructure, kinetic parameters, as well as thermoelectric and thermomagnetic properties at various temperatures and magnetic fields were studied. It was found that the addition of gadolinium ions affects the type of conductivity, reduces the concentration and mobility of carriers, changes the Hall coefficients and thermoelectric power, and also enhances the longitudinal and transverse Nernst–Ettingshausen effects. The obtained data confirm the prospects of Gd-doped layered SnSe crystals for applications in thermoelectrics and sensor devices.*

## 1. INTRODUCTION

Layered crystals are materials consisting of atomic layers held together by van der Waals forces. Due to their unique physicochemical properties and their intermediate position between molecular and nanostructures, they are considered promising nanomaterials [1, 2]. The properties of low-dimensional structures formed based on binary compounds depend on the type of chemical bonding and crystal structure [3, 4]. Binary compounds of the type $A^{IV}B^{VI}$ $(GeS, GeSe, SnS, SnSe)$ have anisotropic layered structures, which allow them to be exfoliated into atomically thin layers, similar to graphene. This makes them promising for $2D$ electronics and nanotechnologies [5, 6]. Low thermal conductivity and high anisotropy of electrical properties enhance their thermoelectric performance [7].

The addition of rare earth elements (REEs) into $SnSe$ leads to changes in electrophysical properties due to defect structures. REEs are characterized by low solubility and the ability to reduce background impurities [8, 9]. Doping improves conductivity, reduces thermal conductivity, and increases material stability, making it particularly suitable for thermoelectric applications [10, 11]. Thermomagnetic properties, which depend on temperature and magnetic field, are important for understanding charge carrier scattering mechanisms and developing

sensors, microelectronics, and energy systems [12–14]. These effects provide deeper insight into interactions in solids than carrier mobility alone.

In this regard, the synthesis and investigation of solid solutions based on $SnSe$ with $Gd$ addition—a typical representative of REEs—are of interest. In this work, such solutions were obtained and their thermomagnetic properties, including the transverse and longitudinal Nernst–Ettingshausen effects, were studied.

## 2. EXPERIMENTAL SECTION

For the synthesis of $SnSe-GdSe$ alloys, tin of grade "B4-000", selenium "OC417-4", and chemically pure gadolinium (99.98%) were used. Synthesis was performed by a two-step direct melting method in evacuated quartz ampoules ($0.1333\ Pa$). At the first stage, the material was heated to the melting temperature of selenium at a rate of $4-5\ °C/min$ and held for $3-4\ hours$. Then the temperature was raised to $950-1000\ °C$ (depending on composition) and maintained for $8-9\ hours$. The resulting samples were annealed for $140-210\ hours$ in an argon atmosphere, with the annealing time increasing with higher $Gd$ content [15].

Phase composition and physicochemical properties were studied using DTA, XRD, microstructural analysis, as well as microhardness and density measurements. DTA was performed on an STA 6000 instrument (Perkin Elmer, USA) in a nitrogen atmosphere ($20\ ml/s$) with heating up to the melting temperature at $5\ °C/min$. X-ray structural analysis was carried out on a Miniflex diffractometer (Rigaku) at $30\ kV, 10\ mA$, using $CuK\alpha$ radiation ($\lambda = 1.5406$ Å), in the $2\theta$ range from 0 to 60°. Surface morphology was investigated using a JEOL JSM6610-LV scanning electron microscope.

Thermoelectric and thermomagnetic characteristics were measured by the steady-state compensation method. At temperatures of $300-620\ K$, thermoelectric power, as well as transverse $(E_y)$ and longitudinal $(\Delta S/S_0)$ Nernst–Ettingshausen effects, were determined under a magnetic field of $11.000\ Oe$ [16]. Measurement errors were approximately 4.6% and 7.1%, respectively.

## 3. RESULTS AND DISCUSSION

**Thermal analysis of the $Gd_xSn_{1-x}Se$ alloy system revealed no thermal anomalies other than the effect corresponding to melting.** Substitution of part of the tin atoms in the binary $SnSe$ compound with terbium atoms leads to a decrease in the melting temperature. Analysis of the intensities of the $X-$ray reflections indicates the presence of a predominant crystallographic orientation and shows that the studied sample consists of a single phase. Indexing of the $X-$ray diffraction patterns demonstrates that, within the solubility range of Tb in $SnSe$, the investigated alloys crystallize in the orthorhombic system with space group $D_{2h}^{16}-Pcmn$ (Fig. 1). In the range $0 \le x \le 0.05$, no shifts of diffraction lines are observed, and only changes in their intensities indicate the formation of solid solutions based on $SnSe$. Changes in diffraction line intensities without their shifts confirm the formation of a substitutional solid solution within the $Gd$ solubility range [17]. The lattice parameters increase linearly, consistent with Vegard's law.

**The results of comprehensive physico-chemical analyses confirm that the $Gd_xSn_{1-x}Se$ alloy system, like the parent compound SnSe, crystallizes in the orthorhombic system.** With

increasing TbSe concentration, a slight increase in unit cell parameters, density, and microhardness is observed, while thermal effects shift to relatively lower temperatures.

The introduction of $Gd$ causes charge carrier scattering and an increase in unit cell parameters without significantly affecting density, indicating the formation of Frenkel-type defects [18]. It has been established that the solubility limit of $Gd$ in $SnSe$ at room temperature does not exceed $2\ mol.\%$. Microstructure and physicochemical property studies confirm that with increasing $GdSe$ content, lattice parameters and microhardness increase, while thermal effects shift toward lower temperatures [19, 20].

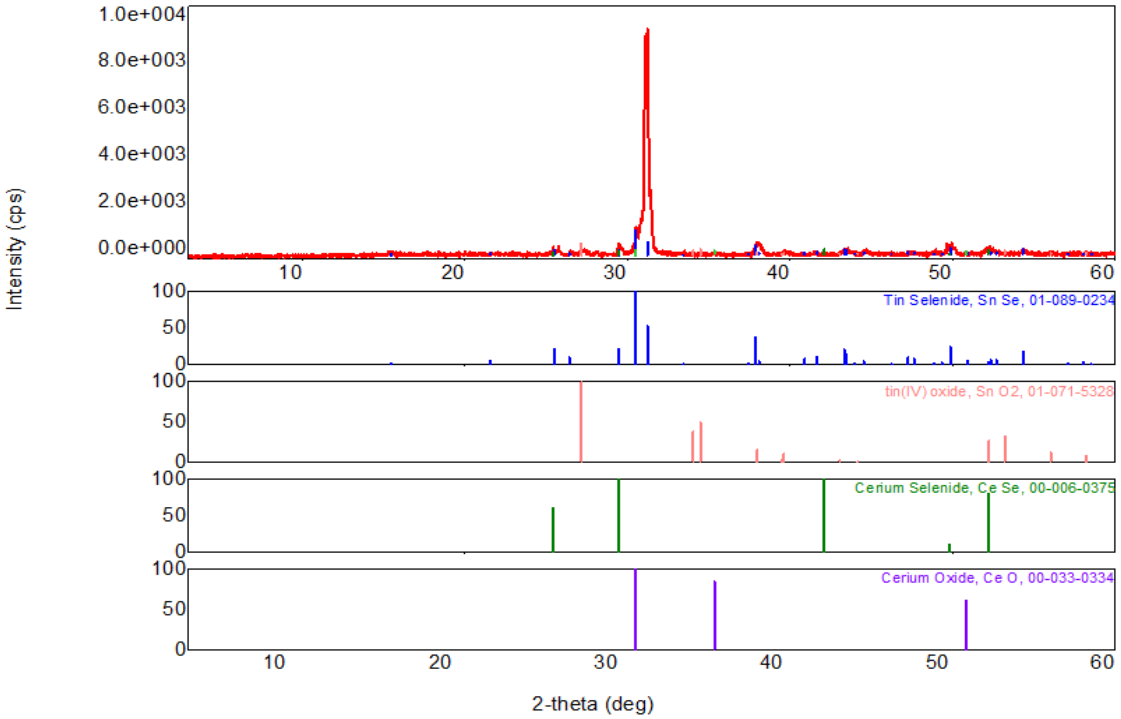


*ray diffractograms of SnSe, SnO, GdSe and GdO compounds*

Despite the layered nature of $SnSe$ single crystals, certain surface roughness is observed on the natural fracture surfaces (Fig. 2a). Atomic force microscopy (AFM) images show that the natural surface homogeneity of SnSe single crystals varies within approximately $25\ nm$ (Fig. 2b). This roughness is likely caused by the weakness of interlayer van der Waals interactions; when these bonds break, atomic clusters, rather than individual atoms, remain on the surface [21].

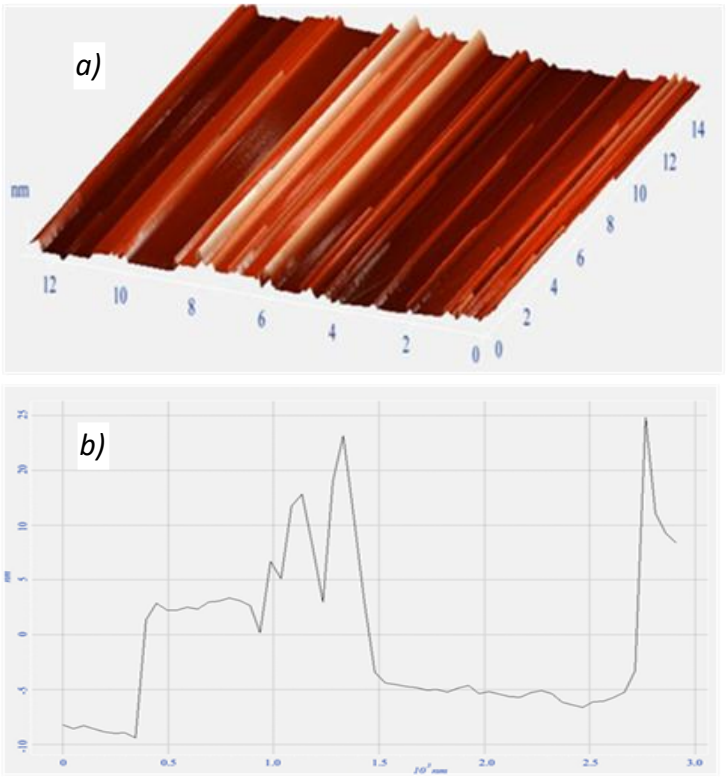


*Figure 2. a) Surface roughness and b) surface profilogram of $Tb_xSn_{1-x}Se$ crystalsl*

**As the content of rare-earth metals (REMs) in $Gd_xSn_{1-x}Se$ single crystals increases, the surface roughness also increases.** Partial substitution of tin atoms in the SnSe binary compound by REM atoms with larger atomic radii leads to enhanced interlayer van der Waals interactions. Therefore, with increasing $Gd$ content in the $Gd_xSn_{1-x}Se$ alloy system, delamination along crystallographic planes becomes more difficult, resulting in increased surface inhomogeneity. This is also confirmed by Fourier spectra obtained via atomic force microscopy.

**Quantitative X-ray microanalysis was used to determine the phase composition and the distribution of chemical elements on the surface of the studied sample.** The analysis of the obtained results indicates surface homogeneity; however, changes in stoichiometry within the homogeneity region of $SnSe$ reveal a tendency toward selenium excess [22].

To more fully characterize the obtained compositions at room temperature, key kinetic parameters of the $Gd_xSn_{1-x}Se$ samples were measured: electrical conductivity ($\sigma$), Hall coefficient ($R$), thermoelectric power ($S$), and thermal conductivity ($k$). Based on these, charge carrier concentration ($p(n)$) and Hall mobility ($\mu$) were calculated; the results are presented in the table below.

***Table.*** *Main kinetic parameters of $Gd_xSn_{1-x}Se$ system alloys at T = 300K*

| Sample compo-sition | σ $om^{-1}sm^{-1}$ | R $sm^3/Kl$ | S Vt/K | $10^{-3}\cdot$ k Vt/sm · K | μ $sm^2/V\cdot s$ | p(n) $sm^{-3}$ |
|---|---|---|---|---|---|---|
| x=0,0 | 76 | 2,105 | 405 | 18,7 | 160 | $3\cdot 10^{18}$ |
| x=0,0025 | 26 | 4,63 | 150 | 17, 36 | 120 | $8.2\cdot 10^{17}$ |
| x=0,005 | 5,43 | 9,88 | 297 | 16,21 | 54 | $6.3\cdot 10^{17}$ |
| x=0,01 | 4,32 | -11, 14 | -215 | 15,42 | 48 | $5.6\cdot 10^{17}$ |
| x=0,03 | 3,28 | -13,42 | -320 | 14,97 | 44 | $5\cdot 10^{17}$ |

As seen from the table, with increasing $Gd$ content, charge carrier concentration and their mobility sharply decrease. This is related to a change in the nature of the chemical bond: substitution of $Sn^{2+}$ ions by $Gd^{3+}$ strengthens the ionic component of the bond and reduces its directionality [23]. The additional positive charge of $Gd^{3+}$ requires compensation, which may occur through the formation of point defects (e.g., selenium vacancies) that act as traps for carriers and reduce hole concentration. Additionally, $Gd^{3+}$ can act as a donor, causing a transition from p-type to n-type conductivity or compensation thereof [24].

Differences in size and charge between $Sn^{2+}$ and $Gd^{3+}$ lead to local lattice distortions and enhanced carrier scattering, reducing their mobility. Formation of additional defects and clusters that intensify this scattering is also possible. Moreover, the reduction in thermal conductivity is due to phonon scattering on emerging structural disruptions and alloy disorder [25].

The temperature dependence of thermoelectric power in $Gd_xSn_{1-x}Se$ solid solutions is shown in Fig. 3. Its behavior is related to electronic structure features and carrier transport mechanisms. Upon gadolinium addition to $p-SnSe$, both the magnitude and sign of thermoelectric power change [26].

In the sample with $x = 0.0025$, $S(T)$ increases from 60 to $250\ \mu V/K$ in the range $100-450\ K$, then decreases. This is associated with an increase in thermally excited carrier concentration and subsequent generation of electron-hole pairs compensating the thermoelectric contribution. At $Gd$ content $\geq 0.005\ at.\%$, a conductivity type change is observed. For the $x = 0.005$ sample at $T = 420\ K$, the sign of $S$ inverts from positive to negative, indicating a transition from $p-$ to $n-$type conduction. In samples with $x > 0.005$, this transition occurs at higher temperatures (e.g., $T = 500\ K$ for $x = 0.03$).

In all solid solutions, thermoelectric power first increases and then decreases with temperature, explained by a two-band model with light and heavy holes. Hall coefficients and thermoelectric power correlate well, confirming the complexity of the band structure [27]. Thermoelectric power in pure $SnSe$ is higher in all temperature ranges than in doped samples. Substitution of $Sn$ with rare-earth elements reduces S and shifts the region of its decrease toward higher temperatures.

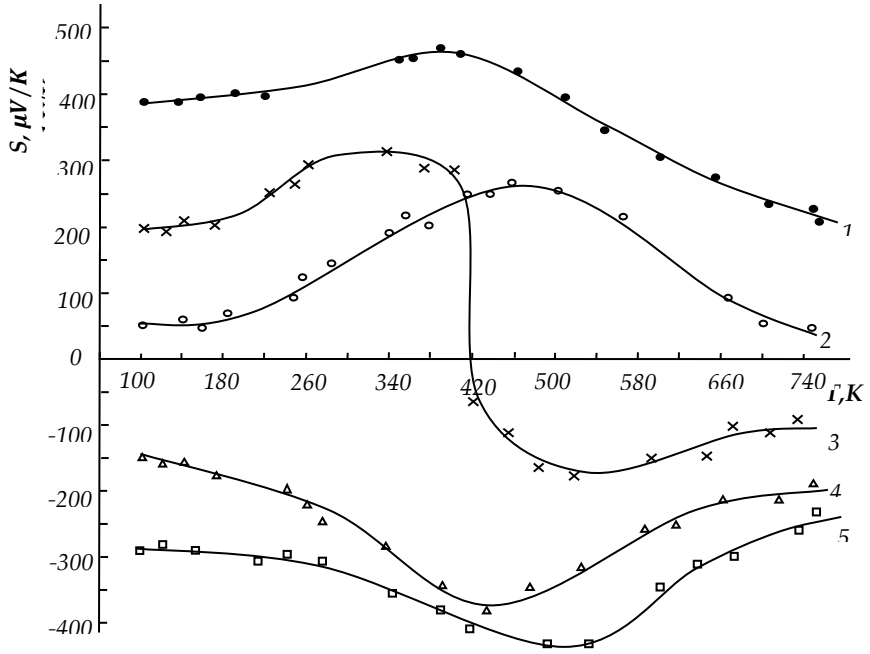


***Figure 3.*** *Temperature dependence of thermo-EMF in system $Gd_xSn_{1-x}Se$ crystals:1-x =0; 2-x=0.0025; 3-0.005 4-x=0.01; 5-x=0.03*

Fig. 4 shows the temperature dependence of the Nernst–Ettingshausen transverse effect coefficient $(E_y)$ for $Gd_xSn_{1-x}Se$ alloys with different gadolinium contents: $x = 0$ (sample No.1), 0.0025 (No.2), and 0.01 (No.4). In pure $SnSe$ (curve 1) in the range $100–450\ K$, $E_y$ rises from 5.8% to 9%, then gradually decreases at $460–740\ K$ but remains positive. This behavior is associated with an increase in carrier concentration and mobility upon heating, followed by enhanced scattering [28].

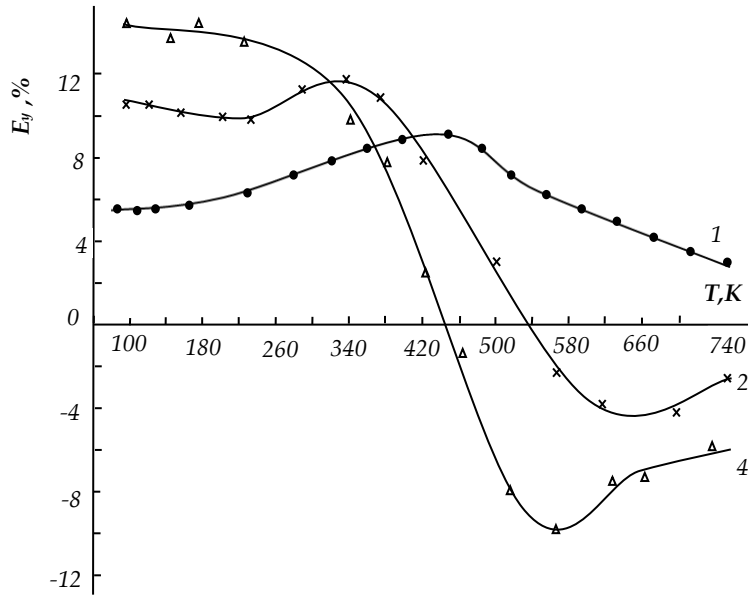


***Figure 4.*** *Temperature dependence of the transverse N-E effect in some compositions of $Gd_xSn_{1-x}Se$ crystals: 1-x=0.0; 2 - x = 0.0025; 4 - x = 0.01*

In doped alloys, the character of $E_y$ dependence changes. In sample No.2 with $x = 0.0025$, a maximum is observed near $380\ K$, after which the coefficient decreases and changes sign to negative at $540\ K$, indicating a change in the dominant carrier type. This is related to the activation of heavy holes and influence of local levels introduced by $Gd^{3+}$.

For sample No.4 ($x = 0.01$), the effect becomes negative already at $430\ K$, with a maximum (in absolute value) around $550–560\ K$. With increasing $Gd$ content, the inversion temperature shifts to higher values. This is explained by the donor nature of $Gd^{3+}$ and Fermi level shift, leading to an earlier disruption of electron-hole balance.

Fig. 5 presents the dependencies of thermoelectric power change ($\Delta S(H)$) on magnetic field for $Gd_xSn_{1-x}Se$ alloys at various temperatures. At $95\ K$, a more pronounced growth of $\Delta S(H)$ up to $6\ kOe$ is observed, after which the increase slows. The dependence is nonlinear and does not reach saturation. At $310\ K$, the curve approaches linearity.

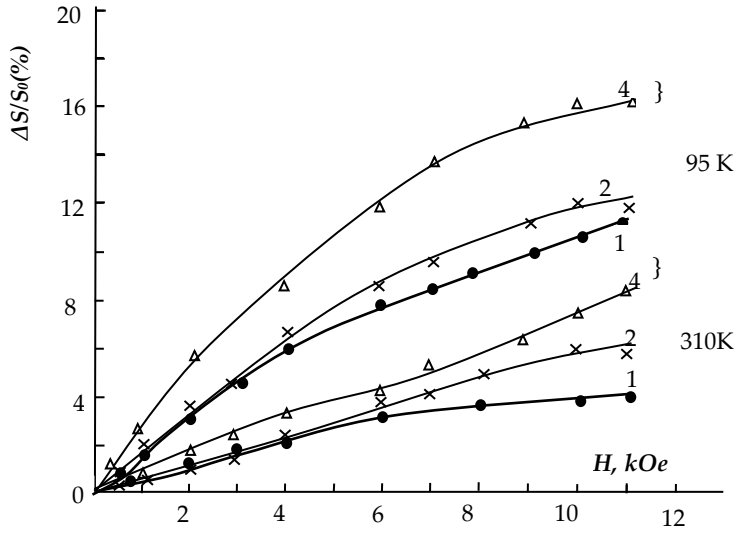


***Figure 5.*** *The dependence of ΔS on the magnetic field(H) in $Gd_xSn_{1-x}Se$ crystals: 1-x=0.0; 2 - x = 0.0025; 4 - x = 0.01*

With increasing gadolinium content, $\Delta S(H)$ increases, indicating enhancement of the longitudinal Nernst–Ettingshausen effect. At low temperatures, weakened thermal vibrations make carriers more sensitive to the magnetic field, and nonlinearity reflects a change in dominant mechanisms. At high temperatures, thermal scattering predominates, reducing magnetic field influence. The more pronounced effect in samples with high Gd content is explained by additional magnetic scattering and the influence of rare-earth ions on the electronic structure.

## 4. CONCLUSION

This work presents the results of synthesis and comprehensive investigation of $Gd_xSn_{1-x}Se$ solid solutions obtained by the direct melting method. It was established that the introduction of $Gd^{3+}$ ions into the $SnSe$ crystal lattice leads to the formation of a substitutional solid solution, accompanied by an increase in lattice parameters, an increase in microhardness, and a decrease in the melting temperature. The studies showed that the addition of $Gd$ significantly affects the electrophysical and thermomagnetic properties of the materials. A decrease in carrier

concentration and mobility was observed, along with an inversion of the sign of the thermoelectric power and the Nernst–Ettingshausen coefficient, as well as an enhancement of the longitudinal N–E effect in a magnetic field. These phenomena are explained by the formation of point defects, a change in the type of conductivity, and enhanced carrier scattering. The obtained results confirm the potential of doping SnSe with rare-earth elements to control its physical properties and to improve its efficiency in thermoelectric and sensor applications.

## REFERENCE


1. Duong D.L. , Yun S.J. , Lee Y.H. (2017) van der Waals Layered Materials: Opportunities and Challenges. ACS Nano , 11 (12), 11803–11830; https://doi.org/10.1021/acsnano.7b07436
2. Kim J., Song O., Cho Y.S., Jung M., Rhee D., Kang J. (2022) Revisiting Solution-Based Processing of van der Waals Layered Materials for Electronics. ACS Materials Au, 2 (4), 382–393; https://doi.org/10.1021/acsmaterialsau.2c00034
3. Stepanov R.S., Marland P.I., Kolobov A.V. (2023) Compositional and Structural Disorder in Two-Dimensional $A^{III}B^{VI}$ Materials. *Crystals, 13 (*8), 1209;
4. https://doi.org/10.3390/cryst13081209
5. Dede D., Morgan N., Gächter N., Nurmamytov T. , Luca M.D. et al. (2022) Low Dimensional III-V and II-VI Semiconductors. Microscopy and Microanalysis, 28 (S1), 2004; http://dx.doi.org/10.1017/s1431927622007784.
6. Buruiana A.-T., Mihai C., Kuncser V., Velea A. (2025) Advances in 2D Group IV Monochalcogenides: Synthesis, Properties, and Applications. *Materials*, *18* (7), 1530; https://doi.org/10.3390/ma18071530
7. Guo S.-D. , Wang Y.-H. (2017) Thermoelectric properties of orthorhombic group IV–VI monolayers from the first-principles calculations. J. Appl. Phys. 121, 034302; https://doi.org/10.1063/1.4974200
8. Ding G. , Gao G. , Yao K. (2015) High-efficient thermoelectric materials: The case of orthorhombic IV-VI compounds. Scientific Reports, 5, 9567; https://doi.org/10.48550/arXiv.1505.02477
9. Isber S., Gratens X. (2010) Crystal growth and magnetic properties of tin selenide-doped europium $Sn_{1-x}Eu_xSe$. Journal of Magnetism and Magnetic Materials. 322, 1113–1116.
10. Wei B., Zhang J., Lin L., Wu T., Cheng Z., Ma Y., Li J., Yu S. (2024) Enhancing Electrical Transport Performance of Polycrystalline Tin Selenide by Doping Different Elements. Physica Status Solidi (A) Applications and Materials. Vol. 221, Is. 9, 2300717; https://doi.org/10.1002/pssa.202300717
11. Yang X., Ma X-Y., Shi T.-E., Bao W-Q., Wang J., et al. (2024) High thermoelectric properties in polycrystalline SnSe materials realized by rare earth halide Co-doping. Ceramics International, Vol. 50 (11), Part B, pp. 20515-20524;
12. https://doi.org/10.1016/j.ceramint.2024.03.173
13. Li S., Yin Li, Liu Y., Wang X., Chen C., Zhang Q. (2023) Rare earth element Ce enables high thermoelectric performance in n-type SnSe polycrystals. Journal of Materials Science & Technology. 143, 234-24120; https://doi.org/10.1016/j.jmst.2022.09.054
14. Askerov B. M. (1994) Electron Transport Phenomena in Semiconductors. World Scientific, Singapore, New Jersey, London, 394 p.
15. Yamada R., Nomoto T., Miyake A., Terakawa T., Kikkawa A., et al. (2024) Nernst Effect of High-Mobility Weyl Electrons in NdAlSi Enhanced by a Fermi Surface Nesting Instability. Physical Review X. 14, 021012; DOI: 10.1103/PhysRevX.14.021012
16. Akhanda S., Schlaak K.A., Scott E.F., Taj N.A., Watzman S. J., Zebarjadi M. (2024) Thermomagnetic responses of semimetals. *J. Appl. Phys.* 135, 240901;
17. https://doi.org/10.1063/5.0192824
18. Huseynov J.I., Murguzov M.I., Ismayilov S.S. (2013) Specificfeatures of self-compensation in $Er_xSn_{1-x}Se$ solid solutions Semiconductors 47, 323–326;
19. https://doi.org/10.1134/S106378261303010X
20. Huseynov J.I., Murguzov M.I., Ismayilov S.S., et al. (2017) On the thermopower and thermomagnetic properties of $Er_xSn_{1-x}Se$ solid solutions. Semiconductors 51, 153–157; https://doi.org/10.1134/S1063782617020075

21. Aliev I.I. , Huseynov J.I. , Murguzov M.I. , Ismailov Sh.S. , Gojaev E.M. (2014) Phase relations and properties of alloys in the SnSe-DySe system. Inorg Mater, 50, 237–240; https://doi.org/10.1134/S0020168514030029
22. Ismailov Sh.S., Huseynov J.I., Musaev M.A., Abbasov I.I., Abdurakhmanova V.A. (2020) Effect of doping level and compensation on thermal conductivity in $Ce_xSn_{1-x}Se$ solid solutions *Low Temp. Phys.* 46, 1114–1120; https://doi.org/10.1063/10.0002155
23. Abbasov I.I., Ismailov Sh.S., Huseynov J.I., Abdurakhmanova V.A. (2019) Concentration dependences of electrical conductivity and the Hall effect of the $Ce_xSn_{1-x}Se$ single crystals. *Low Temp. Phys.* 45, 1277–1280; https://doi.org/10.1063/10.0000209
24. J.I.Hüseynov, Kh.A.Hasanov, T.A.Jafarov, I.I.Abbasov.(2020) Compensating effect of terbium impurity on the conductivity of $Tb_xSn_{1-x}Se$ solid solutions. Ukrainian journal of physics. 65 (3), 225-230; http://jnas.nbuv.gov.ua/article/UJRN-0001127989
25. Jagani H.S., Dixit V., Patel A., Gohil J., Pathak V.M. (2022) Stability & durability of self-driven photo-detective parameters based on $Sn_{1-\beta}Sb_\beta Se$ ($\beta$ = 0, 0.05, 0.10, 0.15, 0.20) ternary alloy single crystals. RSC Adv., 12 (44), 28693-28706; DOI:10.1039/D2RA05492
26. Abbasov I.I., Musayev M.A., Huseynov C.I., Eyyubov Q.Y., Hasimova N.N., Mammadova A.J. (2023). A study of impurity defect photoluminescence in ZnSe: Cr and ZnSe: Fe in the near infrared at room temperature. Advanced Physical Research, 5 (3), 192-199
27. Hu H., Su B., Liu X., Thong H-C., Jiang Y., et al. (2024) Chemical bond engineering toward extraordinary power factor and service stability in thermoelectric copper selenide. Joule, 8, 416–429; doi.org/10.1016/j.joule.2023.12.019
28. Abbasov I.I., Huseynov J.I. (2017) Charge-transfer processes in $(SnS)_{1-x}(PrS)_x$ Alloys. Ukrainian journal of physics. 62 (10), 883-888; http://jnas.nbuv.gov.ua/article/UJRN-0000795750
29. Dhahri R., Benamara M., Bouzidi S., Moussa S.B., Abdullah A.Y., et al. (2025) Effect of Gd doping on the microstructure and electrical characteristics of Maghemite ($\gamma$-$Fe_2O_3$) ceramics. J Sol-Gel Sci Technol. 113, 225–242; https://doi.org/10.1007/s10971-024-06598-0
30. Huseynov D.I., Murguzov M.I., Ismailov S.S. (2008) Thermal conductivity of $Er_xSn_{1-x}Se$ ($x \leq 0.025$) solid solutions. Inorg Mater 44, 467–469;
31. https://doi.org/10.1134/S0020168508050063
32. Hasanov K.A., Huseynov J.I., Dadashova V.V., Aliyev F.F. (2016) Effect of Phonon Drag on the Thermopower in a Parabolic Quantum Well. Semiconductors 50, 295–298 https://doi.org/10.1134/S106378261603009X
33. Hasanov O.M., Huseynov C.I., Aslanov H.A., Adgozalova X.A., Garashova G.A., Bayramli R.B., (2024) Galvanomagnetic properties of $Gd_xSn_{1-x}Se$ solid solutions. Journal of Baku Engineering university – Physics, 8, 2, 81-90, https://doi.org/10.30546/09081.2024.102.7068
34. Huseynov J.I., Jafarov T.A., Hasanov O.M., Adgezalova Kh.A., (2019). Thermoelectric and thermomagnetic properties of the $Tb_xSn_{1-x}Se$ alloy systems. Applied physics 6, 82; https://applphys.orion-ir.ru/appl-19/19-6/PF-19-6-82.pdf

JOURNAL OF BAKU ENGINEERING UNIVERSITY - PHYSICS
*2025. Volume 9, Number 2* *Pages 121-126*

*UDC: 543.429.23:544.344.3:678.7*
*DOI: https://doi.org/10.30546/09081.2025.002.1043*

# NMR SPECTRAL CHARACTERISTICS OF PHASES IN A PEG-DEXTRAN-WATER AQUEOUS TWO-PHASE SYSTEM

**Jala TEYMUROVA**
*Baku State University, Baku, Azerbaijan*
*jalateymurova98@gmail.com*

*ARTICLE INFO*

*Article history:*
*Received:2025-06-16*
*Received in revised form:2025-06-25*
*Accepted:2025-07-21*
*Available online:2025-12-21*

*Keywords:*
*Aqueous polymer two-phase system; Phase separation; Upper phase; Lower phase; $^1H$ NMR*



*ABSTRACT*

*In this study, the properties of the upper and lower phases obtained after phase separation in a PEG (polyethylene glycol)–dextran–water aqueous two-phase system were comparatively investigated using $^1H$ NMR spectroscopy. For comparison, a bi-distilled water sample was used as a reference, and the spectra of the phase samples were recorded under identical measurement conditions. The position and shape of the water signal in the NMR spectra, as well as the appearance of polymer-derived proton signals, enabled the assessment of compositional and structural differences between the phases. The results showed that, although the phases share the same aqueous medium, the spectral patterns differ due to interactions of the polymers with hydrophobic and hydrophilic groups. Thus, $^1H$ NMR is presented as an informative approach for characterization and interpretation of interphase differences in aqueous two-phase systems.*

## 1. INTRODUCTION

As is well known, to study each component of biological mixtures (cells, viruses, proteins, etc.) individually, it is first necessary to separate them from one another. Although numerous chemical methods exist for the separation and purification of biological particle mixtures, these approaches are generally unsuitable for the separation of biological materials [1]. This is because, during the application of such methods, biological objects may undergo denaturation under the influence of various factors, thereby losing their biological activity and original properties. Other potentially applicable methods are complex, labor-intensive, and economically inefficient.

In recent years, the Swedish scientist P. A. Albertsson [2] developed a new method for the separation and purification of biological materials that is simple, cost-effective, does not require large-scale equipment, and is convenient to implement. This method is based on the unequal partitioning of substances in aqueous polymer two-phase systems. The essence of the method is as follows: when two polymers of different chemical nature are dissolved together in water, at polymer concentrations exceeding certain threshold values, the homogeneous solution separates into two immiscible liquid phases that are in equilibrium and possess different physicochemical properties (primarily due to hydrophobic and hydrophilic interactions); that is, a homogeneous-to-heterogeneous phase transition occurs. In such an equilibrium system, one phase becomes enriched with one component, while the other is enriched with the second component. Both phases consist predominantly of water (70–90%), which is the natural environment of living organisms [3]. The physicochemical properties of the phases differ, and consequently, the affinities of solutes distributed in an aqueous polymer system toward the phases are not the

same. Therefore, substances partition unevenly between the phases. Because water constitutes the major component of both phases, the structure of biomaterials is not damaged during partitioning, and thus their biological functions remain unchanged. One of the key advantages of this method is that the partitioning process can be readily transferred from laboratory conditions to biotechnological and industrial-scale applications.

It should be specifically noted that this modified method also has broad application potential in medical, biological, and pharmacological fields. In particular, it has helped to overcome the long-standing simplistic view of the key concepts of hydrophilicity, hydrophobicity, the hydrophobic effect, and hydrophobic interactions, and it enables the quantitative assessment of the relative hydrophobicity of substances, which cannot be determined by other methods [4]. Furthermore, this approach is widely used in primary medical diagnostics and facilitates understanding of the reasons underlying the existence of numerous energetic (histo-hematic) barriers in living organisms.

Thus, the search for, identification of, and recommendation of aqueous two-phase systems (ATPS) applicable to specific practical cases is highly relevant. To experimentally investigate phase separation in such systems, one of the simplest and most accessible model systems is an aqueous polymer system. In the present work, a PEG–dextran–water aqueous two-phase system was selected as the object of study. As noted above, phase separation in this system occurs when the concentrations of both polymers (PEG and dextran) exceed certain threshold values, leading to the formation of two distinct phases in water. One phase is dextran-rich, whereas the other is PEG-rich. Water constitutes the major fraction of both phases (approximately 70–90%). The structural temperature of each phase was determined by the viscometric method, and it was confirmed that the PEG-rich phase is more structured than the dextran-rich phase [5]. The obtained results indicate that the upper and lower phases differ in terms of the level of aqueous polymer structuring.

Phase separation can be qualitatively explained as follows. The polymers introduced into water differ in their chemical composition. This difference is associated with variations in the hydrophobic and hydrophilic groups present in each polymer. Naturally, such diversity should manifest itself in the interactions between the polymers and water. For this reason, when polymers are added to water, their distinct hydrophobic and hydrophilic groups affect the hydrogen-bond network in different ways—weakening or strengthening hydrogen bonding to varying extents. Consequently, as the distribution of electron density responsible for hydrogen-bond formation changes, water molecules become oriented differently, and characteristic microdomains are formed in the immediate vicinity of each polymer [6]. As a result, these processes occurring throughout the bulk lead to the formation of nuclei (incipient domains) of the emerging phases (Figure 1).

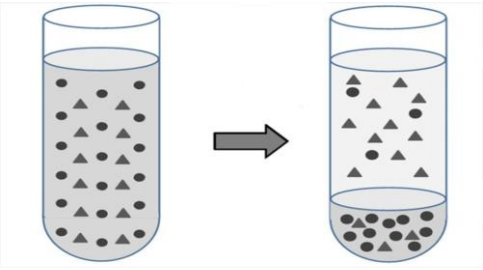

***Fig. 1*** *Schematic representation of the phase-separation process*

When the size (r) and concentration (C) of these newly formed structures are small, they are disrupted by thermal motion. This process is fluctuation-driven: over time, new structures continuously form and disappear, and they remain thermodynamically unstable. As the polymer concentrations are gradually increased, the microdomains grow through fluctuation-induced coalescence, and both their size and concentration increase. Once the size and concentration exceed certain critical values, i.e., when $r > r_{cr}$ and $C > C_{cr}$, thermodynamically stable, mutually immiscible phases are formed in accordance with the specific polymer–water interactions.

To describe aqueous polymer two-phase systems, unlike conventional phase diagrams, a phase diagram is used in which the coordinates represent the concentrations (in weight %) of the polymer components constituting the phases. The phase diagram is characterized by a number of parameters, including the binodal curve, tie-line, critical point, and the slope of the tie-line [7].

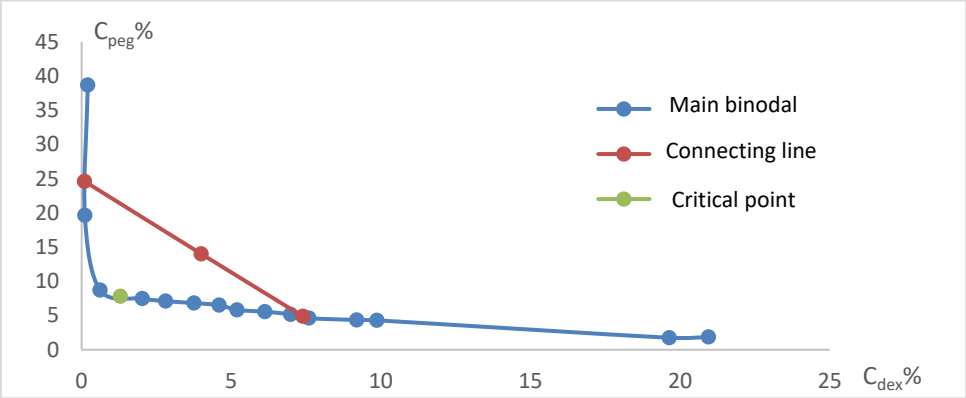


***Fig. 2*** *Phase diagram of the PEG-dextran-water biphasic system*

The concentrations of the components in aqueous solutions at which two-phase systems separate into two distinct phases are determined using binodal curves. The binodal curve represents the locus of points on the phase diagram that separates the single-phase (homogeneous) region from the two-phase (heterogeneous) region for a given system. Another characteristic parameter of two-phase systems is the tie-line. A tie-line indicates the compositions of the upper and lower phases: specifically, the intersections of the tie-line with the binodal, as well as any point along the line, correspond to the component concentrations in the coexisting upper and lower phases. The critical point is a hypothetical point at which the phase volumes and compositions are equal.

## 2. RESULTS AND DISCUSSION

In the present work, to more clearly observe differences in the structure of the aqueous media of the phases in an aqueous polymer two-phase system (ATPS), and considering that both phases are water-rich (70–90%), the nuclear magnetic resonance spectra of pure water and of the aqueous media of the phases were investigated. The experiments were performed on a Spinsolve instrument operating at a working frequency of 60 MHz ($\omega_0 = \gamma H$). Based on the obtained results, the origins of the differences observed between the phases were interpreted, and the applicability of the NMR method for the characterization of two-phase systems was demonstrated.

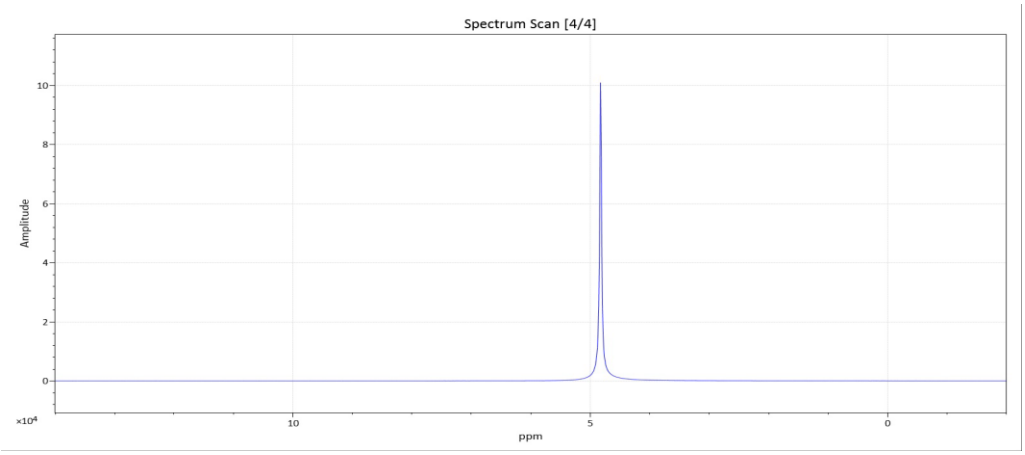


***Fig. 3*** *$^1$H NMR spectrum of distilled water*

Figure 3 shows the NMR spectrum of bi-distilled pure water. As can be seen, the spectrum obtained for the bi-distilled water sample exhibits a single, high-intensity, narrow peak in the range of 4.7–5.0 ppm. This peak corresponds to the protons of free water molecules. The narrow and symmetric peak shape indicates high mobility of water molecules. The absence of additional proton signals confirms that no impurities are present and that the water is pure. This spectrum was taken as the reference for comparison with the other samples (the phase spectra).

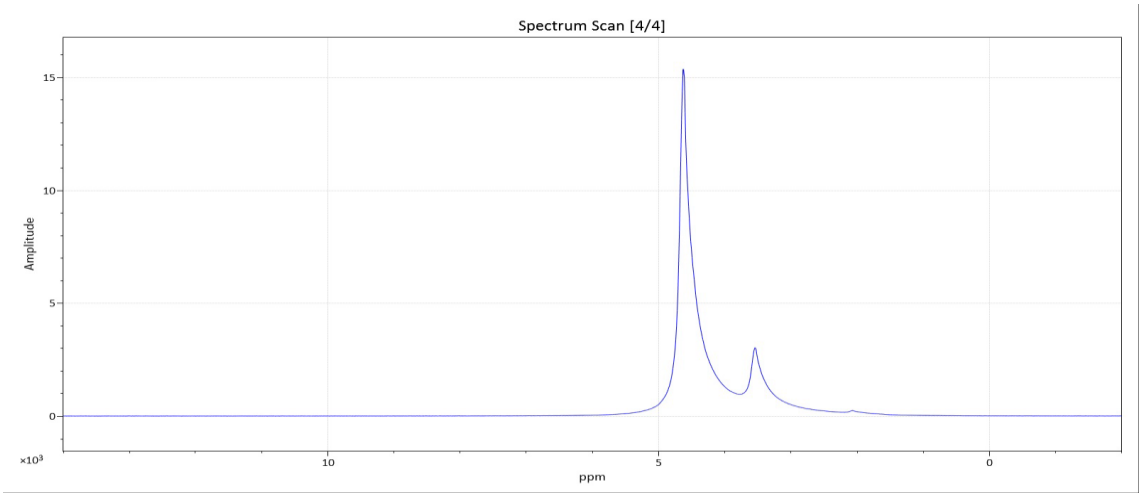


***Fig. 4*** *$^1$H NMR spectrum of the upper phase*

The spectrum of the upper phase is shown in the sample presented in Figure 4. In this spectrum, the main dominant signal (peak) again corresponds to water protons. However, in comparison with bi-distilled water, asymmetry and broadening of the water peak are observed. In addition, extra signals appear in the range of 3.5–3.8 ppm. The additional signal observed at 3.5–3.8 ppm is attributed to the $–CH_2–CH_2–O–$ groups of PEG, since it is generated by PEG protons. On the other hand, the oxygen atoms of PEG form hydrogen bonds with water molecules, rendering a fraction of the water "bound." This interaction alters the electronic environment of water protons and leads to changes in the chemical shift and line shape of the water peak. This indicates that the upper phase is PEG-rich.

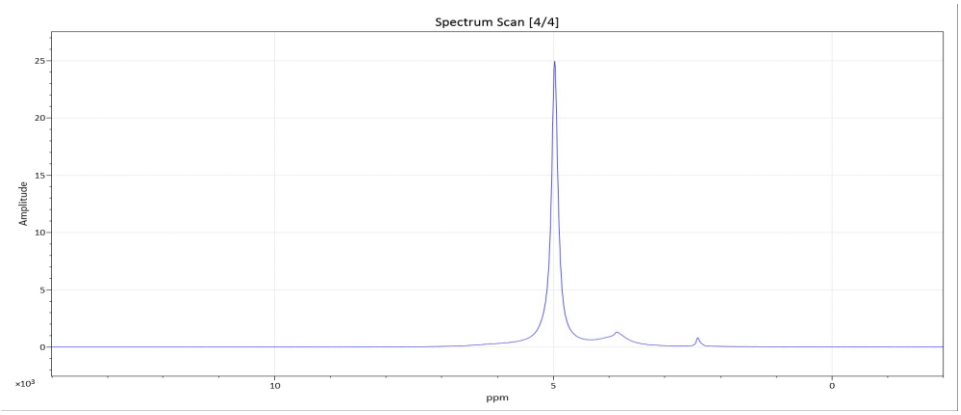


***Fig. 5*** *$^1$H NMR spectrum of the lower phase*

As can be seen from Figure 5, the water peak remains the dominant signal in the spectrum of the lower phase; however, the following additional features are observed:

1. A more complex structure is observed in the vicinity of the water peak

2. Several weak but discernible signals appear in the 3.0–4.5 ppm region

3. Additional weak signals are also observed in the 2.0–2.5 ppm region

The signals observed in the 2.0–2.5 ppm range are attributed to protons located in a modified magnetic environment resulting from the strong interaction of dextran molecules with water. The signals in the 3.0–4.5 ppm region are associated with ring protons of the carbohydrate rings of dextran. In addition, weak signals corresponding to the anomeric protons of dextran are likely present in the ~5.0–5.4 ppm interval (near the water peak). Because a fraction of the anomeric protons participates in bonding, their corresponding signal becomes weakened. Therefore, it is entirely expected that this signal appears not as a distinct, separate peak, but adjacent to and partially overlapping with the water peak. These findings indicate that the lower phase is dextran-rich.

## 3. CONCLUSION

Thus, the performed $^1$H NMR study demonstrated that the upper and lower phases in the PEG–dextran–water aqueous two-phase system differ in their spectral features. Comparison with the bi-distilled water reference revealed changes in the line shape of the water signal and in the overall spectral background in the phase samples, indicating a reorganization of the water microstructure within the polymer environment. The intensity and spectral regions of polymer-derived proton signals in the upper and lower phases confirmed that the phases differ in composition. In particular, the more pronounced signals attributed to ring protons in environments more strongly associated with dextran highlight the role of polymer–water interactions. The results suggest that the differences between the phases are not limited to concentration variations, but also involve changes in hydration and in the state of the hydrogen-bond network. In this respect, $^1$H NMR spectroscopy can be recommended as an effective method for the rapid assessment of phase composition and structural differences in the aqueous medium in ATPS.

**REFERENCE LIST**

1. Masson, P. (2022). Conformational Stability and Denaturation Processes of Proteins. Molecules, 27(20), 6861. https://doi.org/10.3390/molecules27206861
2. Albertsson, P.-Å. (1970). Partition of cell particles and macromolecules in polymer two-phase systems. Advances in Protein Chemistry, 24, 309-341. https://doi.org/10.1016/S0065-3233(08)60244-2
3. Iqbal, M., Tao, Y., Xie, S., et al. (2016). Aqueous two-phase system (ATPS): an overview and advances in its applications. Biological Procedures Online, 18(1), 18. https://doi.org/10.1186/s12575-016-0048-8
4. Zaslavsky, B. Y., & Masimov, E. A. (1988). Methods of analysis of the relative hydrophobicity of biological solutes. Progress in Clinical and Biological Research, 268A, 117-124. https://doi.org/10.1007/BFb0111257
5. Şükürova, J. Z. (2023). PEQ-su və dekstran-su məhlullarının struktur temperaturları. PDF: https://gdu.edu.az/wp-content/uploads/2023/06/Konfrans_2023_5.pdf
6. Titus, A. R., et al. (2022). Mechanism of Phase Separation in Aqueous Two-Phase Systems. International Journal of Molecular Sciences, 23(22), 14366. https://doi.org/10.3390/ijms232214366
7. Zhang, X., et al. (2025). Aqueous two-phase system (ATPS): from basic science to applications. RSC Advances, 15. https://doi.org/10.1039/D4RA08232J

JOURNAL OF BAKU ENGINEERING UNIVERSITY - PHYSICS
*2025. Volume 9, Number 2* *Pages 127-132*

*UDC: 621.315. 592*
*DOI: https://doi.org/10.30546/09081.2025.002.1051*

# THE İNFLUENCE OF BORON ATOMS ON THE ABSORPTİON AND LUMİNESCENCE SPECTRA OF THİN GaSe, InSe FILMS AND GaSe/InSe HETEROSTRUCTURES

**Kh.T. HASANVOA[1], S.R.BAGIROVA**
*İnstitute for Physics Problem*
*Baku State University*
*xaverhasanova2019@rambler.ru , sbagirova2019@gmail.com*

**V.I. HAJIYEVA[3] , A.H. SULTANOVA[4]**
*Nakhchivan State University*
*validehaciyeva@ndu.edu.az, aygunsultanova@ndu.edu.az*

*ARTICLE INFO*

*Article history:*
*Received:2025-06-03*
*Received in revised form:2025-06-14*
*Accepted:2025-07-18*
*Available online:2025-12-21*

*Keywords:*
*GaSe, InSe, laser, absorption, luminescence.*


*ABSTRACT*

*The absorption and luminescence spectra of thin GaSe, InSe films doped with boron atoms and heterostructures based on them were experimentally studied. The studied samples were obtained by a modified chemical vapor deposition method (SILAR). The absorption and luminescence spectra were recorded using a Nd:YAG laser with built-in 2nd and 3rd harmonic generators. It was shown that boron impurities affect the exciton absorption band and the width of the photoluminescence spectral lines.*

## I. INTRODUCTION

Gallium selenide (GaSe) and indium selenide (InSe) crystals belong to layered semiconductor compounds of the $A^3B^6$ type, in which there is a strong ionic-covalent bond along the layers, while weak Van der Waals bonding occurs between the layers. Weak bonding between the layers leads to the formation of tetralayers with thicknesses of ~ 63 nm for GaSe, and the relative arrangement of monolayers in tetralayers forms β-, ε-, γ- and δ- modifications of the crystalline structure [1]. The displacement of tetralayers relative to each other leads in turn to the formation of stacking faults. Experiments show that such defects are distributed randomly in the direction perpendicular to the crystal axis and cause the formation of potential barriers with an average height of $\Delta E \approx 20$ meV for charge carriers in the direction of the [2]. axis. The InSe compound has similar packing defects in the crystal structure. Low hardness and tendency to micro-deltatation of layered GaSe and InSe crystals make them practically unsuitable for mechanical treatment of the working surfaces of samples at an angle to the axis and lead to an increase in optical losses in the crystal. The formed point and linear defects in the crystal structure, due to uncontrollable factors in the process of growing single crystals, do not allow wide application of layered crystals with the required characteristics. To solve this problem, they resort to improving the technology of growing single crystals and doping the crystal with isovalent elements with respect to Ga, In and Se, as well as various rare earth elements [3-6]. In this work, boron was chosen as the doping

element. An isolated boron atom has an unstable configuration of valence electrons $s^2p^1$. However, during the formation of a condensed state, this configuration is transformed into an energetically more stable configuration $s^1p^2$ due to the single-electron transition $s^2p^1 \rightarrow s^1p^2$. For the latter, in turn, transitions according to the scheme $s^1p^2 + s^1p^2 \rightarrow s^1p^3 + s^1p^1$ are possible [7]. Therefore, the boron impurity in multicomponent compounds behaves in a variety of ways. For example, boron atoms implanted in n-type GaAs create deep impurity centers in the forbidden zone of the crystal at a depth of 0.55 and 0.70 eV. In this study, we examined CdSe thin films created on glass substrates using the chemical deposition method and analyzed them using spectroscopic ellipsometry. We used a dispersion model to calculate the optical constants and determine the thickness, dielectric permittivity (real and imaginary part), refraction, and extension coefficients of the thin layers. We found that the width of the forbidden zone in the 350 nm and 400 nm thick cadmium selenide thin films corresponds to Eg = 1.9 eV and Eg = 2.2 eV. The widening of the forbidden zone is attributed to the phase formation process within the thin layers. [8]. After thermal annealing, these centers disappear, turning into a compensating acceptor center. When boron atoms condense in interaction with selenium atoms, an isotypic structure (BSe2) is formed with an optimal distance of 198 nm between B–Se atoms [9]. In the crystal structure of gallium selenide, the distance between Ga–Se and In–Se atoms is 247 nm. Of course, when replacing gallium and indium with impurity boron atoms in the crystal structure of GaSe and InSe, a stronger bond with selenium atoms arises than the Ga-Se and In-Se bond. Therefore, it can be expected that doping GaSe and InSe with boron atoms can eliminate the above-mentioned disadvantages and improve the sought-after practical characteristics of these crystals.

Of particular interest is the study of the effect of boron atoms on epitaxial GaSe/InSe heterostructures, since semiconductor structures with a variable band gap are widely used in the manufacture of optoelectronic devices [10].

In this paper, the absorption and luminescence spectra of thin GaSe, InSe films and GaSe/InSe heterostructures doped with boron atoms under the action of laser radiation are experimentally studied.

## II. EXPERIMENTAL METHODOLOGY

The studied samples were obtained by a modified chemical deposition method (Successive Ionic Layer Adsorption and Reaction- SILAR). Thin films of GaSe and InSe on a glass substrate were grown by hydrochemical deposition from a solution containing sodium selenosulfate ( $Na_2SeSO_3$ ) and gallium trichloride ( $GaCl_3$ ) and indium ($InCl_3$). The initial raw materials used were especially pure $Na_2SeSO_3$ and $GaCl_3$ according to the following reactions:

$$Na_2SO_3 + Se \rightarrow Na_2SeSO_3$$

$$In + 3HCl \leftrightarrow GaCl_2 + \frac{3}{2}H_2$$

$$Ga + 3HCl \leftrightarrow GaCl_2 + \frac{3}{2}H_2$$

Then, aqueous solutions of sodium selenosulfate and gallium chloride were prepared in the ratio necessary for the formation of and InSe, with a composition corresponding to the stoichiometric

composition. Thin films of the compound and InSe were grown in the following sequence: four containers with liquids were used. The first contained a solution of gallium or indium chloride, the second distilled water, the third a solution of sodium selenosulfate and the fourth, also distilled water. The substrates were kept in these containers successively for 20 seconds, 10 seconds, 15 seconds and 10 seconds, respectively. This process was repeated 30 times in a row.

A pulsed Nd:YAG laser with built-in 2nd and 3rd harmonic generators designed to generate radiation with wavelengths of 1064, 532 and 335 nm was used as a radiation source. The laser pulse duration was 10 ns with a maximum power of ~12 MVt/cm2. The radiation intensity was varied using calibrated neutral light filters. Using a lens, the laser beam was focused onto the sample surface with a spot diameter of ~2.0 mm. The absorption and photoluminescence spectra were studied using an automated M833 double dispersion monochromator with computer control and a photodetector recording radiation in the wavelength range of 350-2000 nm. The experimental technique is similar to that presented in. Thus, as the bond lengths of the same chemical elements decrease, the frequency of vibrations increases. Therefore, in studies carried out at high pressures, an increase in the vibration frequency is observed as the crystal lattice is destroyed [11].

## III. EXPERIMENTAL RESULTS AND THEIR DISCUSSION

Figure 1a (curve 1) shows the absorption spectrum of thin GaSe films without boron doping. As can be seen from the figure, the sharp peak corresponds to the energy Eexp~2.077 eV. In our opinion, this peak is associated with free excitons, since it is known that the fundamental edge of the GaSe absorption band is due to free exciton transitions with an exciton binding energy of ~20 meV [12]. The width of the GaSe band gap, determined from the dependence $\alpha^2 \sim f(h\nu)$, turned out to be equal to $E_g = 2{,}097$ eV.

The absorption spectrum of thin GaSe films doped with boron atoms (0.1 V) differs significantly from the absorption spectrum of pure samples (Fig. 1, a, curve 2). In the absorption spectrum of doped samples, a decrease in exciton absorption and a shift of the absorption band edge to the long-wave region of the spectrum (~5 nm) are observed. The band gap of boron-doped GaSe samples was found to be ~2.073 eV.

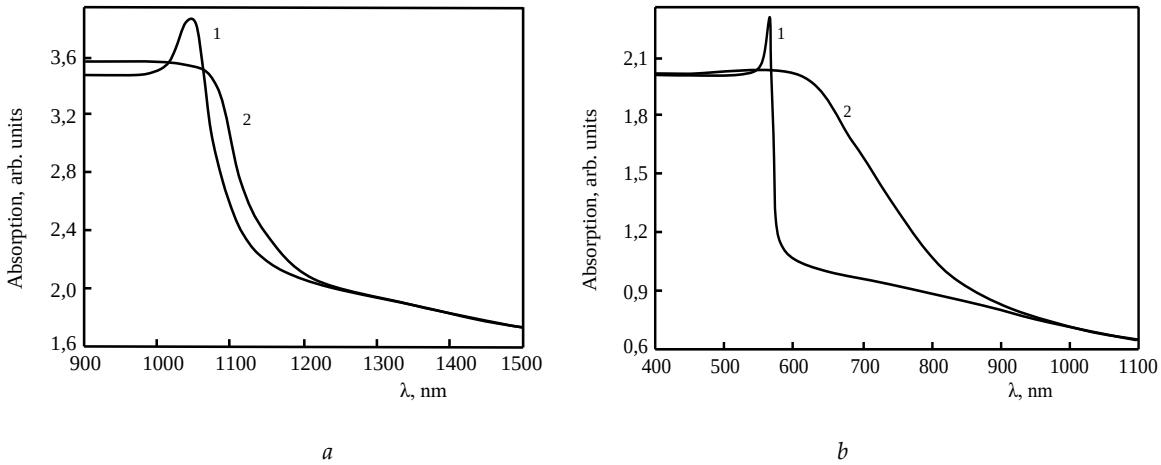


***Fig. 1.*** *Absorption spectra of GaSe (a) and InSe (b): 1 – pure; 2 – doped with boron atoms.*

Similar patterns are observed for InSe thin films. Unlike GaSe, the absorption spectra of InSe thin films are in the near infrared region of the spectrum. In samples undoped with boron atoms, exciton absorption corresponds to the energy Eexp~1.14 eV, and the band gap is 1.16 eV. The shift of the absorption band edge to the long-wavelength region of the spectrum in doped samples is ~9 nm. Fig. 2 shows the absorption spectra of the GaSe/InSe heterostructure of pure (black line) and boron-doped (red line) components. As can be seen from the figure, three absorption bands are observed in the absorption spectrum of pure GaSe/InSe at 597 nm, 465 nm and 485 nm.

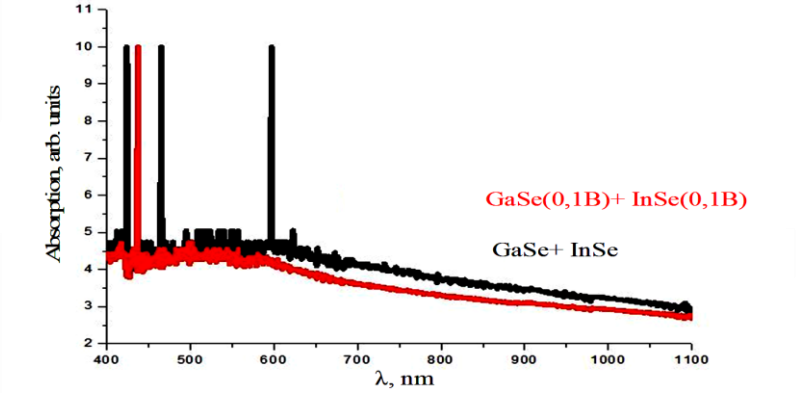


***Fig. 2.*** *Absorption spectra of the GaSe/InSe heterostructure, pure (black line) and doped (red line) with boron atoms.*

In our opinion, the absorption band in thin GaSe films with a maximum at $\lambda$=597 nm is related to exciton absorption at the edge of intrinsic absorption. Two other high-energy bands, at 465 nm and 485 nm, are apparently due to interband transitions in the region of the continuous spectrum of InSe. Referring to the data in, we can say that the features in the absorption spectrum of InSe that we observed are related to hyperbolic excitons and impurities located in the region of the continuous spectrum. The chemical deposition process was carried out at room temperature (27 $^{o}$C) for 48 hours without rotation.During the process, a white precipitate formed at the bottom of the glass. After three to four hours, this precipitate andthe clear solution in the beaker first turned dark yellow and then red, consistent with CdSe. After this procedure, thesaucer was removed from the glass, washed with distilled water and dried [14] However, the absorption line at $\lambda$=475 nm observed in the GaSe(0.1B)-InSe(0.1B) heterostructures is apparently related to boron impurities. As experiments show, in GaSe/InSe structures doped with boron atoms, only one absorption band with a maximum at $\lambda$=475 nm is observed (Fig. 2b). The fact that the band of this line is absent in the absorption spectrum of pure GaSe/InSe structures apparently indicates that this line is associated with boron atoms.

Fig. 3a (curve 1) shows the photoluminescence spectrum of a thin GaSe film without boron doping upon excitation by the second harmonic of a Nd:YAG laser ($\lambda$=532 nm). As can be seen from the figure, the maximum emission corresponds to a wavelength of ~597 nm. The half-width of the emission line, which is only ~5-8 A$^{0}$, is noteworthy. Comparison of the emission line with the absorption spectra allows us to state that the observed recombination emission is also caused by exciton transitions at the edge of intrinsic absorption. Based on the experimental data obtained, it can be assumed that a number of changes in the photoelectric parameters of photodiodes when irradiated with high-energy particles are apparently associated with a specific feature of the crystal structure of layered materials, i.e. interaction of radiation defects arising in

crystalline layers and interlayer spaces. [15] It should be noted that the high emission intensity and its narrowness, several angstroms in size, allow us to state that thin GaSe films can be used as an active element for creating a semiconductor quantum generator on their basis.

Unlike undoped samples, in doped thin GaSe films, as in the case of absorption spectra, the emission spectra shift toward longer waves, and the line half-width increases by a factor of ~10 and is ~80 Å$^0$ (Fig. 3, a, curve 2). In our opinion, the increase in the half-width is due to boron impurities, which create shallow donor levels near the conduction band.

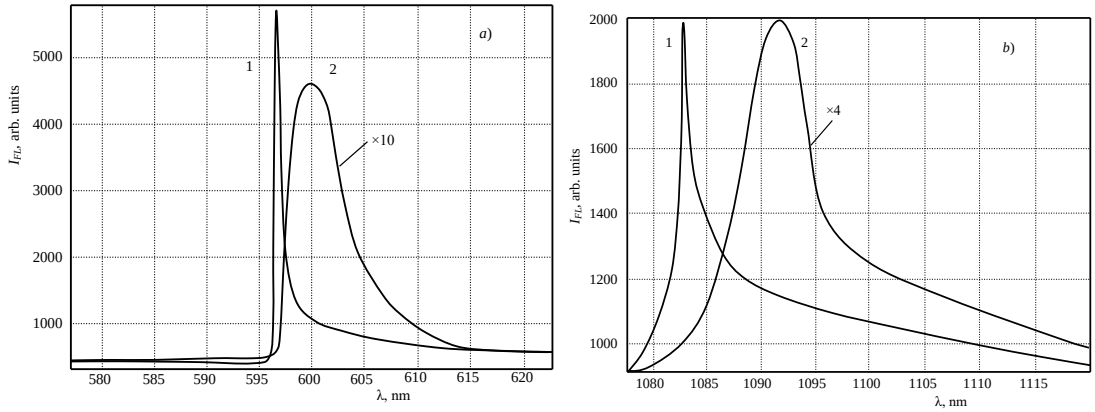


***Fig. 3.*** *Luminescence spectra of pure thin films of GaSe (a) and InSe (b): 1 – pure; 2 – doped with boron atoms.*

Similar features are observed in the luminescence spectra of InSe thin films (Fig. 3, b). The maximum emission corresponds, to the near IR region of the spectrum and is equal to 1083 nm. The half-width of the emission line is ~10 Å$^0$. When doped with boron atoms, as in the case of GaSe, the half-width of the line increases and is equal to ~50 Å$^0$.

## IV. CONCLUSION

Thin GaSe, InSe films and GaSe/InSe heterostructures with and without boron doping were fabricated by chemical vapor deposition. The absorption and photoluminescence spectra of the materials were studied using a pulsed Nd:YAG laser. It was found that the presence of boron impurities not only affects the absorption band edge of GaSe and InSe thin films, but also leads to the disappearance of the exciton absorption of the GaSe/InSe heterostructure associated with hyperbolic excitons in the continuous spectrum region. Common to all luminescence spectra of GaSe, InSe thin films is that boron impurities lead to a broadening of the emission band.

**LITERATURE**

[1]. Rybkovskiy, D. V., Osadchy, A. V., & Obraztsova, E. D. Transition from parabolic to ring-shaped valence band maximum in few-layer GaS, GaSe, and InSe. (2014). Physical Review B, 90(23).

[2]. VM Salmanov, AG Guseinov, MA Dzhafarov, RM Mamedov, F Sh Akhmedova, TA Mamedova. Preparation of Gallium Selenide Nanoparticles by Laser Ablation in Liquid. Russian Journal of Physical Chemistry A (2024), 98(3), p479-483

[3]. Guo, J., Xie, J.-J., Li, D.-J., Yang, G.-L., Chen, F., Wang, C.-R., ... Svetlichnyi, V. A. Doped GaSe crystals for laser frequency conversion. Light: Science & Applications, (2015), 4(12), e362–e362.

[4]. Zhang, Y.-F., Wang, R., Kang, Z.-H., Qu, L.-L., Jiang, Y., Gao, J.-Y., ... Zuev, V. V. AgGaS2- and Al-doped GaSe Crystals for IR Applications. Optics Communications, (2011), 284(6), 1677–1681.

[5]. Yu-Kuei Hsu, Chen-Shiung Chang and Wen-Chang Huang. Electrical properties of GaSe doped with Er. J. Appl. Phys. 2004, 96, 1563.

[6]. Evdoteev I. Impurity states and defects in layered semiconductors GaSe and InSe. Abstract of Cand. Diss. 2010, 32 p.

[7]. Tutelyan V.A., Knazhev V.A., Khotimchenko S.A., et al. (Eds) Selen v organizme cheloveka: metabolism, antioksidantnyye svoystva, rol' v kantserogeneze (Selenium in the Human Organism: Metabolism, Anti-Oxidant Properties, Role in Carcinogenesis) (Moscow: Izd-vo RAMN, 2002)

[8]. L.N.İbrahimova, Kh.N.Ahmadova, M.E.Aliyev Study of CdSe thin films using the spectroscopic ellipsometry method. Chalcogenide Letters. Volume 21, Number 12, December 2024 DOI: 10.15251/CL.2024.2112.1035

[9]. D. V. Rybkovskiy, A. V. Osadchy, and E. D. Obraztsova, J. Nanoelectron. Optoelectron. **8**, 110 (2013).

[10]. A. Pashayev, B. Tunaboylu, K. Allahverdiyev, et al., Proc. SPIE **9810**, 981017 (2015).

[11]. N.M. Abdullayev, L.N. Ibrahimova, M.E. Aliyev, Y.I. Aliyev Investigation of the atomic dynamics of cdse thin layers by raman spectroscopy Chemical problems 2024 no. 2 (22) ISSN 2221-8688. DOI: 10.32737/2221-8688-2024-2-231-236

[12]. V.M. Salmanov, A.G. Guseynov, R.M. Mamedov, A.A. Salmanova, N.D. Dashdamirova. Optics and Spectroscopy, 2020, v. 128, v.4, p. 513-516.

[13]. Kozhemyakin, G.N., Belov, Yu.S., Loginov, B.M., Parashchenko, A.N., and Romanenko, S.S., Microstructure peculiarities of the extruded crystals of bismuth and antimony chalcogenides, Fiz. Khim. Obrab. Mater., 2017, no. 4, pp. 67–73.

[14]. Ibrahimova, L., Abdullayev, N., Aliyev, M., Garashova, G., & Aliyev, Y. (2024). Phase Formation Process in CdSe Thin Films. *East European Journal of Physics*, (1), 493-496. https://doi.org/10.26565/2312-4334-2024-1-54

[15]. Valida Ibrahim Haciyeva, Shirzad Zulfugar Babayev. İnfluence of gamma,electron,proton and gamma neytron irradiation on photodiodes based on inse with improved parametres.Chemical problems 2025 no 2(23) ISSN2221-8688, 266-272 DOI: 10.32737/2221-8688-2025-2-266-271

# INSTRUCTIONS FOR AUTHORS

1. "The Baku Engineering University Journal-Physics" accepts original unpublished articles and reviews in the research field of the author.
2. Articles are accepted in English.
3. File format should be compatible with **Microsoft Word** and must be sent to the electronic mail (**journal@beu.edu.az**) of the Journal. The submitted article should follow the following format:

- Article title, author's name and surname
- The name of workplace
- Mail address
- Abstract and key words

4. The title of the article should be in each of the three languages of the abstract and should be centred on the page and in bold capitals before each summary.
5. **The abstract** should be written in **9 point** type size, between **100** and **150** words. The abstract should be written in the language of the text and in two more languages given above. The abstracts of the article written in each of the three languages should correspond to one another. The keywords should be written in two more languages besides the language of the article and should be at least three words.
6. **UDC** and **PACS** index should be used in the article.
7. The article must consist of the followings:

- Introduction
- Research method and research
- Discussion of research method and its results
- In case the reference is in Russian it must be given in the Latin alphabet with the original language shown in brackets.

8. **Figures, pictures, graphics and tables** must be of publishing quality and inside the text. Figures, pictures and graphics should be captioned underneath, tables should be captioned above.
9. **References** should be given in square brackets in the text and listed according to the order inside the text at the end of the article. In order to cite the same reference twice or more, the appropriate pages should be given while keeping the numerical order. For example: [7, p.15].

Information about each of the given references should be full, clear and accurate. The bibliographic description of the reference should be cited according to its type (monograph, textbook, scientific research paper and etc.) While citing to scientific research articles, materials of symposiums, conferences and other popular scientific events, the name of the article, lecture or paper should be given.

**Samples:**

a) ***Article:*** Demukhamedova S.D., Aliyeva İ.N., Godjayev N.M.. *Spatial and electronic structure af monomerrik and dimeric conapeetes of carnosine üith zinc,* Journal of structural Chemistry, Vol.51, No.5, p.824-832, 2010

b) ***Book:*** Christie ohn Geankoplis. *Transport Processes and Separation Process Principles*. Fourth Edition, Prentice Hall, p.386-398, 2002

c) ***Conference paper:*** Sadychov F.S., Aydın C., Ahmedov A.İ.. Appligation of Information – Commu-nication Technologies in Science and education. II International Conference."*Higher Twist Effects In Photon- Proton Collisions", Bakı, 01-03 Noyabr, 2007, ss 384-391*
References should be in 9-point type size.

10. The margins sizes of the page: - Top 2.8 cm. bottom 2.8 cm. left 2.5 cm, right 2.5 cm. The article main text should be written in Palatino Linotype 11 point type size single-spaced. Paragraph spacing should be 6 point.
11. The maximum number of pages for an article should not exceed 15 pages
12. The decision to publish a given article is made through the following procedures:

- The article is sent to at least to experts.
- The article is sent back to the author to make amendments upon the recommendations of referees.
- After author makes amendments upon the recommendations of referees the article can be sent for the publication by the Editorial Board of the journal.